Mechanical and Tribological Aspects of Microelectronic Wire Bonding

by

Aashish Satish Shah

A thesis

presented to the University of Waterloo

in fulfilment of the

thesis requirement for the degree of

Doctor of Philosophy

in

Mechanical Engineering

Waterloo, Ontario, Canada, 2010

I hereby declare that I am the sole author of this thesis. This is a true copy of the thesis, including any required final revisions, as accepted by my examiners. I understand that my thesis may be made electronically available to the public.

Abstract

The goal of this thesis is on improving the understanding of mechanical and tribological mechanisms in microelectronic wire bonding. In particular, it focusses on the development and application of quantitative models of ultrasonic (US) friction and interfacial wear in wire bonding. Another objective of the thesis is to develop a low-stress Cu ball bonding process that minimizes damage to the microchip. These are accomplished through experimental measurements of *in situ* US tangential force by piezoresistive microsensors integrated next to the bonding zone using standard complementary metal oxide semiconductor (CMOS) technology. The processes investigated are thermosonic (TS) Au ball bonding on Al pads (Au-Al process), TS Cu ball bonding on Al pads (Cu-Al process), and US Al wedge-wedge bonding on Al pads (Al-Al process).

TS ball bonding processes are optimized with one Au and two Cu wire types, obtaining average shear strength (SS) of more than 120 MPa. Ball bonds made with Cu wire show at least 15% higher SS than those made with Au wire. However, 30% higher US force induced to the bonding pad is measured for the Cu process using the microsensor, which increases the risk of underpad damage. The US force can be reduced by: (i) using a Cu wire type that produces softer deformed ball results in a measured US force reduction of 5%; and (ii) reducing the US level to 0.9 times the conventionally optimized level, the US force can be reduced by 9%. It is shown that using a softer Cu deformed ball and a reduced US level reduces the extra stress observed with Cu wire compared to Au wire by 42%.

To study the combined effect of bond force (BF) and US in Cu ball bonding, the US parameter is optimized for eight levels of BF. For ball bonds made with conventionally optimized BF and US settings, the SS is ≈ 140 MPa. The amount of Al pad splash extruding out of bonded ball interface (for conventionally optimized BF and US settings) is between 10–12 μm. It can be reduced to 3–7 μm if accepting a SS reduction to 50–70 MPa. For excessive US settings, elliptical shaped Cu bonded balls are observed, with the major axis perpendicular to the US direction. By using a lower value of BF combined with a reduced US level, the US force can be reduced by 30% while achieving an average SS of at least 120 MPa. These process settings also aid in reducing the amount of splash by 4.3 μm.

The US force measurement is like a signature of the bond as it allows for detailed insight into the tribological mechanisms during the bonding process. The relative amount of the third harmonic of US force in the Cu-Al process is found to be five times smaller than in

the Au-Al process. In contrast, in the Al-Al process, a large second harmonic content is observed, describing a non-symmetric deviation of the force signal waveform from the sinusoidal shape. This deviation might be due to the reduced geometrical symmetry of the wedge tool. The analysis of harmonics of the US force indicates that although slightly different from each other, stick-slip friction is an important mechanism in all these wire bonding variants.

A friction power theory is used to derive the US friction power during Au-Al, Cu-Al, and Al-Al processes. Auxiliary measurements include the current delivered to the US transducer, the vibration amplitude of the bonding tool tip in free-air, and the US tangential force acting on the bonding pad. For bonds made with typical process parameters, several characteristic values used in the friction power model such as the ultrasonic compliance of the bonding system and the profile of the relative interfacial sliding amplitude are determined. The maximum interfacial friction power during Al-Al process is at least 11.5 mW (3.9 W/mm^2), which is only about 4.8% of the total electrical power delivered to the US transducer. The total sliding friction energy delivered to the Al-Al wedge bond is 60.4 mJ (20.4 J/mm^2).

For the Au-Al and Cu-Al processes, the US friction power is derived with an improved, more accurate method to derive the US compliance. The method uses a multi-step bonding process. In the first two steps, the US current is set to levels that are low enough to prevent sliding. Sliding and bonding take place during the third step, when the current is ramped up to the optimum value. The US compliance values are derived from the first two steps. The average maximum interfacial friction power is 10.3 mW (10.8 W/mm^2) and 16.9 mW (18.7 W/mm^2) for the Au-Al and Cu-Al processes, respectively. The total sliding friction energy delivered to the bond is 48.5 mJ (50.3 J/mm^2) and 49.4 mJ (54.8 J/mm^2) for the Au-Al and Cu-Al processes, respectively.

Finally, the sliding wear theory is used to derive the amount of interfacial wear during Au-Al and Cu-Al processes. The method uses the US force and the derived interfacial sliding amplitude as the main inputs. The estimated total average depth of interfacial wear in Au-Al and Cu-Al processes is 416 nm and 895 nm, respectively. However, the error of estimation of wear in both the Au-Al and the Cu-Al processes is ≈ 50%, making this method less accurate than the friction power and energy results. Given the error in the determination of compliance in the Al-Al process, the error in the estimation of wear in the Al-Al process might have been even larger; hence the wear results pertaining to the Al-Al process are not discussed in this study.

Acknowledgements

I would like to express my sincere appreciation to my advisors Prof. Michael Mayer and Prof. Norman Y. Zhou for their invaluable guidance, constructive discussion, and encouragement, without which this work would not have been possible. My appreciation is extended to the members of the Examination Committee: Prof. Kaan Erkorkmaz, Prof. Mustafa Yavuz, Prof. Ting Tsui, and Prof. Andrei Sazanov for their scholarly suggestions, advices and examination in the whole process. I am honored to have George G. Harman, who is considered as the world's foremost authority on wire bonding, as the external examiner of this thesis.

I am indebted to Dr. I. Lum, Dr. J. Lee, Dr. C. Hang, Dr. H. Gaul, Dr. I. Qin, and Mr. C. Huynh for their support and useful feedback at different times during my PhD work. I thank all my labmates and friends in Waterloo for their useful advice and support throughout this research.

Last but not the least, I am greatly indebted to my parents Mr. Satish Shah and Mrs. Neena Shah, my wife Nikita, and my siblings Akshita and Abhinav for their continued moral support and love. Their sacrifices in making this work a reality is gratefully acknowledged.

To my loving family

Table of Contents

List of Figures

List of Tables

List of Acronyms

B

BB   Bonded ball

BDC BB diameter at capillary imprint

BDI   BB diameter at interface

BF   Bond force

BH   BB height

BPC   Bond process case

C

C. I.   Confidence Interval

CMOS Complementary metal oxide semiconductor

E

EDS   Energy dispersive x-ray spectroscopy

EFO   Electronic flame-off

F

FAB   Free-air ball

FE(M) Finite element (method)

FVC   Free vibration case

H

HTS   High temperature storage

I

IC   Integrated circuit

ID   Impact deformation

IF   Impact force

IMC   Intermetallic compound

N

NSOP   Non-stick on pad

P

PCB   Printed circuit board

S

SDI   Splash diameter at interface

SEM   Scanning electron microscope

SF   Shear force

SOIC   Small outline integrated circuit

SS   Shear strength

T

TEM   Transmission electron microscope

U

UED   Ultrasonic enhanced deformation

US   Ultrasound

W

WDS   Wavelength dispersive x-ray spectroscopy

List of Symbols

A_o — Free-air vibration of the capillary/wedge tool tip (in µm)

A_o^{max} — Maximum value of A_o (in µm)

A_B — Equivalent free-air vibration of the capillary/wedge tool tip during BPC (in µm)

A_B^{max} — Maximum value of A_B (in µm)

A_{rel} — Relative interfacial sliding amplitude (in µm)

A_{rel}^{max} — Maximum value of A_{rel} (in µm)

A_o^{nf} — Free-air equivalent vibration amplitude for no sliding at the interface in ball bonding (in µm)

A_T — Total sliding distance (in µm)

a_w — Vibration amplitude of the wire (or ball) bottom at the bonding interface (in µm)

a_w — Vibration amplitude of the pad top at the bonding interface (in µm)

a_b — Estimated maximum free-air equivalent vibration amplitude when there is no sliding at the interface in wedge-wedge bonding (in µm)

c_w — Ultrasonic compliance of the wire (or ball), tool, horn and transducer (in µm/N)

c_p — Ultrasonic compliance of the pad (in µm/N)

c — Total compliance of the ultrasonic system (in µm/N)

c_{pk} — Process capability index (dimensionless)

δ — Total average depth of material wear (in nm)

Δk — Error in δ due to the estimated variation in k (in nm)

ΔH — Error in δ due to the estimated variation in H (in nm)

$\Delta\delta_M$ — Error in δ due to measurement variability (in nm)

$\Delta\delta_T$ — Combined error of δ (in nm)

E	Total sliding friction energy delivered to the bond (in mJ)
f	Nominal ultrasonic frequency
f_{calib}	Calibration factor of the microsensor (in mV/V/N)
f_d	Calibration constant of A_o depending on transducer current I in K&S IConn ball bonder (in nm/mA)
F_N	Normal bond force (in mN)
F_T	Ultrasonic tangential force acting at the bond interface (in mN)
F_T^{nf}	Ultrasonic tangential force when there is no sliding at the interface in ball bonding (in mN)
F_b	Static friction force (in mN)
F_{max}	Maximum value of F_T (in mN)
H	Indentation hardness (in MPa)
I	Current delivered to the ultrasonic transducer during FVC (in mA)
I_B	Current delivered to the ultrasonic transducer during BPC (in mA)
I_B^{max}	Maximum current supplied to the ultrasonic transducer during BPC on Delvotec 6319 wedge-wedge bonder (in A)
k	Wear coefficient (dimensionless)
k_1	Constant of proportionality between I and A_o during FVC in Delvotec 6319 wedge-wedge bonder (in mA/μm)
M	Force signal response of the microsensor (dimensionless; in mV/V)
M_{max}	Maximum value of M (dimensionless; in mV/V)
N	Total number of ultrasonic cycles (dimensionless)
n	Sample size (dimensionless)
μ_m	Coefficient of friction between clean metal layers (dimensionless)
μ_s	Coefficient of static friction (dimensionless)
μ_{OA}	Overall coefficient of friction (dimensionless)

P	Ultrasonic friction power acting at the bond inteface (in mW)
P_{max}	Maximum value of P (in mW)
P_T	Total power delivered to the US transducer (in mW)
R_i	Nominal electrical resistance of the microsensor elements (in Ω)
S	Interfacial area (in μm^2)
s	Sample standard deviation (units)
σ_{US}^{sen}	Ultrasonic shear stress acting at the microsensor element (in MPa)
σ_{sen}^{max}	Maximum value of σ_{US}^{sen} (in MPa)
σ_{US}^{bond}	Ultrasonic shear stress acting over the bond interface (in MPa)
σ_{bond}^{max}	Maximum value of σ_{US}^{bond} (in MPa)
σ_{yy}	Normal stress acting at the microsensor element (in MPa)
σ_{yz}	Shear (tangential) stress acting at the bond pad (in MPa)
t	Time (ms)
t_b	Time stamp of F_b (ms)
U_{rel}	Relative sliding velocity (in $\mu m/s$)
USP	Ultrasonic parameter on Delvotec 6319 wedge-wedge bonder (dimensionless)
V_H, V_L	Differential voltage output of the microsensor Wheatstone bridge circuit (in mV)
V_S	DC supply voltage to the microsensor Wheatstone bridge circuit (in V)
V_B^{max}	Maximum voltage supplied to the ultrasonic transducer during BPC on Delvotec 6319 wedge-wedge bonder (in V)
W	Volume of material wear (in μm^3)
$W(t)$	Time evolution of W (in μm^3)
W_{cycle}	Volume of material wear per cycle of ultrasound (in μm^3)

1 Introduction

Microelectronic wire bonding is a critical process step in microelectronics packaging that provides for electrical interconnections between an integrated circuit (IC) and the larger scale substrate. It is estimated that more than 90% of semiconductor chips used wire bonding for interconnections in 2006 [1]. The market share of wire bonding in 2010 is expected to be more than 85%, resulting in $\approx$ 192.2 billion wire bonded devices [1]. The main reasons for the widespread use of wire bonding can be attributed to the nature of the process: self cleaning, low temperature, high yield rate, low cost, and flexibility. Interest in this technology continues to grow because electrical interconnect as provided by wires is one of the basic requirements for almost all microelectronic and micro-system devices.

In this introductory chapter, Section 1.1 describes the basics of wire bonding process. Section 1.2 presents a detailed literature review in this area. The motivation, objectives, and contributions of this study are summarized in Section 1.3. Finally, organization of this thesis is outlined in Section 1.4.

1.1 Wire Bonding

In wire bonding, a thin metal wire is welded to a metallized surface on the IC and package by a solid-state welding process that can be classified as ultrasonic (US) welding. The welding of the wire is achieved by a combination of constant normal bond force (BF), F_N pressing the wire to the pad, and an ultrasonic (US) tangential force $F_T(t) = F_T \sin(2\pi f t)$, where f is the US frequency and t is the time. Among the mechanisms observed in this process are sliding friction at the contact zone between the wire and pad (interface), wear (cleaning), and the establishment of metallurgical bonds.

1.1.1 Methods and Technologies

Based upon the type of energy and force used, there are three types of wire bonding processes: US, thermosonic, and thermo-compression. US bonding is performed at room temperature by applying normal force and US power. In contrast, thermosonic bonding uses

heat (usually less than 240 °C) in addition to the normal force and US power. Thermo-compression bonding is done by applying normal compressive force, at a very high temperature (usually greater than 300 °C) and normal force. It differs from the other two types in that no US is used in the bonding process, the lack of which is compensated by longer process times and higher process temperatures.

Based upon the type of bonds made, wire bonding can be classified into two types: ball-wedge bonding and wedge-wedge bonding. In ball-wedge bonding, shown in Fig. 1-1 (a), the first bond (known as the ball bond) is performed on the semiconductor chip and the second bond (known as the crescent or wedge or stitch bond) is performed on the lead frame of the substrate. In wedge-wedge bonding, shown in Fig. 1-1 (b), both bonds are almost identical, obtained by deforming the wire on the chip and the substrate. The major difference between these two types of processes is that wedge-wedge bonding uses an additional bondhead axes to rotate the US horn towards the wire loop direction. The wedge tool has an optimized shape for delivering the US always in the same direction. In contrast, the ball-wedge bonding process is performed using a ceramic capillary tool, which is rotational symmetric, allowing for bond loops to be formed in any direction. Only three bond head axes are required for ball-wedge bonding. A comparison of ball-wedge and wedge-wedge bonding is summarized in Table 1-1.
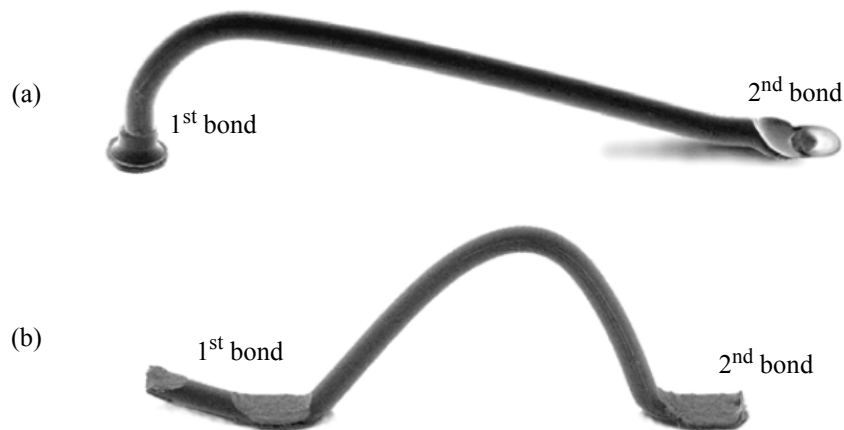
Fig. 1-1. Side view of (a) ball-wedge bond and (b) wedge-wedge bond. The wire material of the wedge-wedge and ball-wedge bond is AlSi (1%), and Au (99.99%), respectively. Reproduced from [5].

2

Among all the variants of the wire bonding technologies, thermosonic Au ball-wedge bonding is the most widely used process in the industry [2–4].

1.1.2 Thermosonic Ball-wedge Bonding

The schematic of the setup used for thermosonic ball bonding is shown in Fig. 1-2. A ceramic capillary tool, which is clamped to the horn, is used to provide the normal bonding load and US energy for bonding. The thermal energy is provided by a heated clamping stage, which holds the material to be bonded. The US transducer, made from polycrystalline piezoelectric ceramics, is attached to the base of the horn. The US energy propagates as a longitudinal wave along the length of the horn, which is then propagated as a transverse

Table 1-1. Comparison of ball and wedge bonding technologies

	Ball Bonding	**Wedge Bonding**
Technique (most common)	Thermosonic	Ultrasonic
Tool	Capillary tool (Al_2O_3)	Wedge tool (W, Ti)
Bonding wire (most common)	Au, Cu	Al, Au
Speed	up to 22 wires/second	up to 5 wires/second
Main applications	Microelectronics	Power devices, automotive electronics
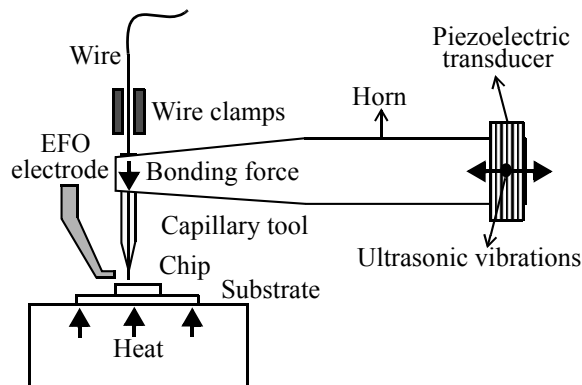
Fig. 1-2. Schematic setup of thermosonic wire bonding process.

3

wave in the capillary as shown in Fig. 1-3. Vibration nodes appear in the tool with a resultant oscillating tangential displacement at the tip of the tool. The number and location of nodes depends on the US frequency and the tool geometry.

The basic cycle of thermosonic ball-wedge bonding process is shown in Fig. 1-4. The bonding cycle starts with the application of a high voltage DC current to the electronic flame-off (EFO) system. This produces an arc between the edge of the wire beneath the capillary and EFO electrode, and the wire tail melts. Due to surface tension, the molten wire metal takes shape of a spherical ball before it solidifies. This ball is known as free air ball (FAB) and is centered inside the capillary chamfer. The capillary then guides the wire ball system to the first bonding location. The next stage is the ball bond formation stage. The capillary holding the FAB touches down the pad with an impact force resulting in the initial deformation of the FAB. This is followed by a plastic deformation of the ball by the interaction of normal bonding force, heat, and US energy, until the ball is bonded on to the pad. After the formation of the ball bond, the capillary retreats and shapes the wire into a loop by following a well defined trajectory to the second bond location. The capillary then deforms the wire and bonds it to the substrate, again by the application of normal force, heat, and US. Finally, the capillary moves up with the wire clamps open until a controlled length of wire called tail is formed. The clamps are closed and the wire breaks at its weakest part which is close to the heavily deformed zone near the second bond. The rise to the controlled
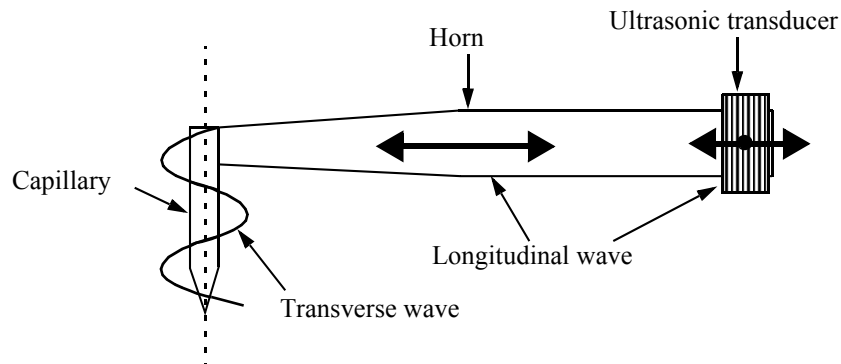
Fig. 1-3. Illustration of ultrasound propagation along horn and capillary.

4

tail length is important to generate the tails with constant lengths, which is crucial for an optimized FAB formation in the next cycle.

1.1.3 Ultrasonic Wedge-Wedge bonding

In US wedge-wedge bonding, there is no FAB formed at the end of the wire and the process is normally performed at ambient temperature. The wire, which is usually Al, is itself pressed on the bonding location using a wedge tool as shown in Fig. 1-5. The bonding procedure is similar to the thermosonic ball bonding process shown in Fig. 1-4, except for the absence of FAB and thermal energy.

1.2 Literature Review

In this section, a review of the wire bonding process is presented. It is classified into five broad categories: (i) process parameters; (ii) process types; (iii) process evaluation; (iv)
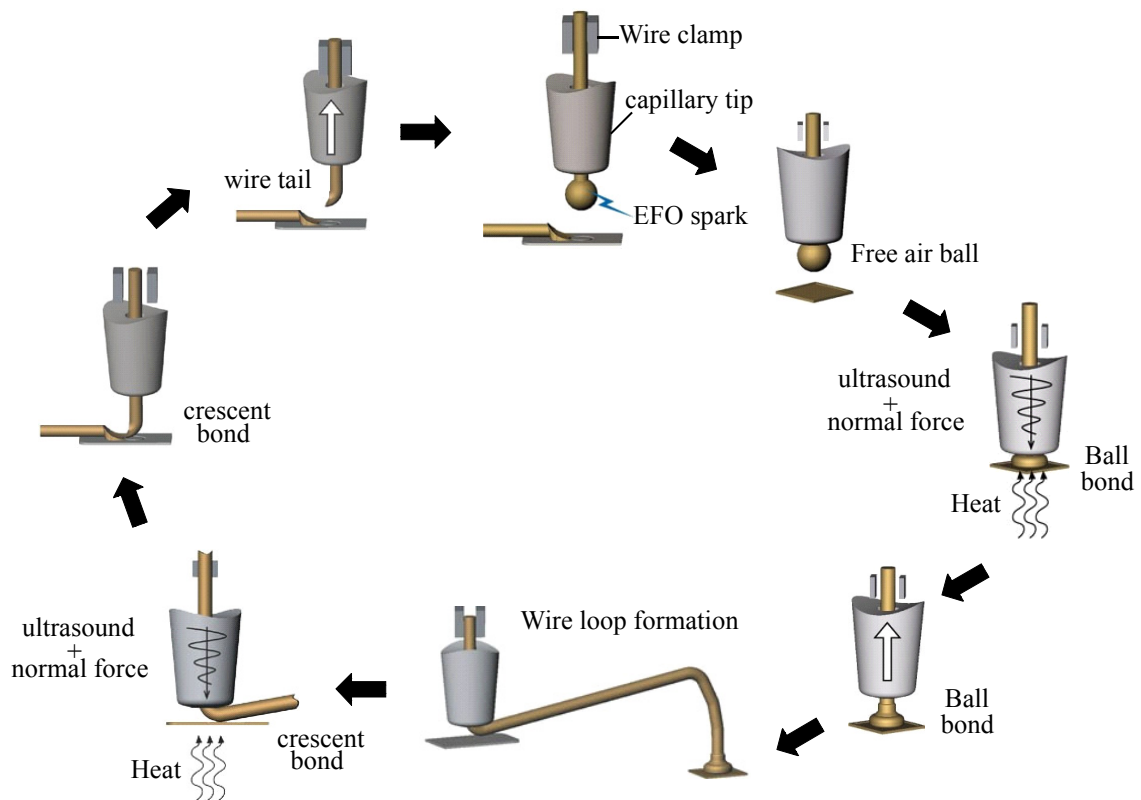
Fig. 1-4. Thermosonic ball bonding cycle. Adapted from [6].

5

aspects of chip damage during wire bonding; (v) theories of bonding mechanisms; (vi) finite element analysis of wire bonding process; and (vii) integrated microsensors for wire bonding process monitoring. Each of these categories are described in the subsections that follow.

1.2.1 Process Parameters

Wire bonding is affected by various process parameters. The most important parameters for successful and high quality wire bonding are initial FAB diameter, normal force, US energy, bonding time, and substrate temperature. It is very important to find an optimum combination of these parameters to achieve higher quality and robust bonds. These parameters interact with each other during the bonding process, which makes parameter optimization time consuming, tedious, and therefore inefficient.

1.2.1.1 Free Air Ball (FAB)

The FAB diameter is important as it is directly proportional to the final deformed bond size and strength. The size of the FAB depends on parameters such as wire tail length, time, current and electrode-wire distance. The tail bond is formed during the second bond formation of the previous cycle [7]. Weak tail bonds will lead to lifting off the wire from the substrate
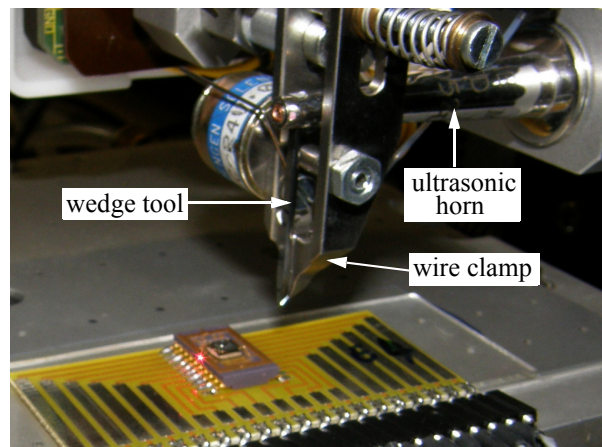
Fig. 1-5. Photograph of ultrasonic wedge-wedge bonding setup showing the wedge tool, ultrasonic horn and wire clamp.

before tail breaking stage and the tail will recede into the capillary resulting in stoppage of the process.

The studies of Chen et al. [8] reported that current and time are the most critical parameters affecting the FAB formation. The relation between FAB diameter $\varnothing$, current I, resistance R, and time t follows the parabolic law

$$\varnothing \propto Q = I^2 R t \tag{1-1}$$

where Q denotes the amount of heat generated during EFO spark [9].

During the formation of free air ball using Cu wire, the oxidation is prevented using a shielding gas such as a homogeneous mixture of 95% nitrogen and 5% hydrogen [9, 10].

1.2.1.2   Normal Force

Two types of normal forces are used during the thermosonic ball bonding process: impact force (IF) and bond force (BF). Typical industry practice is to use an IF value, which is 1.5 to 2 times higher than BF, but processes with IF lower than the BF are used, too. Extreme types of these two processes are described in Section 1.2.2.

The normal BF ensures that the ball is in intimate contact with the substrate. It has been suggested that high BF values decrease bonding action by limiting interfacial sliding of the ball [11]. The vibration amplitude at the tool tip decreases in an exponential manner as the BF increases under constant US setting [12]. With higher BF, the displacement of the bonding tool will be less and the US setting needs to be increased to have similar bonding.

1.2.1.3   Ultrasound

US vibrations dissipate the necessary friction energy at the interface. This has two benefits: ultrasonic cleaning of the native oxides from the bonding pad, and enhancing the intermetallic bond formation. The US vibrations are controlled by the amplitude of the piezoelectric transducer, which is proportional to the current delivered to it.

US has been shown to be the most important parameter in bond formation [13, 14]. Increasing US leads to increased displacement at the bond interface and subsequent increased

cleaning (due to wear) of the surfaces. With cleaner surfaces, more intimate contact between the two metal surfaces will occur, resulting in higher bonding (strength) [13].

There are two effects of US on metals: US softening and US hardening. In US softening, the static stress necessary for plastic deformation of metals is temporarily decreased during the application of US. On the other hand, US hardening as the name suggests leads to hardening, which is observed as a residual effect after the US irradiation is stopped.

In 1966, Langenecker [15] studied the effects of US on the deformation characteristics of materials. It was shown that intense US and applied thermal energy have similar effect on the reduction of the stress required for deformation. However, much less energy is required for US softening than the equivalent thermal softening.

Geisler et al. [17] used microhardness testing to point out that US has a residual softening effect on AlSi1 wire in wedge/wedge bonding. The softening was due to dynamic recrystallization of the wire that has high stacking fault energy prior to bonding. Recently, the investigation on the effect of US superimposed with normal force on the plastic deformation of Au [18,19] and Cu [20] during thermosonic ball bonding was reported. It was shown that when US irradiation is applied with normal force, the metal is softer than when deformed without US. After US is turned off, the deformed metal remains softer (if previously deformed with US) [18–20].

1.2.1.4 Bond Time

The bonding time parameter describes the duration of ultrasound during the bonding process. Mayer [11, 21] showed that most of the bonding takes place in approximately first 12 ms of the bonding time. Shorter bond times are preferred for increased productivity in the industry. The bonding time depends on the frequency of the US parameter.

1.2.1.5 Bond Temperature

Elevated temperature during bonding enhances the interdiffusion between the ball and the substrate, necessary for the formation of a strong metallurgical bond [11]. Due to high temperature, the bond surface gets dehydrated resulting in a uniform surface quality and increased process stability [11]. A high bonding temperature assists in the bonding as it

allows increased deformation by reducing the yield strength of the bond material. However, excessive bonding temperatures may result in too much wire deformation and higher fluctuations in bond placement accuracy.

1.2.2 Process Types

The major process factors in ball bonding are normal force and US and the way these factors are controlled over time. These factors determine the two major mechanisms observed in the thermosonic ball bonding process, which are the plastic deformation of the free-air ball (FAB) and the bond formation at the interface. With respect to the normal force and US profiles, two major process types can be distinguished, characterized by the way the ball is deformed: (i) the US-enhanced deformation (UED) process for which a single load bond force profile is sufficient [22]; and (ii) the impact deformation (ID) process for which a double load bond force profile is required [23–25]. For commercial applications, wire bonds are often made with a mixture of these two process types, e.g. a double load process that includes UED. Extreme cases of UED and ID process types are illustrated in Figs. 1-6 (a) and (b), respectively.

The UED process is characterized by a relatively small impact force during touchdown of the ball on the pad, resulting in little deformation and a small initial interface area. The major part of the overall deformation happens during the subsequent dissipation of US. Underpad stresses are high during the first moments of US dissipation as this is when normal force and US forces are concentrated on the relative small initial interface area.

The ID process is characterized by a relatively high IF to BF ratio causing most or all of the ball deformation already before US starts. During the subsequent US period, the bond forms uniformly over the interface. Compared to an UED process, an ID process can allow for more uniform bonded ball geometries, faster throughput due to faster search/approach times (i.e. higher contact velocities), and potentially more reliable bonds because of more uniform intermetallic coverage formed at the interface. Weaker bond at the interface periphery (peripheral effect) can be avoided with an ID process. Previous studies using Au [23] and Cu [24, 25] wires reported that ID process aids in reducing defects related to bonding stress (e.g. cratering).

9

1.2.3 Process Evaluation

The common techniques used evaluate the wire bond quality are visual inspection (optical or electron microscopy), pull testing, shear testing, and reliability testing. The pull test, shear test, and bond reliability assessment methods are described below.

1.2.3.1 Pull Test

Typically, in industry the quality of a wire bond is tested by performing a wire pull test. In this test, illustrated in Fig. 1-7, a hook is used to pull on the wire at midspan in order to determine the mode of failure as well as the breaking load. On good bonds, typically the wire bond will break in the wire. According to Harman [1], this method of bond quality evaluation is suitable for US wedge bonds, but it is not the best method to test the thermo-sonic ball bonds. This is because the interfacial bonded area in ball bonds is approximately 6 to 7 times larger than the cross-section area of the wire, thus the wire may break in pull testing even before a poorly bonded ball lifts. In addition, the region of the wire just above
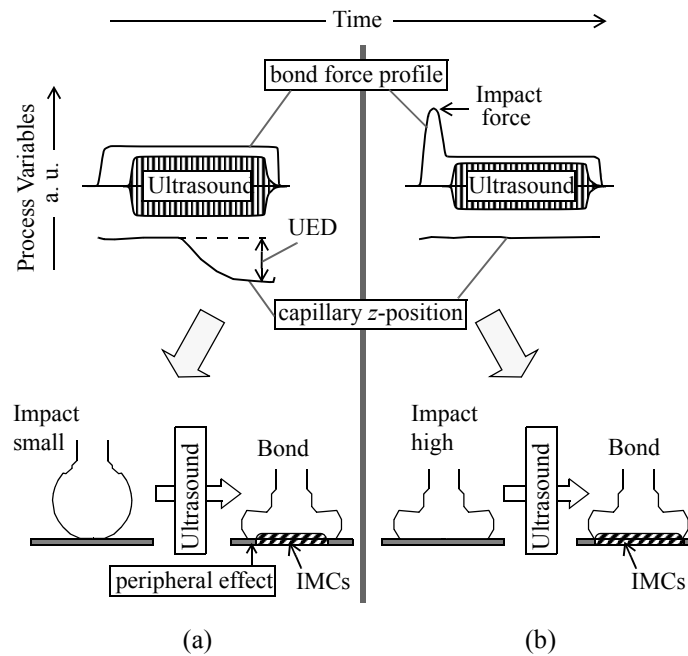
Fig. 1-6. Illustrations of two ball bond process types: (a) Ultrasound enhanced deformation (UED). (b) Impact deformation (ID). IMC = intermetallic compound. Illustrations by M. Mayer.

10

the ball, called heat affected zone is the weakest part of the wire. Pull test failure often occurs in this area, again not providing complete information about the quality of the bond between the ball and the substrate. However, quality assurance with the pull test remains widely used in industry.

1.2.3.2 Shear Test

The shear test is used to measure the force required to shear off a ball bond. In this test, a shear tool is used to shear the ball bond at a fixed height (typically about 5 µm) above the bond pad, as shown by the illustration in Fig. 1-8. The shear force (SF) of the ball is related to bond quality based on the calculation of its nominal shear strength (SS). The value of SS
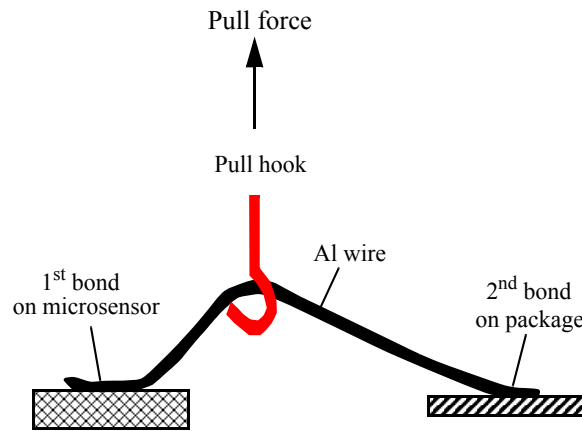
Fig. 1-7. Illustration of the pull test of an Al wedge-wedge bond.
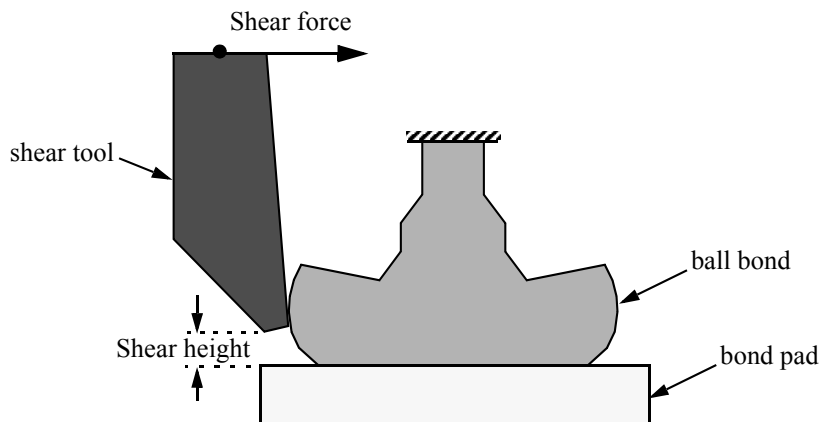
Fig. 1-8. Illustration of a ball bond shear test.

is calculated as the SF divided by the nominal bond area. The shear test is standardized in [26].

1.2.3.3 Reliability

Reliability testing is often used for long-term quality assessment of the wire bonds. The wire bonds are subjected to temperature cycling, high temperature storage (HTS) or exposed to hot and humid atmospheres. Subsequently, the samples undergo metallurgical procedures for analyses using an optical microscope or a scanning electron microscope (SEM) for intermetallic compound (IMC) coverage. Pull and shear tests are also carried out after these aging procedures to test the long-term reliability of the bond connections. Such reliability tests are required before mass production can start.

In contrast to destructive testing like shear testing or IMC coverage measurements, non-destructive monitoring of ball bond reliability can reduce the effort and amount of samples required while allowing for a higher time-resolution measurements. Non-destructive monitoring was used based on measuring the electrical contact resistance R_c of the bonds [27–33]. The electrical parameter R_c is important for describing the quality of bonds, considering that ball bonds can be mechanically strong after HTS while being electrically degraded [34]. Recently, a new application of stress sensors for online reliability monitoring of Au wire bonds was reported [35,36]. Localized stress measurements close to the bond zone are used in combination with R_c measurements to evaluate the reliability performance of Au ball bonds during HTS [35,36]. The stress sensor approach is a promising tool since detailed insights into physical mechanisms related to bond reliability can be gained using this method.

1.2.4 Chip Damage

Chip damage can occur as delamination of layers, bond pad peel-off or delamination [37–40], fracture of dielectrics or underpad interfaces [39, 40], or Si cratering [41–48] as illustrated in Fig. 1-9 (a)–(c), respectively. In pad de-lamination, the bonded ball lifts-off together with the bonding pad. On the other hand, cratering appears as damage to the semiconductor, silicon dioxide, or other dielectric layers under the bonding pad. It is termed cra-

tering when a hole is left in the substrate with its remains attached to the wire. However, most of the time, no visible damage is seen immediately after bonding [46–48], but can degrade the device characteristics by creating micro-cracks internally as illustrated in Fig. 1-9 (b). These cracks result in cratering failures during thermal aging and accelerated reliability tests [43]. Cratering usually occurs in only a small percentage of the bonds, even though the bonds are created at the same time with the same bonding parameters. It can occur in various forms: metal extrusion, marginal cratering at center of bond, marginal cratering at bond periphery and bulk Si cratering [42].

Si cratering refers to complete fracture and removal of the bond pad underlayers during bonding. It is induced by overbonding or improper bonding parameters, in particular US and BF [1, 50–52]. In addition, there are many materials and equipment problems such as improper capillary profile [46], wire (or ball) hardness [43], and bond pad thickness [53] and hardness [51, 53–55].
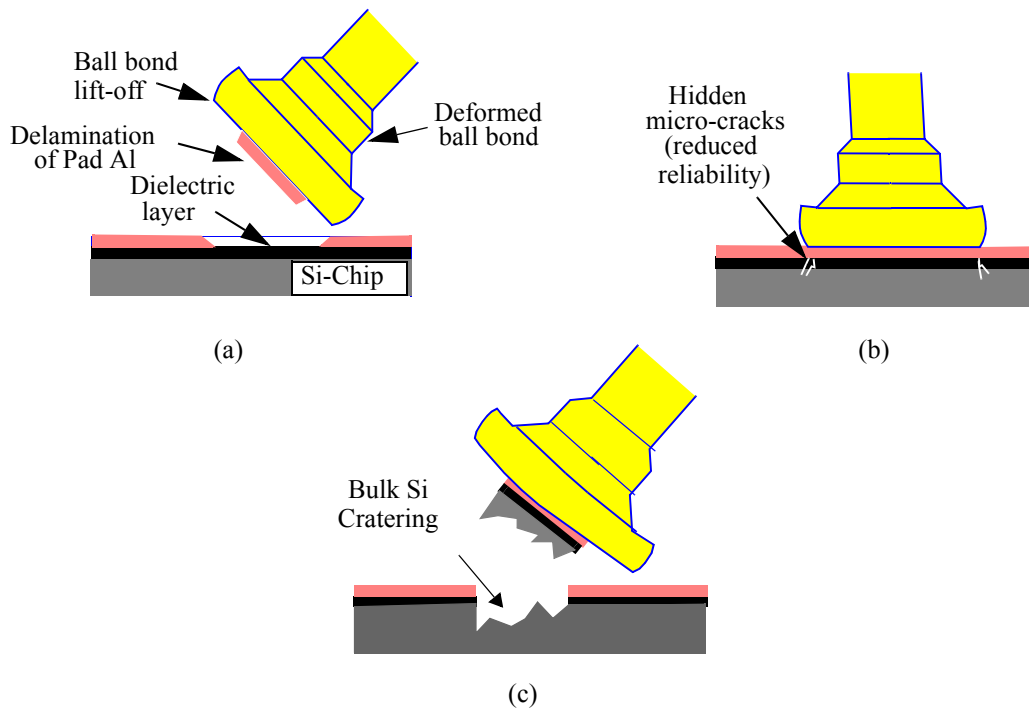
Fig. 1-9. Illustration of underpad damage types (a) bond pad peel-off, (b) hidden microcracks, and (c) bulk Si cratering. Reproduced from [49].

13

The bond pad serves as a cushion to protect the underlying material from damage due to the mechanical stresses during bonding. Winchell and Berg [53] found that craters were most prevalent for thin metallization. A softer bonding pad metal would inhibit cratering by absorbing US energy and deforming easily, while a hard pad should more readily transmit the ultrasonic energy to the substrate [2]. However, recent work has shown that using harder bond pads, such as Ni/Pd, Ni/Au, and Ni/Pd/Au are robust in minimizing chip damage [55].

Harder wires require higher force and US energy to bond, and this induces higher stresses to the pad, which increases the chances of cratering. However, the actual role of wire hardness in cratering is not understood completely because of the synergistic effect of other variables.

Currently, optimization of wire bonding processes to avoid chip damage is a major research area, which is attributed to two causes. The first is increased use of low-k dielectric layers in microchips. Low-k dielectrics have low mechanical strength and hence are more prone to chip damage [56–57]. The second cause are the trends towards replacing the industry standard Au wire bonding with Cu wire bonding [58]. Cu wire being harder than Au increases the likelihood of chip damage [42–45, 48–51].

1.2.4.1 Pad Splash

One mechanism specifically observed during ball bonding of Cu on Al bond pad is the squeezing of Al pad metal from the peripheries of the ball bond [59–62] as shown in Fig. 1-10 (a) and (b). The Al material squeezing out is termed as *splash*, and it occurs in the US direction. Splash is not desired as it results in localized pad thinning [61], which can reduce bond reliability [61]. Mechanisms to reduce the formation of Al splash are not fully understood yet. A possible reason for splash may be attributed to the hardness of Cu compared to Al, and the subsequent higher stresses observed during the Cu ball bonding process [62]. It has been reported that pad splash is not observed for Cu ball bonds made on harder bond pads, such as Ni/Pd, Ni/Au, and Ni/Pd/Au in Cu ball bonding [55]. Recently, it was shown that using US during the impact portion of bonding aids in minimizing Al splash [63].

1.2.5 Theories on Bonding Mechanisms

There have been many theories on mechanisms underlying the wire bonding process proposed in the literature. The most important of these are: (i) melting; (ii) inter-diffusion; (iii) wear/micro-deformation; and (iv) micro-slip. Each of these theories are described in the following sections.

1.2.5.1 Melting

Among the earlier theories was the wire bonding mechanism proposed by Kreye [64] in 1977. The US spot welds were observed using transmission electron microscopy. After analyzing the interfacial microstructure, it was concluded that melting of a thin interfacial layer had occurred during the bonding. In another study published in 1978, Winchell and Berg [53] proposed that US friction energy caused by scrubbing and heating of the wire and the bonding pad. This caused localized melting of the interfaces involved in the bonding process and subsequent welding between them due to fusion. However, since then there have been several instances wherein it has been confirmed by experiments that wire bonding is a solid state welding process and no melting of the bonding materials occurs during the welding process. Notable among them is the work of Harman and Leedy [54], in which they performed wire bonding by immersing the tool, wire and substrate in liquid nitrogen. They obtained strong bonds with no air bubbles and little temperature rise. Furthermore,
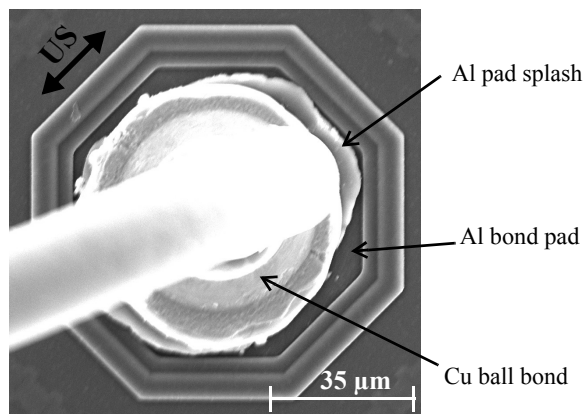
Fig. 1-10. SEM micrograph of a Cu ball bond on Al pad depicting the Al pad metal splash.

15

examination of the bonded surface by TEM [65] confirmed that no melting is required for bond formation. Experimental studies [13] involving measuring the interfacial temperature of the bond area using thermocouple showed that the temperature rise during ultrasonic wire bonding reached between 70-80 $^{\circ}$C. This suggested that US wire bonding cannot be considered a thermally activated diffusion process. Recent results [66] show that melting can occur using process parameter levels twice as large as optimum levels with a low melting point metallization (Sn). In conclusion, melting can be observed but is not desired to achieve sufficient weld quality. Therefore, melting is irrelevant in this context and no further studies were conducted trying to support it.

1.2.5.2 Inter-diffusion

Inter-diffusion is a common phenomenon observed during the US wire bonding process, particularly in Au-Al system. Applied mechanical and thermal energies directly affect the diffusion coefficients of the two materials, thereby promoting inter-diffusion between them. There have been many research papers on inter-diffusion in US wire bonding. Almost all of them sought to explain that inter-diffusion was either due to the normal forces or due to temperature rise during bonding [1]. However, there was no evidence of the direct role of US on diffusion coefficients. In 1966, Hochman and Gray [67] published a note on the effect of US energy on diffusion and sintering of tin into lead. It is found that there was an increased concentration of tin in lead after US activation, which is attributed to increased volume diffusion. As the temperature was carefully controlled, it resulted in negligible heat effect. However, there were no further evidences to support this theory.

1.2.5.3 Wear/Micro-deformation

It has been postulated that US frictional energy solely causes interfacial deformation and wear, which is necessary to displace surface contaminants and produce clean metal surfaces, which can readily bond due to adhesion, applied pressure and US energy. In 1973, Harthoorn [68] conducted an experiment in order to investigate the effect of US and fretting on Al wire/Al substrate joining surfaces. The fretting experiment was conducted in a custom made apparatus at 30 Hz and 45 MPa. The results demonstrated that there is a pronounced increase in the micro-welds as the number of vibrations is increased independent

of frequency. It was proposed that due to US vibration, there is uniform scrubbing of the entire area, which resulted in micro-deformation of the surface asperities due to wear. Furthermore, upon examination of the joints by US welding and fretting revealed similar results and it was concluded that joining in both processes was due to plastic micro-deformation.

It was reported that interfacial deformation exists in thermo-compression bonding and thermosonic bonding where the only difference in the two processes was that the plastic deformation in the former was due to high pressure and thermal energy while in the latter it was due to US energy [54]. However, Zhou et al. [16] showed that bonds made with same deformation with and without US had different bond strengths and contact area. Therefore, US has effects other than merely helping in deformation.

1.2.5.4 Micro-slip

The micro-slip based theory of US wire bonding mechanism was proposed by Chen [69] in 1972. The wire bonding process was described by the classical elasticity model proposed by Mindlin et al. [70]. In his theory, Mindlin considered the contact between two spheres under the action of oscillating tangential load. The central region was referred to as the elastic or non-slip region while the peripheral area exhibited micro-slip when tangential force is sufficiently high. It was postulated that due to micro-slip, the surface contaminants are displaced and the bonding is due to the result of adhesion of two clean metal surfaces coming in intimate contact with each other. If the US energy is considered as the oscillating tangential force, then it implies that according to the micro-slip theory, bonding will dominate at the periphery of the interfacial contact rather than at the centre.

Recent publications tend to support this theory, e.g., the work of Zhou et al. [16] in which they showed that metallurgical bonding initiated at the lateral periphery at low US power and gradually moved towards the central regions as the US power was increased. In a numerical study of US wire bonding process, Ding et al. [71] observed that maximum frictional energy intensity occurred at the periphery of the contact area rather than at its centre.

In 2005, Lum et al. [72] investigated the effects of process parameters in thermosonic gold ball bonding on Cu substrate with scanning electron microscopy (SEM). A basic model

based on the micro-slip theory was developed to explain the phenomena of bond formation in wire bonding. They experimentally verified the result of Mayer [11] and Zhou et al. [16] that relative motion existed at the bonding interface and suggested that this relative motion at the bond interface exists as micro-slip at low US and transitions into gross sliding at higher powers. They postulated that an increase in US power results in micro-slip region growing towards the ball center and a corresponding increase in the contact area. In another paper [73], the same authors confirmed this result for US Al wire wedge bonding on Cu substrate. It was concluded that the bonding mechanisms in US ball-wedge and wedge-wedge bonding are very similar. Modern processes, however, do not show much difference between peripheral and central bonding areas. Microslip alone is mostly unfit for making high quality bonds.

1.2.6 Finite Element Analysis

Finite element (FE) analysis is an excellent way to obtain insight into physical quantities highly localized at the interface. The ball bonding process includes several physical mechanisms that have been partly described by FE models, for example, plastic wire deformation [5, 40, 71, 74–79], work hardening and/or rate-dependent properties of wire or pad [18, 40, 76–79], interfacial sliding friction [40, 71, 74, 76, 77, 80], US cycles [5, 40, 74, 76, 79, 80], cyclic plasticity [81], dynamic effects of the bonding tool [5, 82, 49], and thermal effects [40, 77]. Process factors studied are bond force and US-related parameters [40, 74, 77, 49], US frequency [77], friction coefficient [76, 77], mechanical properties [76], wire/pad dimensions [77, 78], and shape of the tool tip [78]. Responses investigated were under-pad stress [5, 40, 74, 76, 77, 49], interfacial friction [74], wire stress/shape [5, 40, 77, 78], plastic dissipation energy [76, 77], residual stress [40], and temperature [77].

1.2.7 Integrated Microsensors

In addition to the conventional offline process monitoring methods such as visual inspection, wire pull testing, and bond shear testing, novel real-time monitoring techniques such as the measurements of US amplitudes using laser interferometry [22, 83], piezoelectric sensor attached to the horn [84], piezoelectric sensor mounted to the heater block [85], and

integrated microsensors [5] have been applied to gain a better understanding of the process. The microsensor based approach is reviewed below.

Complimentary Metal Oxide Semiconductor (CMOS) microsensors have been used for wire bonding process monitoring and characterization by enabling real-time, *in situ* experimental measurements of temperature, normal force F_N, and US tangential (shear) force F_T [86]. Circular aluminum metal resistors integrated next to the bond pad were used for *in situ* temperature measurements, while silicon piezoresistors were used to sense F_N and F_T. The design details of these test chips and sensors is documented in detail in [5]. Detailed information on the physical principle and mathematical description of the piezo-resistance of silicon are discussed in [87-90].

An early publication about integrated microsensors for monitoring the wire bonding process appeared in 1998 when Mayer et al. [86] reported a direct measurement method for real time, *in situ* monitoring of the quantities related to temperature and mechanical stress during the thermosonic ball bonding process. The quantities measured were bonding force and temperature of the pad. These measurements identified three different physical effects: mechanical stress induced by the F_N applied on the capillary, cooling of the chip by the heat transfer between the test pad and gold ball, and heating of the chip by the US dissipation.

1.2.7.1   *In situ* Temperature

Mayer et al. [91] described the use of an integrated aluminum resistive microsensor for *in situ*, real time measurements of temperature close to the bond zone during ball bonding. The microsensor signal quantified cooling and heating of the pad during ultrasonic dissipation. Three distinct stages are identified based upon this signal. Stage one starts with capillary touch down which results in a steep drop in the temperature of the bond pad due to localized cooling of the ball by the capillary. After the steep drop, there is a partial recovery due to heat transfer from the heated chip. The second stage represents the application of US which is witnessed by a steep rise in temperature until it reaches a peak value. When the US excitation stops, the temperature falls down rapidly. The third stage is when the bond has been formed and the capillary is touching the bond pad without US. As such, the temperature remains more or less constant and reaches a level (which is still lower than the ini-

tial level, as the bonded wire acts as a heat sink) after the tool lifts off. Supported by experimental observations, it was concluded that sliding and scrubbing at the bond interface plays a crucial role in bond formation. In addition, it was confirmed that temperature rise due to US was not high enough to cause melting of the bonding surfaces.

The Al resistive microsensor used to measure temperature yields an average temperature close to the bonding interface. In [92], a FE model was developed to estimate the average temperature at the bond interface from the microsensor measured temperature.

Suman et al. [93, 94] confirmed this result using a test structure with embedded thermopile sensors that measured temperature at a radial distance under the bond pad. In [94], they presented an approach to separate the thermal response due to US excitation and ball deformation using thermopile sensor measurements and transient thermal FE modeling of the process. The results suggested that US energy and ball deformation independently cause rise in temperature under the bond foot print.

1.2.7.2 *In situ* Ultrasonic Force

A p^+ diffused piezoresistive microsensor [11, 21] integrated next to and under the bonding pad have been used for *in situ* measurements of F_T during ball bonding. The microsensor signal revealed significant process characteristics such as minimal US level needed for bonding and the minimal dwell time needed to start (i) scrubbing and intermetallic formation, and (ii) to attain maximum shear strength. Based upon the evaluation of the fundamental and harmonic components of the microsensor signals, the authors identified four distinct phases during bond formation: initial stiction, sliding, bond growth, and ultrasonic softening. Among these, the first three phases are required for successful bond growth.

In phase 1, the ball sticks to the substrate, due to static friction (stiction) between the two contact surfaces. In this phase, the US amplitude is not large enough to overcome stiction. The second phase is characterized by an increase in the third harmonic of the US signal. This indicates the presence of interfacial sliding (interfacial slip, dynamic friction) at the ball-substrate interface. The authors suggested that interfacial slip leads to oxide removal (US enhanced cleaning by fretting wear) and subsequent bonding of the clean surfaces. Furthermore, if the US power is set low, the third harmonic does not exist, which indicates

there is practically no sliding for bonding to take place. The phase 3 symbolizes the metallurgical bond formation phase. In phase 4, the harmonics undergo little change. During the sliding and bond growth phases, the pad complied with the ball like a harmonically driven friction oscillator. The analysis of the harmonics of the US frequency concluded that there exists a stick-slip motion at the bond interface. This stick-slip motion results in relative movement between the ball and pad, which is found to be a pre-requisite to high quality bonding. In summary, the work of Mayer [11, 21] tends to describe the wear/micro-deformation theory of US wire bonding.

The concept of stick-slip friction was further developed in [95–97]. An analytical model that describes the development of bonding in thermosonic ball bonding was reported based on the friction power [95]. The model incorporates material properties, coefficient of friction, and bonding parameters like bond force, time, and US power. In [96, 97], a bond quality factor is introduced based on friction power. This model was extended in [22] to include wire deformation during the process.

1.3 Motivation, Objectives and Contributions

In the microelectronics industry, there is a continuous push towards higher performance and lower costs [98]. In addition, trends towards miniaturization lead to reduced package sizes and form factors of the devices that are pad limited. This results in a need for finer pitch interconnection with longer wires. This has further led to an increased focus on the research and development of finer diameter wire and new materials for wire bonding process.

Cu wire is now being considered as possible material to substitute Au wire in thermosonic wire ball bonding [58, 99–101]. Cu wire to Al pads and Cu wire to Cu pads are currently evaluated as methods for reducing cost and pitch [51, 102, 103]. There are two major reasons for the interest in Cu wire: its superior electrical and thermal conductivity to Au [51, 102], and it is less expensive than Au [103]. For example, using Cu wire instead of Au wire can reduce production costs by up to 90% [58]. In addition, Cu boasts of reduced intermetallic growth [59, 60], higher reliability of the bonding connection at higher temperatures

and better mechanical stability [48, 104]. Thus, thinner Cu wires can be used and longer wire loops can be bonded without any wire sweep (also called wire sag) [48].

Among the current roadblocks that hinder the employment of Cu wire into IC interconnections are its tendency to oxidation, and high hardness of Cu. Oxidation of Cu reduces its bondability and its high hardness increases the risk of pad peeling, cracks and cratering in the underlying Si during bonding [37–45]. Moreover, Cu easily strain-hardens when deformed during bonding [105] and exhibits a larger strain-hardening effect especially at higher strain rates [106]. This strain-hardening effect can result in gross cratering i.e. when pieces of the silicon chip are visibly cracked and broken [43]. As the semiconductor industry moves towards higher signal speeds by employing multi-layered bond pads with low-k dielectric layers, which have low mechanical robustness, this additional hardness of Cu presents a major challenge for high yield wire bonding process development. Methods to evaluate the processes and optimization of parameters in the context of bonding stress and underpad damage are therefore essential.

To develop the best possible wire bonding processes with novel Cu wires, an improved understanding of the bonding mechanisms with such wires promises to be helpful. Despite being a widely used process, there is a general lack of fundamental understanding of the mechanics and tribology of the wire bonding process. In particular, studies on quantitative models are limited.

1.3.1 Objectives

This research intends to contribute novel and innovative solutions to overcome the current roadblocks in wire bonding. It is aimed at obtaining detailed insights into the process mechanisms in wire bonding. Three common wire bonding processes are investigated: ball bonding with Au and Cu wires, and wedge bonding with Al wire. The main objectives of this research are:

1. Develop low-stress Cu ball bonding processes. Formulate guidelines to optimize process parameters and settings to minimize damage to the semiconductor chip.

2. Improve the understanding of mechanical and tribological aspects of wire bonding, in particular the US friction at the bonding interface.

3. Develop, extend, and apply the quantitative models of US friction and interfacial wear in wire bonding.

1.3.2 Major Results and Contributions

Low-stress Copper Ball Bonding
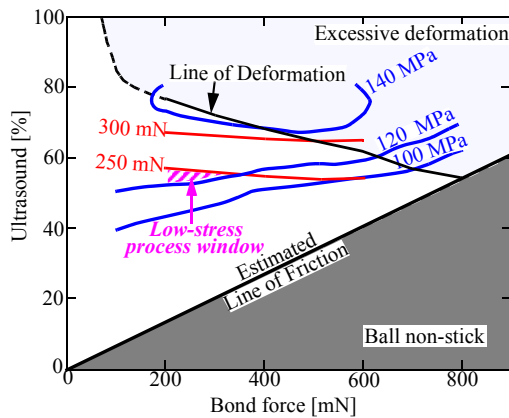
A novel low-stress process window for thermosonic copper ball bonding is determined. Instead of a conventional shear strength maximization, an adequate trade-off between shear strength and pad stress is recommended for copper ball bonding. The results demonstrate that the underpad defect risks typical to a copper ball bonding process can be reduced by a thorough optimization of the bonding process settings, in particular ultrasound and bond force.

Improved Understanding of Process Tribology
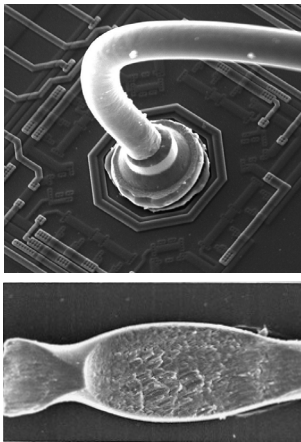
Improved understanding of ball-wedge and wedge-wedge bonding processes is obtained. For the first time, the *in situ* tangential force acting at the bond interface is measured and analyzed for the thermosonic Cu ball bonding and ultrasonic Al wedge bonding processes. The tangential force measurement is like a signature of the bond as it allows for detailed insights into the physical mechanisms during various phases of the bonding process, e.g., stiction phase, start of friction (cleaning) phase, and bond growth phase. The relative amount of third harmonic of tangential force in Cu ball bonding is found to be five times smaller than in Au ball bonding process. In contrast, in Al wedge bonding, a large second harmonic content is observed, describing a non-symmetric deviation of the force signal waveform from the sinusoidal shape. The analysis of harmonics of the tangential force leads to the conclusion that although slightly different from each other, stick-slip friction is an important mechanism in all these variants of wire bonding.

Ultrasonic Friction Power, Energy, and Total Sliding Distance
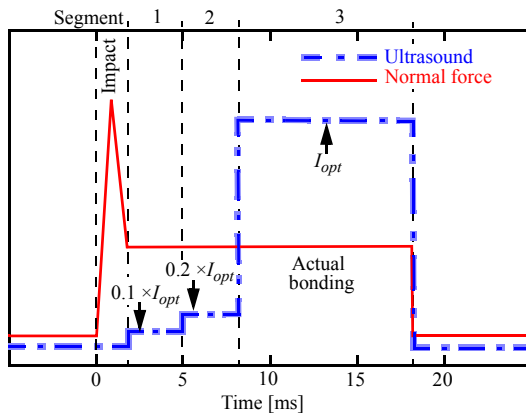
A friction power theory is used to derive the transient profiles of ultrasonic friction power during Au and Cu ball bonding, and Al wedge bonding processes. For bonds made with typical process parameters, several characteristic values used in the friction power model such as the ultrasonic compliance of the bonding system and the relative interfacial sliding amplitude are determined using a new method with improved precision. Detailed insights into the interfacial tribological mechanisms e.g. start and end of friction can be detected from the derived curves. It is found that the friction cleaning process in Cu ball bonding is faster than in Au, resulting in faster bond formation in Cu process compared to Au process. Typical values of total sliding distance and friction energy density are reported.

Interfacial Wear
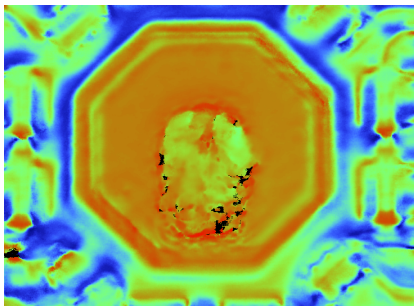
The sliding wear theory is used to estimate the amount of interfacial wear during wire bonding. The method uses the derived interfacial sliding amplitude and tangential force as the inputs. For the first time, a transient profile of interfacial wear during thermosonic Au and Cu ball bonding processes is reported. Values of wear coefficient, total wear volume and wear depth are estimated. The results show that only a few cycles of ultrasound are required to disperse the native oxides and precipitates away from the interface.

1.4   Organization of Thesis

This thesis is divided into six chapters. Chapter 2 presents and compares the US tangential force measured during thermosonic Au and Cu ball bonding process. It investigates the mechanisms of bond growth in Cu ball bonding. Ball bonding processes are optimized with one Au and two Cu wire types. It shows how a reduced US level and softer Cu wire type can be used to optimize a Cu ball bonding process with reduced ultrasonic pad stress. The

chapter contains the process optimization procedure and results, the description of the microsensor used, results and discussion.

Chapter 3 extends the study presented in Chapter 2 by looking at the synergistic effect of BF and US on the ultrasonic pad stress. It contains the process and pad splash optimization results, and the microsensor measurements. A low-stress process window for Cu ball bonding is determined and reported. Some guidelines to optimize a low-stress Cu ball bonding process are outlined.

Chapter 4 investigates the US tangential force measured during Al wedge bonding process. The analysis of the harmonics of the force signal is analyzed and compared with those obtained during Au and Cu ball bonding processes. A friction power model is used to derive the US friction power during Al wedge bonding process. The chapter contains the theory, experimental details, results, and discussions.

Chapter 5 applies the friction power model in thermosonic Au and Cu ball bonding processes. A method of bond process modification is reported, which enables an accurate derivation of the mechanical compliance of the US bonding system. The chapter describes the method of bond process modification and example results of transient interfacial sliding amplitude and friction power are presented. Finally, a method to estimate Al pad wear during Au and Cu ball bonding using the derived relative sliding amplitude and the measured US tangential force is reported.

Chapter 6 lists the conclusions and provides recommendations for future research.

2 In situ Ultrasonic Force during Thermosonic Au and Cu Ball Bonding

Given the cost and performance advantages associated with Cu wire, it is being increasingly seen as a candidate to replace Au wire for electrical interconnects in microelectronics packaging. However, Cu wire brings with it a set of challenges and problems, which need to be addressed before a robust Cu ball bonding process can be implemented in the industry. In particular, a better understanding of process mechanisms during Cu ball bonding promises to be helpful.

One of the most suitable methods to this end is to use microsensors to measure the in situ forces caused by US induced to the pad during bonding. In situ US tangential force measured using integrated piezoresistive microsensors were used previously to describe the interfacial stick-slip motion [11] as the most important mechanism in thermosonic Au wire ball bonding to Al pads (Au-Al process). In this chapter, the same experimental method is applied with a hard and a soft Cu wire type (Cu-Al process). The signals are compared with those obtained from ball bonds with standard Au wire. Prior to carrying out the microsensor measurements, the bonding processes are optimized to obtain consistent bonded ball diameters of ≈ 60 μm, yielding average shear strengths of at least 120 MPa at a process temperature of $\approx 110°C$.

The ball bond process optimization is described in Section 2.1. The analysis of the measured ultrasonic tangential force signals, including the microsensor design and calibration is reported in Section 2.2. Section 2.3 reports on a new method to reduce ultrasonic pad stress during thermosonic Cu ball bonding. Finally, Section 2.4 summarizes the results.

The research reported in this Chapter has been published in parts in *Microelectronics Engineering* [62], *Proceedings of 58th IEEE Electronics Components and Technology Conference* [107], and *IEEE Transactions on Electronics Packaging Manufacturing* [108].

2.1 Ball Bond Process Optimization

The automatic ESEC 3100 wire bonder (Besi Esec, Cham, Switzerland) is used to perform thermosonic ball bonding with a standard Au wire, a hard Cu wire (Cu-H), and a soft Cu wire (Cu-S). All wire types used are 25 µm in diameter, 99.99% purity, and manufactured by MK Electron Co. Ltd., Yongin, Korea. Table 2-1 shows the basic mechanical properties of the three wire types. The values for Vickers hardness were measured on the wire cross-sections made perpendicular to the wire main axis. Using the deformability characterization method reported in [109], it is found that the FAB made with Cu-S wire is softer than that made with Cu-H wire.

Bonding is performed at a nominal heater plate temperature of 125 °C, resulting in an actual chip temperature of ≈ 110 °C. A commercial ceramics bottleneck capillary having a hole diameter of 35 µm and a chamfer diameter of 51 µm is used. During the formation of FABs with the copper wires, a homogeneous mixture of 95% N_2 and 5% H_2 is used as a shielding gas to prevent the oxidation of the molten FAB metal during solidification. The flow rate of the shielding gas is set to 0.48 l/min.

The ball bond process optimization is aimed at obtaining maximum bond strength while controlling the bonded ball geometry (diameter and height). It is used to find the optimum levels of the process parameters (ultrasound, bond force, etc.) that result in maximum bond strength for the targeted bonded ball geometry.

2.1.1 Procedure

Ball bonding processes are optimized for the three wire types using a four-step procedure: (i) crescent bond optimization; (ii) FAB optimization; (iii) ball bond IF optimization; and (iv) ball bond US optimization. Each of these steps is described below.

Table 2-1. Wire Properties

Property	Au	Cu-H	Cu-S
Breaking load [gf]	10.0	12.6	10.1
Elongation [%]	2.8	14.9	11.2
Vickers hardness	50.0	57.8	55.5

The crescent bond parameters are optimized using an iterative method reported in [110], and shown in Table 2-2. These parameters result in symmetrical bonds with consistent wire tail length (length of the wire below the capillary tip), without any signs of fish tailing (peeling). The unit % is used for the US parameter. It is proportional to the US vibration amplitude where 1% is equivalent to a peak to peak amplitude of 26.6 nm measured at the center of the transducer tip.

Next, the parameters for the EFO process are optimized to obtain a 50 µm diameter FAB. To this end, 30 FABs are made with three different levels of EFO current (10 FABs for each current level), and fixing all other EFO parameters such as tail length to 500 µm, EFO time to 0.4 ms, and electrode to wire (E-W) distance to 300 µm. The FAB diameters are measured using an optical microscope and fitted with a second order polynomial against the EFO current. From the fitted curve, the EFO current corresponding to a 50 µm FAB is determined. An example plot visualizing this procedure is shown in Fig. 2-1. Table 2-3 shows the resulting EFO currents. Using this optimized EFO current, sample FABs are made as shown in Figs. 2-2 (a), (b) and (c). The FAB diameters are verified to be 50 ± 0.5 µm.

An IF value, which is nominally three times as high as the subsequent BF value is used (3-to-1 ratio). US is present only after impact. The nominal parameters are given in Table 2-

Table 2-2. Crescent bond parameters

Parameter	Au	Cu-H	Cu-S
Impact force [mN]	700	800	700
Bond force [mN]	350	500	700
Ultrasound [%]	65	75	75
Bond time [ms]	25	65	65
Pre-ultrasound, off at impact [%]	0	30	30

Table 2-3. EFO currents to obtain 50 µm diameter FABs

	Au	Cu-H	Cu-S
Current, I [mA]	58.59	81.63	83.25

4 . To verify the nominal IF/BF ratio, the actual forces applied by the machine are recorded in real-time by the proximity sensor attached to the wire clamp of the bonder [110]. Example force profiles are shown in Figs. 2-3 (a), (b), and (c). It is observed that the actual IF/BF ratio is about 2.9.
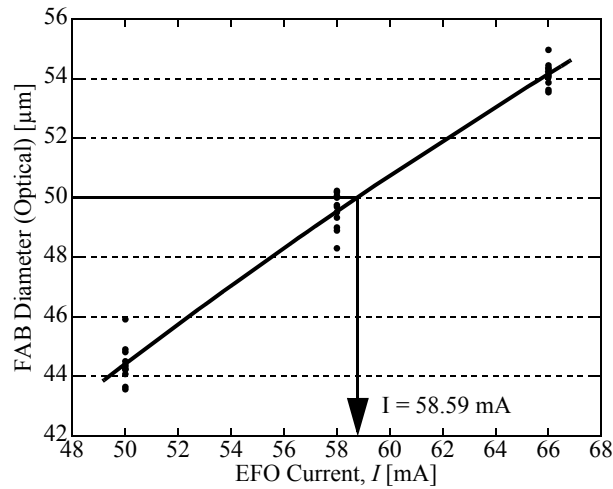
Fig. 2-1. FAB diameter vs. EFO current for Au wire. Thick solid line is second order polynomial fit. EFO time = 0.4 ms.
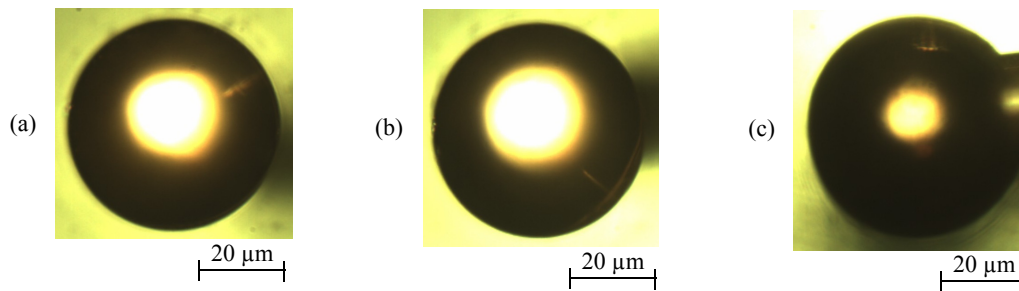
Fig. 2-2. Optical micrographs of example FABs obtained with (a) Au, (b) Cu-H, (c) Cu-S wires.

Table 2-4. Ball bonding parameters

Parameter	Au	Cu-H	Cu-S
Impact force [mN]	800	1200	1200
Bond force [mN]	266	400	400
Bond time [ms]	25	25	25
Ultrasound [%]	25-70	50-86	50-86

29

The IF values are adjusted such that the bonded ball geometries were the same with each of the three wires with a target bonded ball diameter measured at the capillary imprint (BDC) of ≈ 60 μm. To remove the effect of US enhanced deformation (UED) [22], the US level is kept at the minimal level required for the bond formation with each of the three wire types. The nominal BF is then calculated to maintain the 3-to-1 ratio.

The chips with Al metallized bond pads used for the ball bond process optimization trials were supplied by Besi Esec (Cham, Switzerland). An example is shown in Fig. 2-4 mounted on a PLCC44 lead frame. On each chip, ball bonding is performed by varying the US from the minimum US level required for bonding, in steps to high US level when the ball is heavily deformed. For levels lower than the US ranges specified in Table 2-4, ball non-stick on pads (NSOPs) are observed.
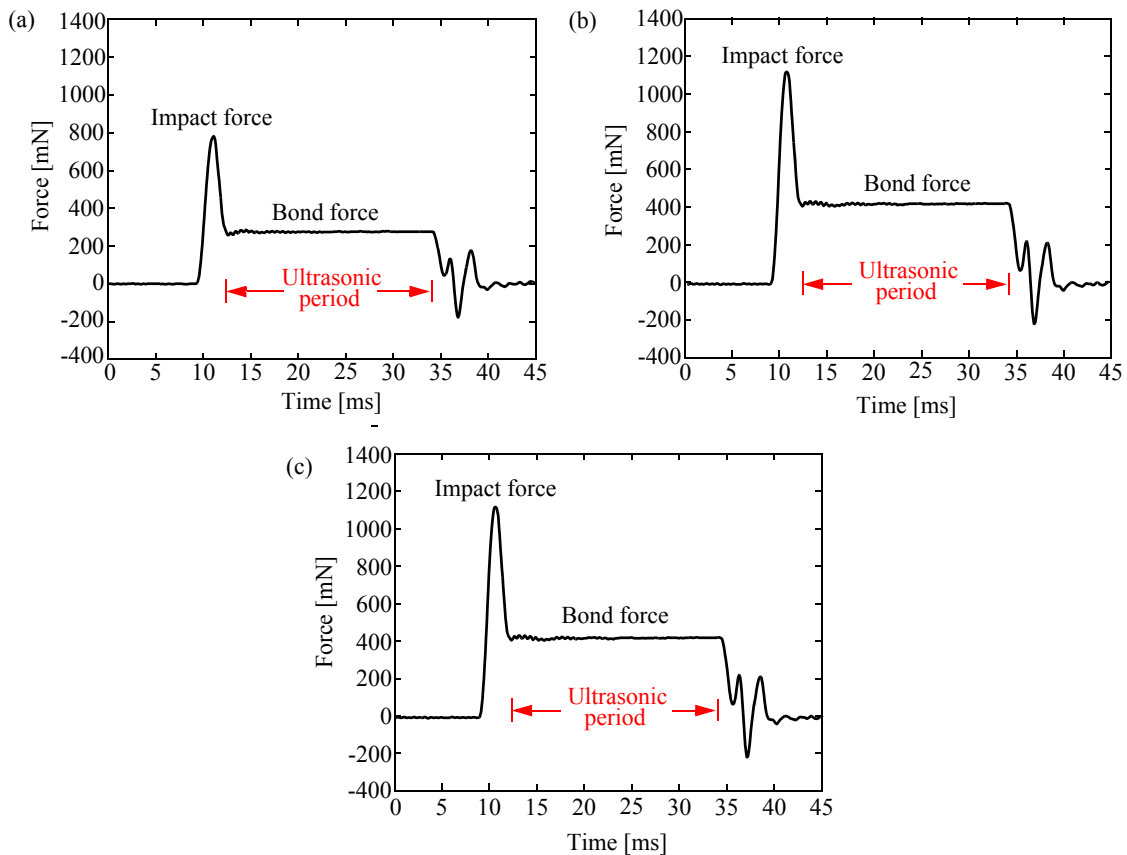
Fig. 2-3. Example measured force profiles of ball bonding process with (a) Au, (b) Cu-H and Cu-S wires.

30

A set of 14 bonds using different US values for each is made per chip, repeated on ten chips. Example micrographs of typical optimized ball bonds with Au, Cu-H, and Cu-S wires are shown in Figs. 2-5 (a), (b), and (c), respectively. BDC and ball height (BH) values are measured at the capillary imprint using an optical microscope. Then the balls are sheared, and the shear force (SF) is recorded. Example micrographs of the pad morphology after shearing the ball bonds with Au, Cu-H, and Cu-S ball bonds are shown in Figs. 2-6 (a), (b), and (c), respectively.

The shear strength (SS) of the ball bond is defined as the shear force divided by the cross-sectional area A, where $A = \pi \, (BDC/2)^2$. The variations of BDC, BH, and SS as a function of US are plotted in Figs. 2-7, 2-8 and 2-9, for the processes with Au, Cu-H, and Cu-S wires, respectively. The optimum US levels are selected at the point (indicated by arrows
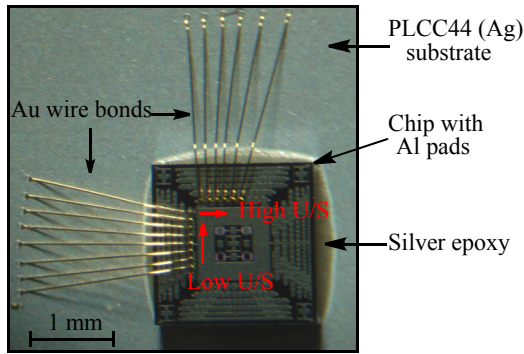
Fig. 2-4. Test chip used for ball bonding process optimization.

(a)   (b)   (c)
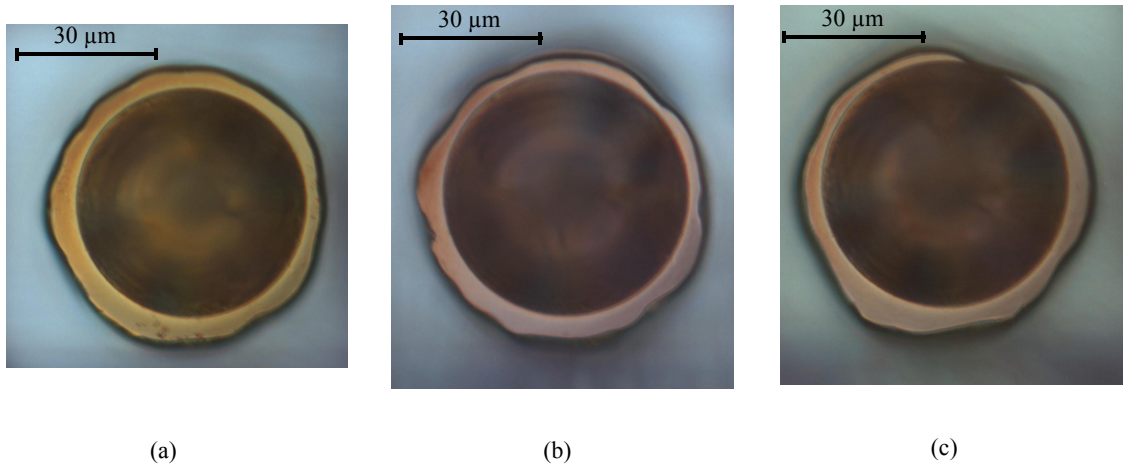
Fig. 2-5. Example micrographs of optimized ball bonds made with (a) Au, (b) Cu-H, and (c) Cu-S wires.

31

in the figures) when a sharp increase in BDC and decrease in BH is observed. This is the maximum US at which there is no UED, i.e. the ball deformation is due to the normal IF alone. The values for the processes with Au, Cu-H, and Cu-S wires are 51%, 70%, and 66%, respectively, as indicated by the red arrows in Fig. 2-7.

2.1.2 Evaluation of Processes

It is observed that ball bonds made with Cu wires have higher SS than those made with Au wire. This is consistent with the findings reported in [103]. One of the reasons for the higher SS values is possibly the higher US stress supported by Cu without yielding. If the US
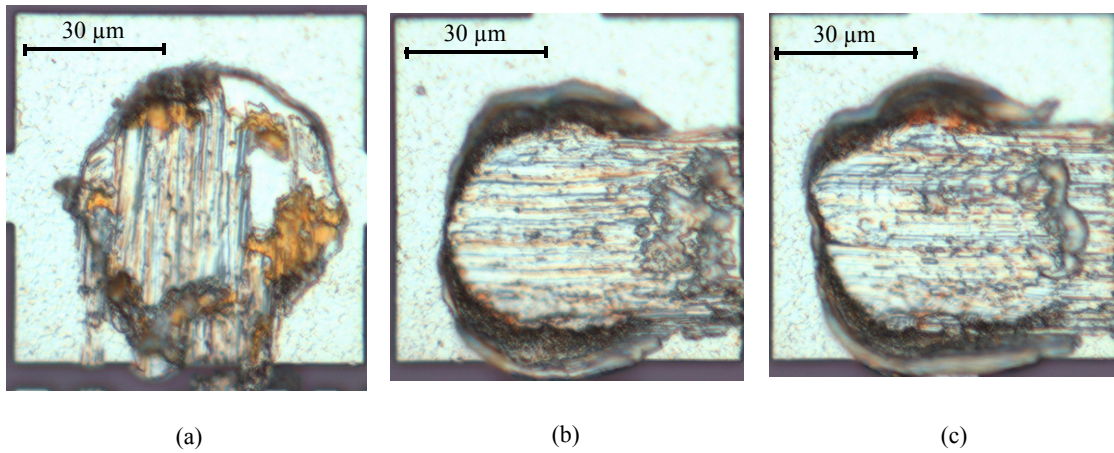
Fig. 2-6. Example micrographs of pad morphology after shearing the ball bonds with (a) Au, (b) Cu-H, and (c) Cu-S wires.
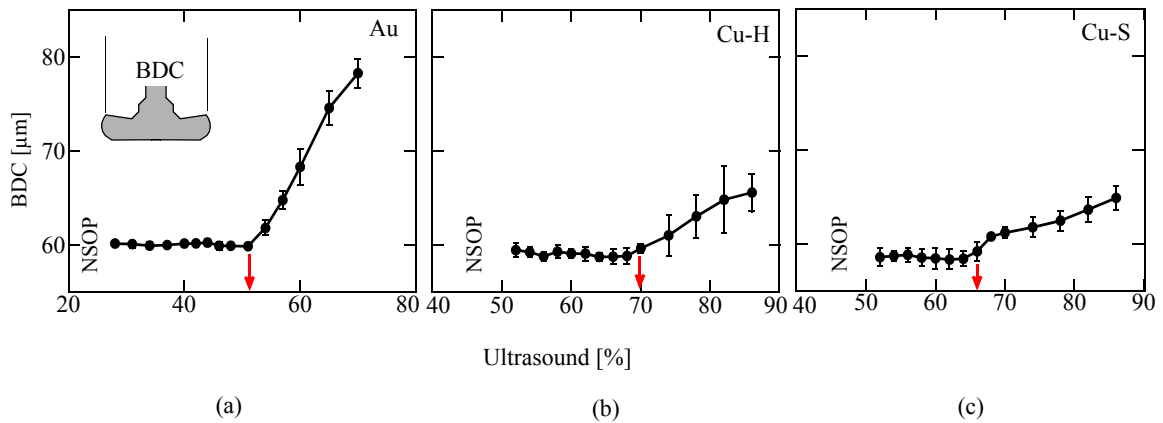
Fig. 2-7. Ball bond diameter (BDC) vs. ultrasound for (a) Au, (b) Cu-H and (c) Cu-S wire process.

32

stress induced to the ball is larger than the yield strength, additional UED occurs, and the bonded ball dimensions are out of specifications. Since Cu has a tensile strength of about 210 MPa which is higher than that of Au (120 MPa) [111], higher US levels can be used without UED, resulting in higher shear strengths.

In order to quantify the process capability (i.e. the ability of the process to produce output within specification limits), the c_{pk} value [112] is calculated using Eqn. 2-1

$$c_{pk} = \frac{\mu - LSL}{3\sigma} \qquad \qquad (2\text{-}1)$$
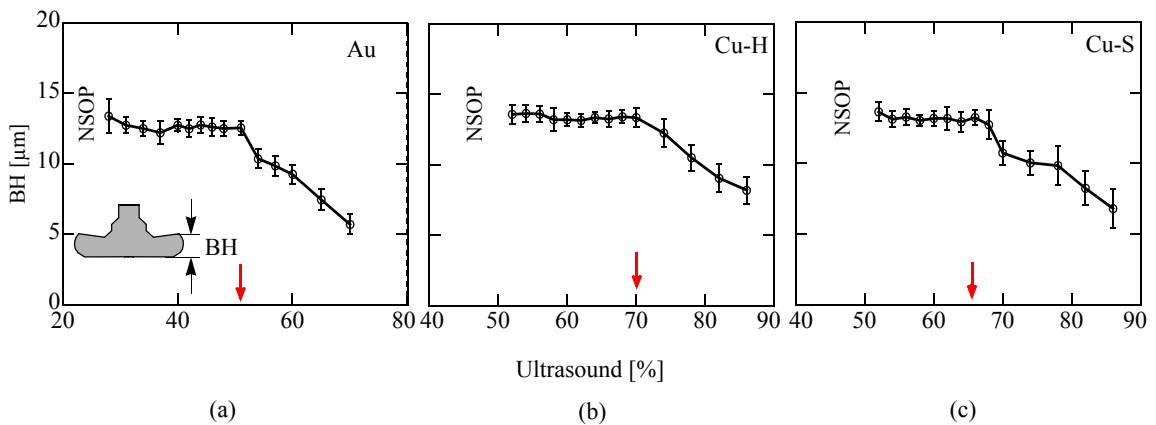
Fig. 2-8. Ball bond height vs. ultrasound for (a) Au, (b) Cu-H and (c) Cu-S wires.
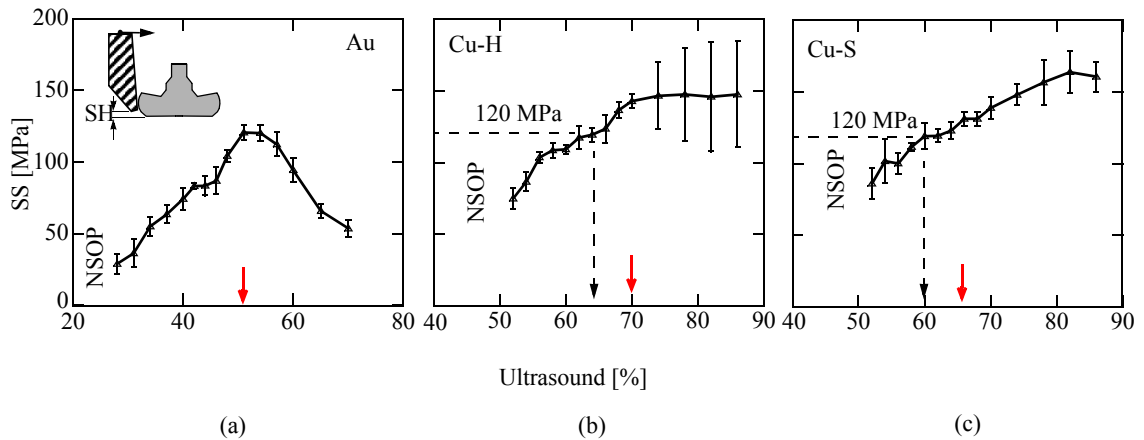
Fig. 2-9. Ball bond shear strength vs. ultrasound for (a) Au, (b) Cu-H and (c) Cu-S wires. 'SH' denotes shear height.

33

where μ, *LSL*, and σ are the average, lower specification limit, and standard deviation of the ball bond shear strength, respectively. From the EIA/JEDEC Standard 22-B116 [26], *LSL* is defined to be 65.2 MPa.

The c_{pk} values are determined for various US levels for each of the three wire types and plotted in Figs. 2-10 (a), (b), and (c), respectively, together with parabolic curve fits. The fits are used to estimate the maximum c_{pk} values at the optimized US parameter. These are found to be 2.3 ± 0.9, 3.3 ± 1.4, and 3.7 ± 1.2 for Au, Cu-H, and Cu-S wires respectively.

The optimal US levels were chosen from Fig. 2-7 (start of BDC increase). The optimum US parameter for Cu-H is slightly higher than that of Cu-S. However, the maximum of the parabolic fit in Fig. 2-10 (c) is observed at a US value higher than that previously deter-mined from Fig. 2-7. This apparent discrepancy may be attributed to the fact that the para-bolic model used for the fit is a strongly simplified model for this type of process and therefore less suited to evaluate an optimal ultrasound level. The discrepancy might further be attributed to the relatively large uncertainty of the parabolic fit. In particular, the stan-dard deviation of SS measured for high US levels is relatively large, adding to the uncer-tainty.
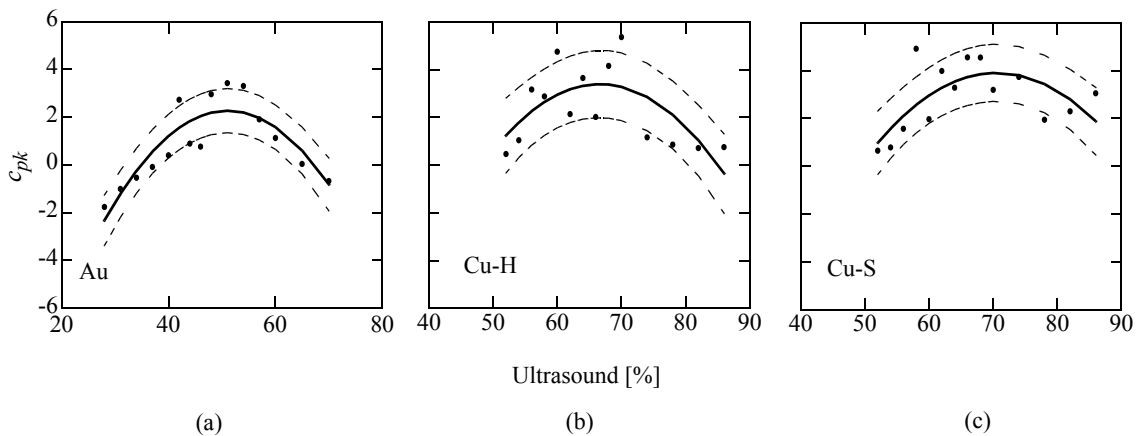
Fig. 2-10. Shear strength c_{pk} values with a parabolic fit (dashed lines indicate ±1 standard deviation) vs. ultrasound for (a) Au, (b) Cu-H, and Cu-S wires.

2.1.3 Reduced Ultrasound Process

The maximum shear strength c_{pk} value determined for Cu ball bonding is approximately 1.5 times as large than that of the Au ball bonding process. However, the US level required for Cu is approximately 30–37% higher than that required for Au. The higher US results in higher force induced to the pad during the bonding process, which increases the pad stress and therefore risk of underpad (or chip) damage.

One way to reduce this stress is to reduce the US level during the process. A trade-off is expected between such a parameter reduction and achieving a high bond quality. For the Cu ball bonding processes, the US level is reduced from the optimum value to a level at which a SS equivalent to that of Au ball bonding (120 MPa) is obtained. In case of Cu-H wire, the US level is reduced to 66% and for Cu-S wire, it is reduced to 60%, as indicated by the dashed arrows in Figs. 2-9 (b), and (c), respectively and shown in Table 2-5. While this causes the average SS to fall by $\approx 15\%$, the c_{pk} (3.4 ± 1.3 and 3.0 ± 1.1 for reduced US Cu-H and Cu-S process, respectively) does not change significantly. Thus, a successful Cu ball bonding operation can be run at $\approx 7 - 9\%$ lower US level than the conventionally optimized value. The actual amount of reduction in pad stress by using the reduced US process is reported in Section 2.3.

2.2 Ultrasonic Tangential Force

2.2.1 Test Chip

A test chip has been designed in the Microjoining Laboratory of the University of Waterloo and developed using a standard 0.7 μm double metal, single polysilicon CMOS process of

Table 2-5. Ultrasound settings for optimized and reduced ball bonding process

Wire type	Optimized US	Reduced US
Au	51%	--
Cu-H	70%	66%
Cu-S	66%	60%

AMI Semiconductor (Oudenaarde, Belgium). An example test chip is shown in Fig. 2-11. The die size is 4×2.5 mm^2. The chip has a number of independent test structures with bonding test pads (standard Al pads). Test structure A shown in Fig. 2-12 is used in this research.
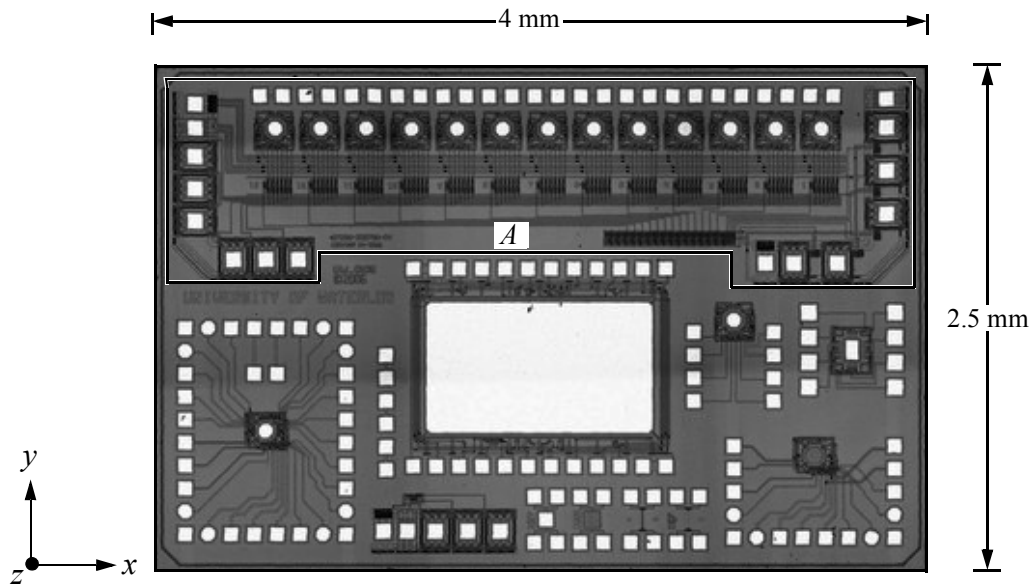
Fig. 2-11. Optical micrograph of the test chip with test structure A. Ultrasound is in y direction.
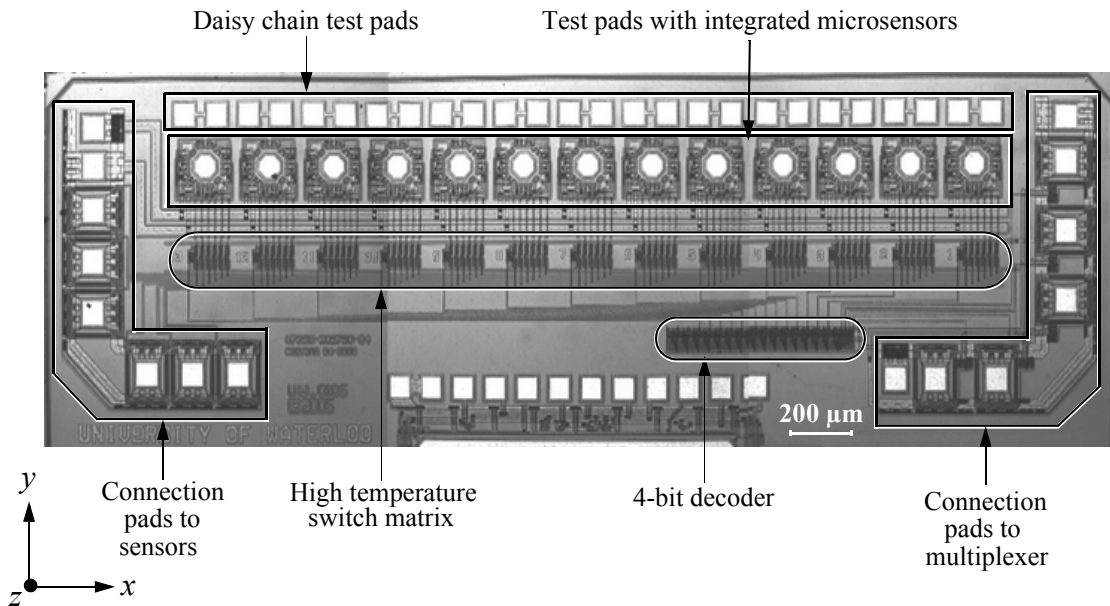
Fig. 2-12. Optical micrograph of the test structure A. Ultrasound is in y direction.

Test structure *A* has thirteen octagonal shaped bonding test pads. Each test pad, as shown by an optical micrograph in Fig. 2-13, has Si resistors integrated adjacent to it. The design and operation of these sensors is similar to those reported in [5] and is described briefly in Section 2.2.2.

The test pads are addressed using an on-chip multiplexer circuit consisting of a 4-bit decoder and a high temperature switch matrix as shown in Fig. 2-12. The sensing and multiplexer address pads are placed at left and right edges. These pads have to be connected with wire bonds prior to the measurement. The connection pad wires do not interfere with the wires bonded to the test pads during the measurement.

2.2.2 Microsensor Design

Four serpentine shaped (strain gauge) type sensing elements R_1, R_2, R_3, and R_4, are placed outside of the pad metallization at an average distance of 65 μm from the pad center, as shown in Fig. 2-14 (a). An element has a room temperature resistance of 4.49 kΩ, a sensitive area of 17.5 × 17.5 μm, forces the current into the $[1\bar{1}0]$ direction of the Si crystal, and is covered by dielectric layers of the CMOS process. The sensitive material is highly doped p^+-diffusion, and the effect exploited is the piezoresistive effect, i.e. the change in resistance caused by a change in mechanical stress at the resistor location [87–90]. The bulk of the chip is *p*-type Si.
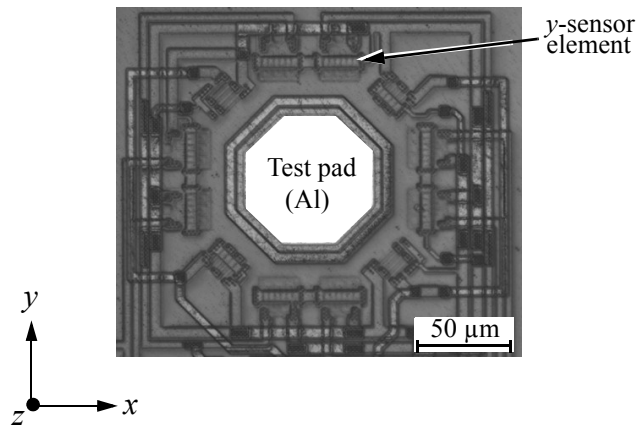
Fig. 2-13. Optical micrographs of the test pad with microsensors integrated next to it. Ultrasound is in *y* direction.

37

The sensing elements are connected in a Wheatstone bridge as shown in Fig. 2-14 (b). The response of the sensor (signal) is

$$M = \frac{V_H - V_L}{V_S} \tag{2-2}$$

where V_S is the constant voltage operating the full Wheatstone bridge. The value of M is non-dimensional and expressed in mV/V.

Applying Kirchhoff's circuit law leads to

$$\frac{V_H - V_L}{V_S} = \frac{(R_1 \cdot R_4) - (R_2 \cdot R_3)}{(R_1 + R_3) \cdot (R_2 + R_4)} \tag{2-3}$$

Since all elements are designed the same, their electrical resistances R_i ($i = 1,...,4$) are expressed as the sum of a common base resistance R and individual resistance ΔR_i. The relative resistance change of one element is defined as $r_i = \Delta R_i / R$. Thus,

$$R_i = R + \Delta R_i = R(1 + r_i) \tag{2-4}$$

With Eqns. 2-2 – 2-4 and assuming $R_i \gg r_i$, M simplifies to
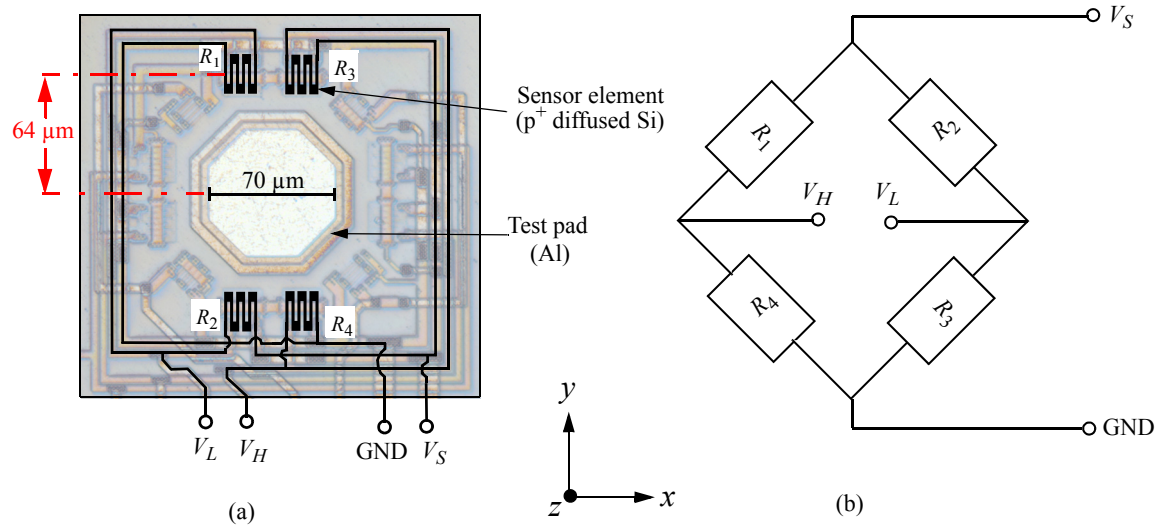
Fig. 2-14. (a) Layout and identification of connections to microsensor elements next to test pad; (b) Electrical circuit diagram. Ultrasound is in y direction.

$$M \approx \frac{r_1 + r_4 - r_2 - r_3}{4} \tag{2-5}$$

Thus, the sensor signal is approximately equal to the average of the values ($r_1, -r_2, -r_3, r_4$). Due to the symmetry expressed by Eqn. 2-5, the Wheatstone bridge is largely "blind" to all changes of resistance that are same for all four bridge elements. This is the case for temperature induced resistance changes.

The sensor signal M is related to the mechanical stress changes by the formula for the relative resistance change of a sensor element,

$$M = \left.\frac{\Delta R}{R}\right|_{\phi = 90°} = \left(\frac{\pi_{11} + \pi_{12} - \pi_{44}}{2}\right)\sigma_{xx} + \left(\frac{\pi_{11} + \pi_{12} + \pi_{44}}{2}\right)\sigma_{yy} + \pi_{12}\sigma_{zz} \tag{2-6}$$

where σ_{xx}, σ_{yy}, and σ_{zz} are the changes of stress tensor components averaged over the element location, π_{11}, π_{12} and π_{44} are the piezoresistive coefficients of the p^+ silicon, and ϕ is the resistor angle with respect to the x-axis. Typical values of π_{11}, π_{12} and π_{44} are found in [5, 89] are 0.11×10^{-10} Pa^{-1}, 0.1×10^{-10} Pa^{-1} and 7.5×10^{-10} Pa^{-1}, respectively.

Since the values of (π_{11}, π_{12}) $\ll \pi_{44}$, and the fact that the US vibrations are in the resistor direction (y-direction), $\sigma_{yy} \gg \sigma_{xx}$, σ_{zz}. Thus, Eqn. 2-6 reduces to

$$M = \left.\frac{\Delta R}{R}\right|_{\phi = 90°} \approx \left(\frac{\pi_{11} + \pi_{12} + \pi_{44}}{2}\right)\sigma_{yy} \tag{2-7}$$

Therefore, this design is selectively sensitive to the stress field originating due to US vibrations at the bond interface. The frequency range of the microsensor exceeds several MHz [5]. The US frequency (100–130 kHz) is low enough not to excite the microsensor resonance frequency. In addition, the US frequency does not excite the parasitic vibrations of the measurement setup itself as is evident from the measured signals.

2.2.3 Microsensor Calibration

The microsensor is calibrated for US tangential force F_T using a standard sensor [5] with a similar design provided by Besi Esec, Cham, Switzerland. This standard sensor itself has a sensitivity of 10.2 ± 0.5 mV/V/N [5]. To calibrate the microsensor, ball bonding tests are

performed with a 50 μm diameter Au free air ball (FAB) on an ESEC 3100 automatic ball-wedge bonder. This bonder offers a software feature that allows to split the bonding operation into multiple segments. The duration, BF, and US level for each segment can be adjusted separately, resulting in parameter profiles of varying complexities. The US parameter profile for the calibration test is defined in Table 2-6. The tests are performed at room temperature.

A high normal BF of 1000 mN for all segments ensures that there is no friction between the ball and pad during the calibration. The absence of interfacial sliding is confirmed by the weakness of the 3rd harmonic of F_T, the values of which do not exceed 0.05 mV/V. Since the US levels selected are lower than those required for bonding, the deformed FAB does not stick to the pad, and is removed from the pad and subsequently bonded at the second bond position defined on the package. For the next test, a fresh FAB is fired. The tests are repeated on ten samples each of the microsensor and the standard sensor.

The microsensor response M has a high frequency (US frequency) and a low frequency content. For simplicity, only the amplitude of US frequency, E is used. It is evaluated using a method described in [5]. An example E from the calibration test is shown in Fig. 2-15 (a). Values of E are evaluated as the average of the microsensor response for each US level in Fig. 2-15 (a). Figure 2-15 (b) shows a linear relationship between the evaluated values from the microsensor and from the standard sensor. The calibration factor of the microsensor is evaluated as the slope of the linear fit in Fig. 2-15 (b) and is determined to be $f_{calib} = 17.27 \pm 0.99$ mV/V/N. The error value includes the fit error of the microsensor and the sensitivity error of the standard sensor.

Table 2-6. Ultrasound parameter profile for calibration experiment

	Segment number									
	Impact force = 1000 mN		Bond force = 1000 mN							
	1	2	1	2	3	4	5	6	7	8
Time [ms]	1	1	10	10	10	10	10	10	10	10
Ultrasound [%]	0	0	2	4	6	8	10	12	14	16

To study the effect of temperature on the sensitivity of the microsensor, the calibration is repeated at 100°C. The calibration factor of the microsensor at 100°C is 16.52 ± 0.86 mV/V/N, which is ≈ 4.3% lower than that measured at room temperature (17.27 mV/V/N). It is noted that f_{calib} does not vary significantly due to frictional heating during bonding. This is due to the cooling of the bonding zone (interface) due to heat transfer from the hot bond pad to the cooler ball/capillary during touchdown, which precedes the heating effect due to US friction. Studies of the real-time temperature have shown that the effective temperature rise at the interface (due to both cooling and heating effects) does not exceed 10°C [91–94]. The temperature rise at the sensor location itself is significantly lower than that at the interface.

2.2.4 Experimental setup

The microsensor test chip is die bonded to a gold plated polyimide substrate supplied by Besi Esec, Cham, Switzerland, using a commercially available Ag filled epoxy adhesive. The sensor channels and the multiplexer addressing channels are connected to the terminals on the substrate by Au wire bonds as shown in Fig. 2-16. A constant DC voltage of $V_S = 3$V is applied to the microsensor.
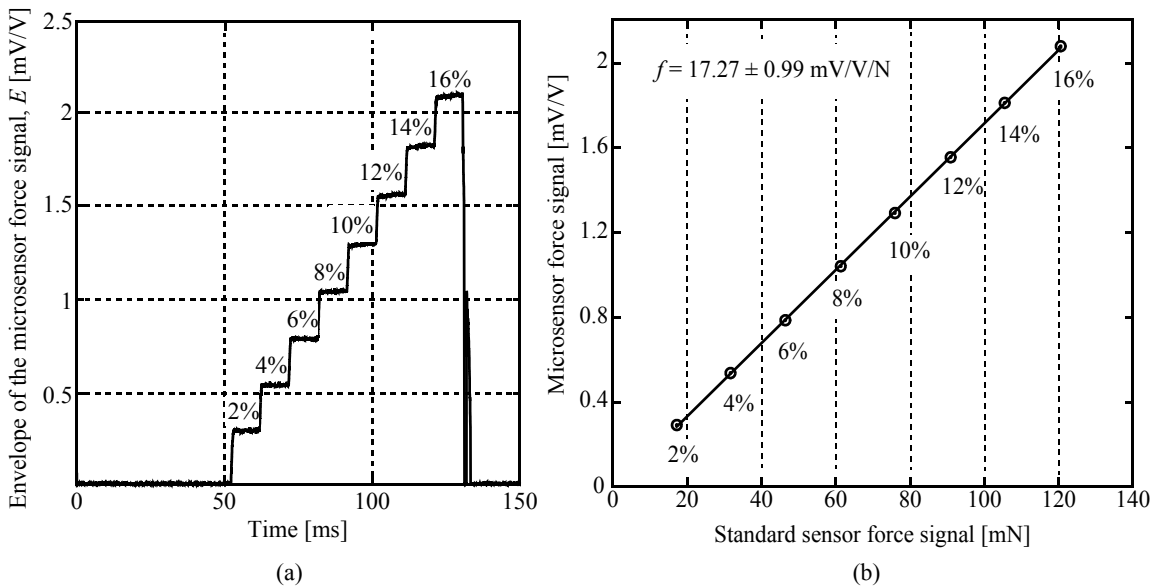
Fig. 2-15. (a) Example microsensor response for the calibration test. (b) Calibration of the microsensor using a standard sensor [5]. The numbers in % indicates the ultrasound level.

41

Ball bonding using the optimized US level for Au, Cu-H, and Cu-S wires (shown in Table 2-5) is performed on the test pads with each of the three wire types, and the real time signals of the microsensor are recorded on a PC. The measurements are performed on 10 chips. An example bond on the octagonal shaped test pad between the sensing elements of the microsensor is shown by the SEM micrograph in Fig 2-17.

2.2.5 Results and Discussion

The signals of US tangential force F_T obtained during thermosonic ball bonding with Au, Cu-H, and Cu-S wires are shown in Figs. 2-18 (a), (b), and (c), respectively. Each of these
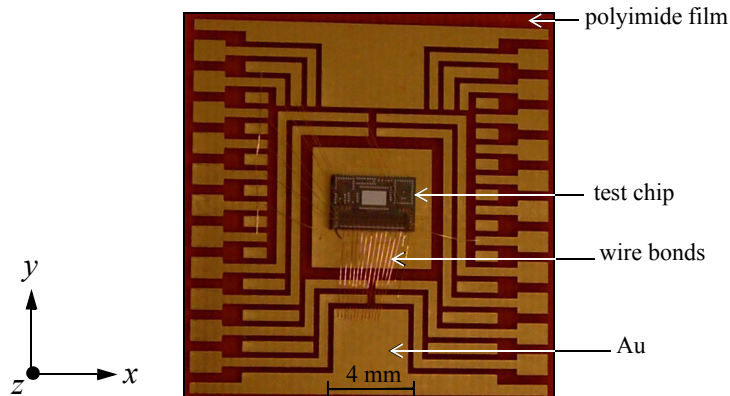
Fig. 2-16. Microsensor test chip attached on gold metallization of polyimide substrate. Ultrasound in y direction for bonding tests.
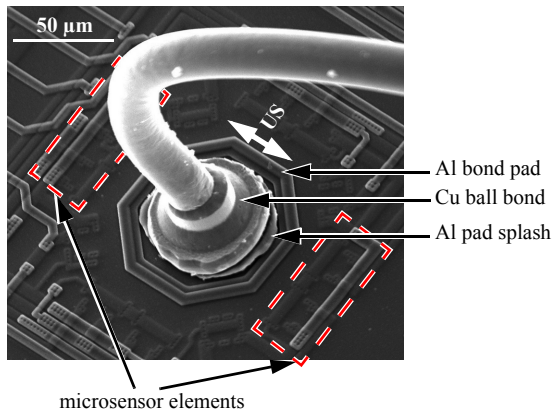
Fig. 2-17. SEM micrograph of a ball bond on the microsensor test pad (shown here is an optimized ball bond performed using Cu-H wire).

42

signals consist of approximately 3,125 cycles of US vibration. Hence, the signals appear as filled areas. The waveform of the signal between 3 and 4 ms after touchdown is shown adjacent to the signal for each wire type. The harmonics of the microsensor signals obtained with Au, Cu-H, and Cu-S wires are shown in Figs. 2-19 (a), (b), and (c), respectively.

The results obtained with Au wire are consistent with those reported previously [11, 21]. Between 1 ms and 1.5 ms after US dissipation starts, a break-off in the microsensor signal is observed, characterized by a sharp fall in the first harmonic and a sharp rise in the third
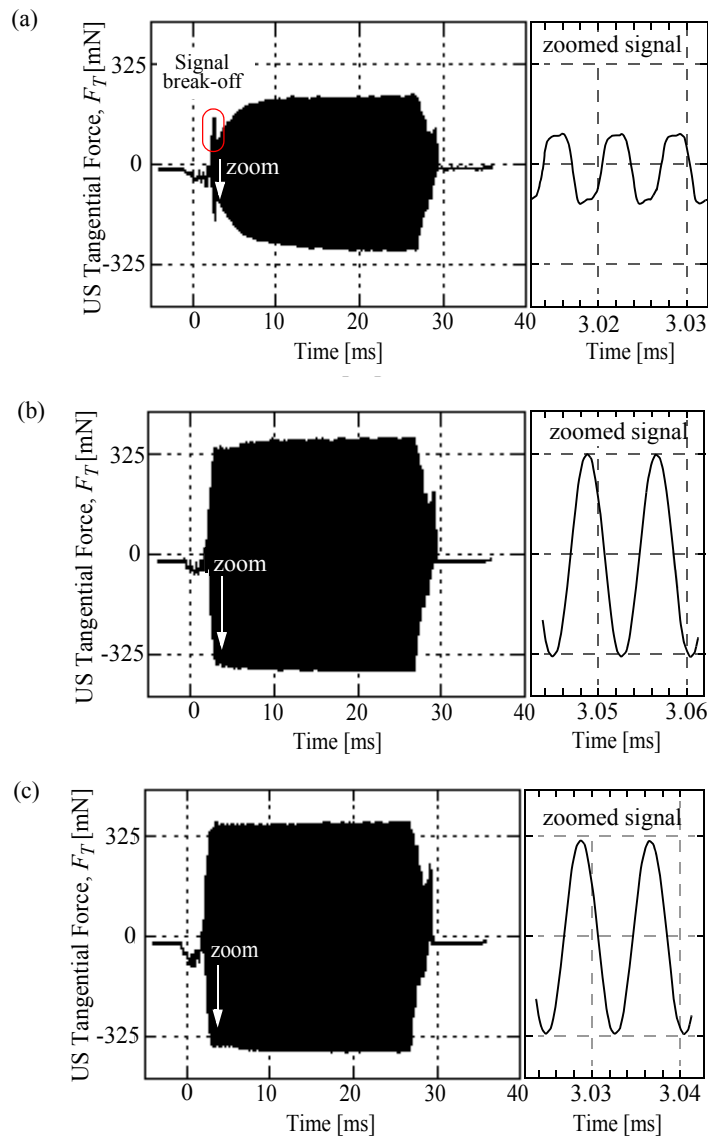
Fig. 2-18. (a) Example F_T signals measured by the microsensor for (a) Au, (b) Cu-H, and (c) Cu-S ball bonds made with optimized US settings shown in Table 2-5.

43

harmonic. During this period, the waveform of the signal becomes cropped as shown in Fig. 2-18 (a), indicating a harmonically driven stick-slip motion at the bond interface.

The cropped signal waveform is mathematically constructed out of the first harmonic and of the other odd harmonic amplitudes, as shown by an example (first and third harmonics only) in Fig. 2-20. When the third harmonic amplitude is low or not present at all, the waveform does not deviate from the sinusoidal shape. Since the cropped waveform indicates stick-slip friction, it follows that the third harmonic is an indicator of friction at the interface.
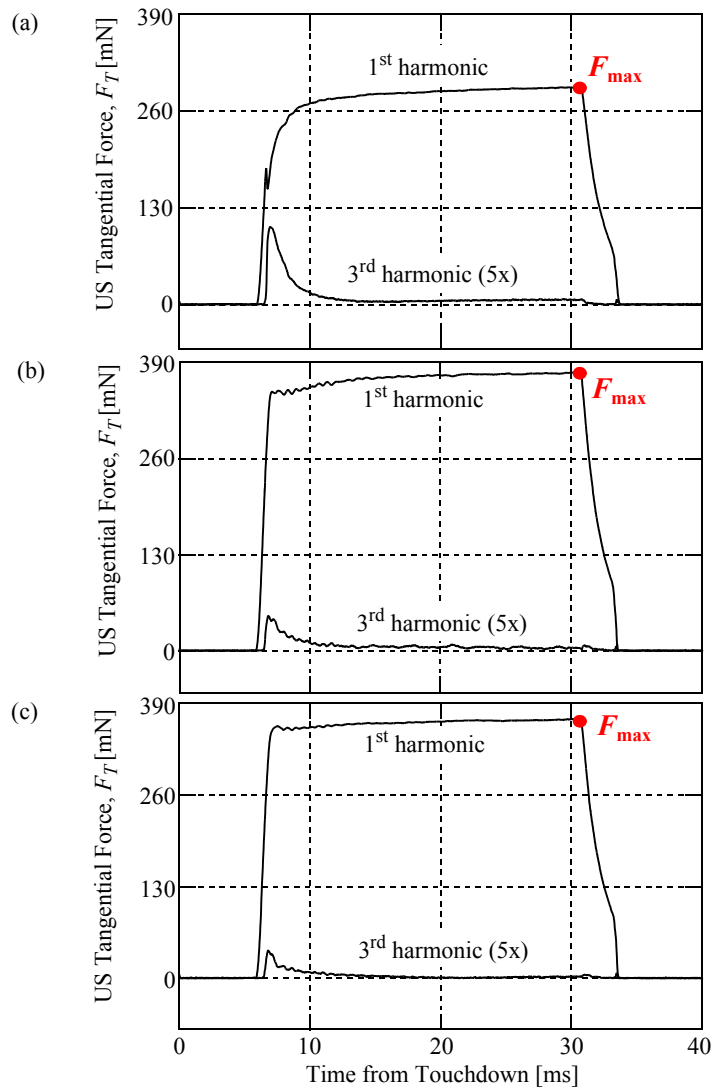
Fig. 2-19. Amplitudes of harmonics from F_T signals of (a) Au, (b) Cu-H, (c) Cu-S ball bonds shown in Fig. 2-18 with optimized US settings shown in Table 2-5.

In contrast, in the Cu ball bonding process, as soon as the US dissipation starts, the force signal rises rapidly and no signal break-off is observed. The relative amount of the third harmonic is approximately 5 times smaller than in the Au-Al ball bonding process, as shown by the typical curves of amplitude ratio of the third by the first harmonic in Fig. 2-21. The averages ± standard deviations of the maximum amplitude ratio of the third by the first harmonic are 13.6 ± 0.4 %, 2.8 ± 0.3 %, and 2.4 ± 0.3 % for the Au, Cu-H, and Cu-S ball bonding, respectively. The cropped sinusoidal waveform explaining the interfacial stick-slip motion is not evident in the Cu ball bonding process. While reduced in relative

1st harmonic

+

3rd harmonic

=

Cropped sinusoidal
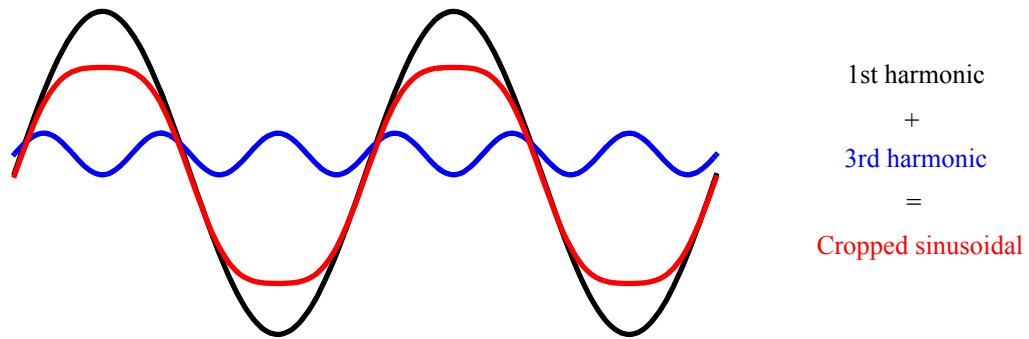
Fig. 2-20. Mathematical construction of the cropped waveform from the first and third harmonic amplitudes of an example sine wave.
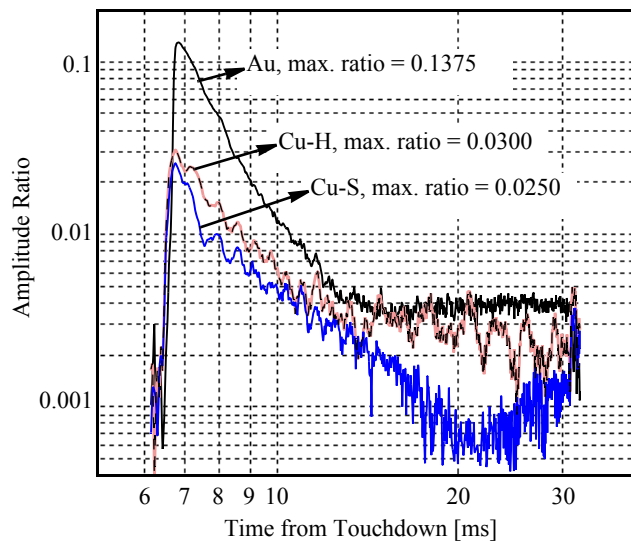
Fig. 2-21. Ratios of 3rd by 1st harmonic amplitudes vs. time.

45

magnitude compared to the Au/Al process, the amount of stick-slip friction in the Cu/Al is still an important if not the leading mechanism for a successful Cu ball bond.

2.2.5.1 Ultrasonic Stresses at Bond Pad and Sensor Location

The US tangential force F_T induces a mechanical stress field at the bonding interface (US pad stress σ_{US}^{bond}) and at the microsensor element location (US microsensor stress, σ_{US}^{sen}). Since the bonded ball diameters are constant (≈ 58 µm), σ_{US}^{bond} is proportional to F_T in the case of a finished bond. The maximum US force induced to the pad is reached at the points F_{max} shown in Figs. 2-19 (a), (b), and (c). Thus, the maximum value of σ_{US}^{bond} is

$$\sigma_{max}^{bond} = \sigma_{yz}^{max} = \frac{F_{max}}{S} \approx \frac{F_{max}}{\pi \cdot (58 \text{ µm})^2/4} \tag{2-8}$$

The maximum value of σ_{US}^{sen} is estimated using Eqn. 2-7 and is

$$\sigma_{max}^{sen} = \sigma_{yy}^{max} = \frac{2 \cdot M_{max}}{\pi_{11} + \pi_{12} + \pi_{44}} \approx \frac{2 \cdot M_{max}}{(0.11 + 0.1 + 7.5) \times 10^{-10}} \text{ Pa} \tag{2-9}$$

where M_{max} is the dimensionless maximum value of the microsensor response M (Eqn. 2-7). It is given by

$$M_{max} = F_{max} \cdot f_{calib} \tag{2-10}$$

where $f_{calib} = 17.27 \pm 0.99$ mV/V/N is the calibration factor of the microsensor (see Section 2.2.3). Table 2-7 shows the estimated values of σ_{max}^{sen} and σ_{max}^{bond} evaluated for Au, Cu-H, and Cu-S ball bonding processes. It is observed that in all three cases, $\sigma_{US}^{sen} \approx 12.7\%$ of σ_{US}^{bond}.

Table 2-7. Comparison of US stress acting at bond interface and sensor location

Wire type	σ_{max}^{sen} [MPa]	σ_{max}^{bond} [MPa]
Au	11.6 ± 0.1	91.3 ± 0.8
Cu-H	15.3 ± 0.1	120.7 ± 0.6
Cu-S	14.7 ± 0.2	116.0 ± 1.3

2.2.6 Bond Growth

To characterize the bond growth, ball bonds are made with Au, Cu-H and Cu-S wires using the respective optimized settings with bond time parameters varying in steps of at least 1 ms and not smaller than 2.5 ms. The tests are conducted on five chips on the daisy chain pads shown in Fig. 2-12. For each bond time, two bonds are made on each chip. The shear strengths for various bond time parameters are shown in Fig. 2-22.

It is observed that the rate of bond growth in Cu is faster than in Au. When bonded with the smallest time parameter (rounded to integer millisecond values) required for successful bonding (no NSOP), Au reaches only about 20% of its maximum shear strength (Fig. 2-22), and the microsensor signal [Fig. 2-19 (a)] is at 73% of its maximum value. The microsensor signal and the shear strength reach 90% of their maximum values at 2.9 ms and 16 ms after ultrasound on, respectively. In contrast, the bond with Cu wire reaches 50% of its maximum shear strength (Fig. 2-22), when bonded with the smallest time parameter (rounded to integer millisecond values), and the microsensor signal [Figs. 2-19 (b), (c)] is 94% of its maximum level. The microsensor signal and the shear strength reach 90% of its maximum level 1.1 ms and 6 ms after ultrasound on, respectively.
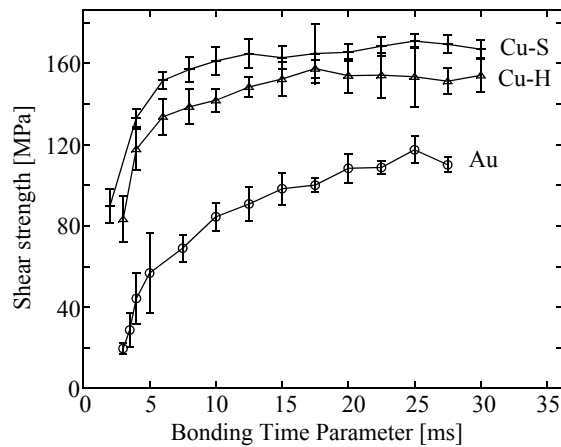
Fig. 2-22. Shear strength vs. bonding time plots for Au, Cu-H, and Cu-S ball bonds. Results shown only for parameters without NSOP occurring.

47

2.3 Reduction of Ultrasonic Pad Stress

In addition to ball bonding using the optimized US setting described in Section 2.2.5, ball bonds are made using the reduced US processes (for Cu-H and Cu-S wires) on the micro-sensor test pads. The measurements are performed on 10 chips for each setting listed in Table 2-5.

The statistics of F_{max} values measured for optimum and reduced ball bonding processes with Au, Cu-H, and Cu-S wires are plotted in Fig. 2-23. Table 2-8 shows the 95% confidence interval (C.I.) estimates of the average F_{max} values for each of the five processes. It
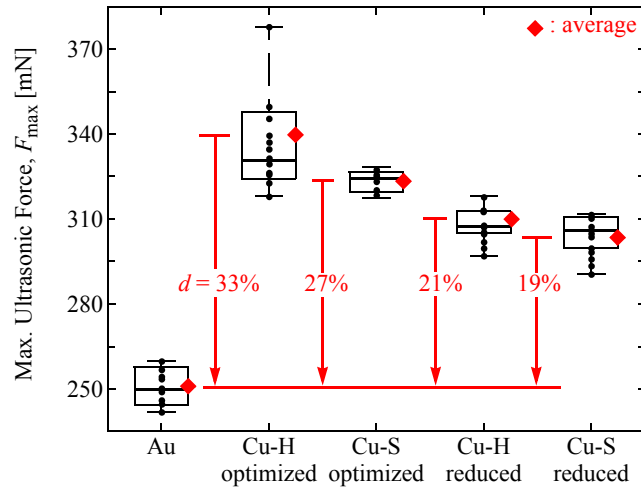
Fig. 2-23. Maximum ultrasonic force F_{max} for five processes.

Table 2-8. Statistical summary (Fig. 2-23)

Process	Max. Ultrasonic Force, F_{max} (95% C.I. estimates)	Difference to Au process (95% C.I. estimates)	
	[mN]	[mN]	[%]
Au, optimized	256.2 ± 5.6	—	
Cu-H, optimized	339.7 ± 14.8	83.5 ± 7.6	32.6 ± 2.9
Cu-S, optimized	324.7 ± 6.7	68.5 ± 4.1	26.7 ± 1.6
Cu-H, reduced	311.4 ± 4.9	55.2 ± 3.5	21.5 ± 1.4
Cu-S, reduced	304.4 ± 11.2	48.2 ± 5.2	18.8 ± 2.0

is observed that F_{max} for optimized Cu-H ball bonding process is $d = 83.5 \pm 7.6$ mN (i.e., about 33%) larger than that measured for the optimized Au ball bonding process. The comparison values for the remaining processes are given in Table 2-8. The reduced US Cu-S wire process succeeds in diminishing the force gap to the Au wire process by 42% (i.e., an absolute decrease of about 19%).

The gap can be reduced further or even closed completely by using even softer wires than Cu-S and/or modifying the BF value or the IF-to-BF) ratio. The IF-to-BF ratio used here is relatively high, resulting in considerable strain hardening of the Cu balls in particular [23, 105, 106]. Detailed studies on the effect of IF/BF on US pad stress is reported in Chapter 3.

2.4 Summary

Thermosonic ball bonding processes on test chips with Al metallized bonding pads are optimized with one Au and two Cu wire types, all 25 µm diameter, obtaining average shear strengths of more than 120 MPa. The process temperature is ≈ 110 °C. For the first time, in situ real time signals of US tangential force measured during thermosonic Cu ball bonding are reported. The analysis of the US force signal harmonics leads to the conclusion that the stick-slip frictional behavior is significantly less pronounced in Cu ball bonding process. The bond growth with Cu is approximately 2.5 times as fast as that in a comparable Au process.

Ball bonds made with Cu wire show at least 15% higher shear strength than those made with Au wire. The estimated maximum shear strength c_{pk} value determined for Cu ball bonding ($c_{pk} = 3.7 \pm 1.2$) is almost 1.5 times as large as that of the Au ball bonding process ($c_{pk} = 2.3 \pm 0.9$). However, the US level required for Cu is approximately 1.3 times than that required for Au. Consequently, about 30% higher US pad stress is measured. The accompanying higher stresses increase the risk of underpad damage.

One way to reduce ultrasonic bonding stresses is by choosing the softer of the two Cu wire types, resulting in a measured US force reduction of about 5%. A second way is to reduce the US level. While this causes the average shear strength to fall by 15%, the US force falls by 9%. The c_{pk} value does not change significantly, suggesting that a successful Cu ball bonding operation can be run with about 0.9 times the conventionally optimized US level.

The process adjusted in this way reduces the extra stress observed with Cu wire compared to that observed with Au wire by 42%.

3 Low-stress Thermosonic Cu Ball Bonding

Chapter 2 reported on a new, fast method to reduce the extra stress observed during Cu ball bonding. It has been shown that an US level, about 15% lower than the conventionally optimized level can be used in combination with a softer bonding wire material to obtain Cu ball bonds of comparable geometry and strength to that of Au ball bonds, while reducing the stress gap by $\approx 42\%$. The study had considered the material and the optimization of the US parameter. The effect of BF on bonding quality and pad stress was not investigated. This chapter presents bond process optimization results with an aim to answer the question: What is the synergistic effect of BF and US on the bonding quality, pad splash, and the stress delivered to the bond pad?

In this Chapter, Section 3.1 describes the experimental details and results pertaining to the optimization of processes. Section 3.2 reports on the Al pad splash measurements. It also describes the "noodle effect", which is used to explain the influence of US on the deformation of Cu bonded balls. The US pad stress results are shown in Section 3.3. Section 3.4 discusses the US/BF process window for low-stress Cu ball bonding. Finally, the results and conclusions of the study are summarized in Section 3.5.

The research reported in this Chapter has been published in parts in the *Proceedings of 11th IEEE Electronic Packaging Technology Conference* [113] and accepted for publication in *Microelectronics Reliability: Special Issue on Copper Wire Bonding* [114].

3.1 Experimental

Thermosonic ball bonding is performed using a 25 μm diameter Cu wire (MK Electron Co. Ltd., Yongin, Korea) on an automatic ESEC 3100 ball-wedge bonder (Besi Esec, Cham, Switzerland), having an ultrasonic frequency of 128 kHz. The Cu wire used in this study is same as the Cu-H wire described in Section 2.1. The bonding is performed at a nominal heater plate temperature of 150°C, resulting in a temperature of ≈ 138°C at the bond pad. The capillary, shielding gas type and flow rate are the same as those in Section 2.1.

3.1.1 Process Optimization

Ball bonding processes are optimized for eight levels of BF using the procedure described in Section 2.1.1. The details and results of process optimization specific to this study are reported below.

The crescent bond parameters to obtain consistent wire tail are shown in Table 3-1. Next, FABs are made with four different levels of EFO current (10 FABs for each current level) while fixing all other parameters, including tail length to 500 µm, EFO time to 0.4 ms, and electrode to wire distance to 300 µm. The FAB diameters are measured using an optical microscope and fitted with a quadratic polynomial against the EFO current. From the fitted curve, the EFO current corresponding to a 50 µm FAB is determined. A plot visualizing this procedure is shown in Fig. 3-1 from which the EFO current to obtain a 50 µm FAB is

Table 3-1. Crescent bond parameters

Impact force [mN]	800
Bond force [mN]	500
Bond time [ms]	75
Ultrasound [%]	65
Pre-ultrasound, off at impact [%]	30
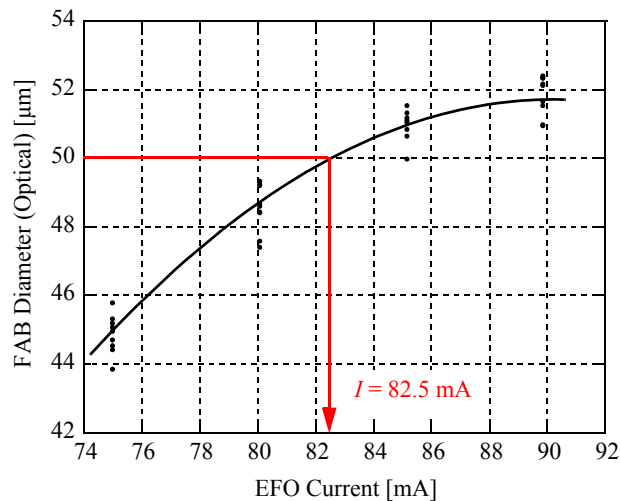
Fig. 3-1. FAB diameter vs. EFO current.

determined and is 82.5 mA. Using this current, sample FABs are made and the diameters are verified to be 50 ± 0.3 μm. A SEM micrograph of a typical 50 μm diameter FAB is shown in Fig. 3-2.

The value of IF for the ball bond process is optimized to obtain the targeted ball geometry measured using an optical microscope: BDC $\approx$ 58 μm and BH $\approx$ 15 μm. To this end, sample ball bonds are made for different values of IF ranging between 1000 mN to 1300 mN. The BF and US values are kept constant at 400 mN and 52%, respectively. The selected US level is the minimum required US for bond formation for the given BF, and is taken from the US optimization reported for Cu-H wire in Section 2.1. Thus, there is no additional US effect on ball geometry. The optimum value of IF is found to be 1200 mN. This value results in ball bonds with BDC $= 58.2 \pm 0.4$ μm and BH $= 14.2 \pm 0.3$ μm.

Ball bonding is performed on ten wire bonding test chips with Al metallized bond pads (Besi Esec, Cham, Switzerland), at levels of BF: 100, 200, 300, 400, 500, 600, 700, and 800 mN. For each BF level, ball bonding is performed by varying US from the minimum level required for bonding, B, in steps beyond a level D above which the ball experiences additional plastic deformation by US. The bonding time is fixed at 25 ms. A SEM micrograph of a typical bonded chip is shown in Fig. 3-3. On each chip, two identical sets of bonds are made (Fig. 3-3), where each set corresponds to the US levels from B and D for the given BF level. Bonding is repeated on ten chips, resulting in a sample of 20 bonds for each US/BF combination.

The variations in BDC and SS as a function of US for each of the levels of BF are shown in Figs. 3-4 and 3-5, respectively. Each BDC measurement is the average of the bonded ball
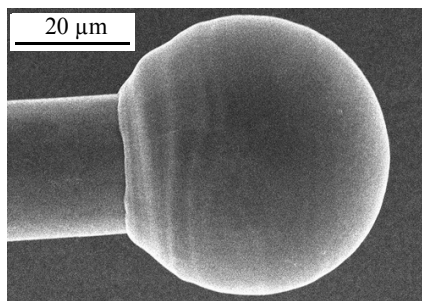
Fig. 3-2. SEM micrograph of a typical 50 μm diameter FAB. Current = 82.5 mA, firing time = 0.4 ms.

53

diameters in *x*- and *y*-directions at the capillary imprint. For US levels lower than *B*, ball non-stick on pad (NSOP) is observed. The optimum US levels are selected at the UED transition point *D*. Beyond the level *D*, for any additional increase in the value of US, a sharp increase in BDC is observed.

The SS results (Fig. 3-5) show that a maximum average shear strength of at least 130 MPa is obtained for each of the BF levels confirming the large size of the BF process window that is predicted by theory [97]. The maximum shear strength is observed for US levels close to level *D*. It is found that with increasing BF, the value of optimum US parameter *D* decreases. However, for lower BF levels, the window between *B* and *D* is found to be wider than that for high BF levels. Thus, significantly lower levels of BF and US can be used to obtain Cu ball bonds with relatively high SS. This might lead to a reduction in the pad stress during bonding, thereby reducing the chances of damage to the Si chip.

3.2 Al Pad Splash

Figures 3-6 (a) and (b) show the optical and SEM micrographs of typical pads, respectively, after the Cu ball bonds were sheared. Bright coloured Al splash material is visible outside the bond interface and is largest in the US direction. Within the bright splash, a dark ring is observed. Optical profilometry shows that the ring is $\approx 0.5 - 1$ µm higher than the unbonded pad surface, and ≈ 2 µm lower than the maximum splash height that occurs at the edge. These observations and the SEM micrograph in Fig. 3-6 (b) confirm that the ring constitutes part of the splash itself, and is outside the bond interface. The Al extruded can
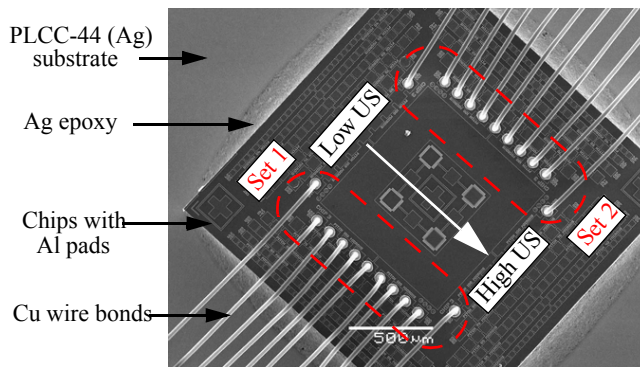
Fig. 3-3. SEM micrograph of the chip used for ball bonding process optimization.

54

follow the shape of the ball (ball bulge) to a certain distance before extruding further out as shown by the illustration in Fig. 3-7. The Al extruded under the ball bulge can have a slope steep enough so the vertical illumination light is reflected out of the microscope resulting in the dark appearance (black ring). The results of energy dispersive spectroscopy (EDS) analysis does not show any significant differences in the amount of Al (85–96%) and Si (4–13%) content in both the bright splash and the dark ring. However, the results of EDS should be interpreted carefully in this situation, because Al and Si are adjacent elements
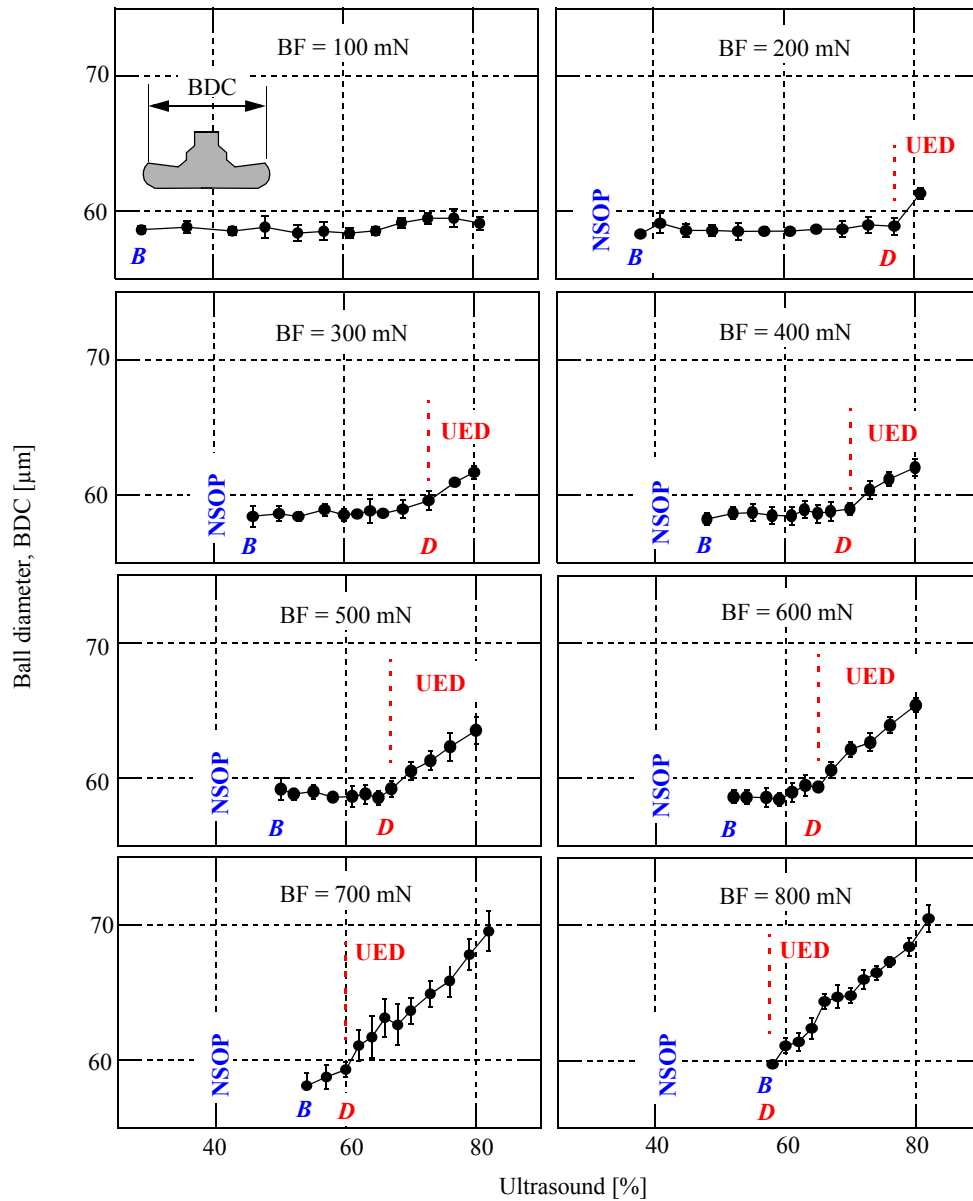
Fig. 3-4. Ball diameter (BDC) for different levels of US and BF. The NSOP and UED regions are shown.

55

having atomic numbers of 13 and 14, respectively. Therefore, the difference in x-ray energies diffracted by Al and Si is small, making it difficult to detect using EDS. An advanced chemical composition study, e.g. wavelength dispersive spectroscopy (WDS) might give more reliable insights into chemical compositions of splash and ring.
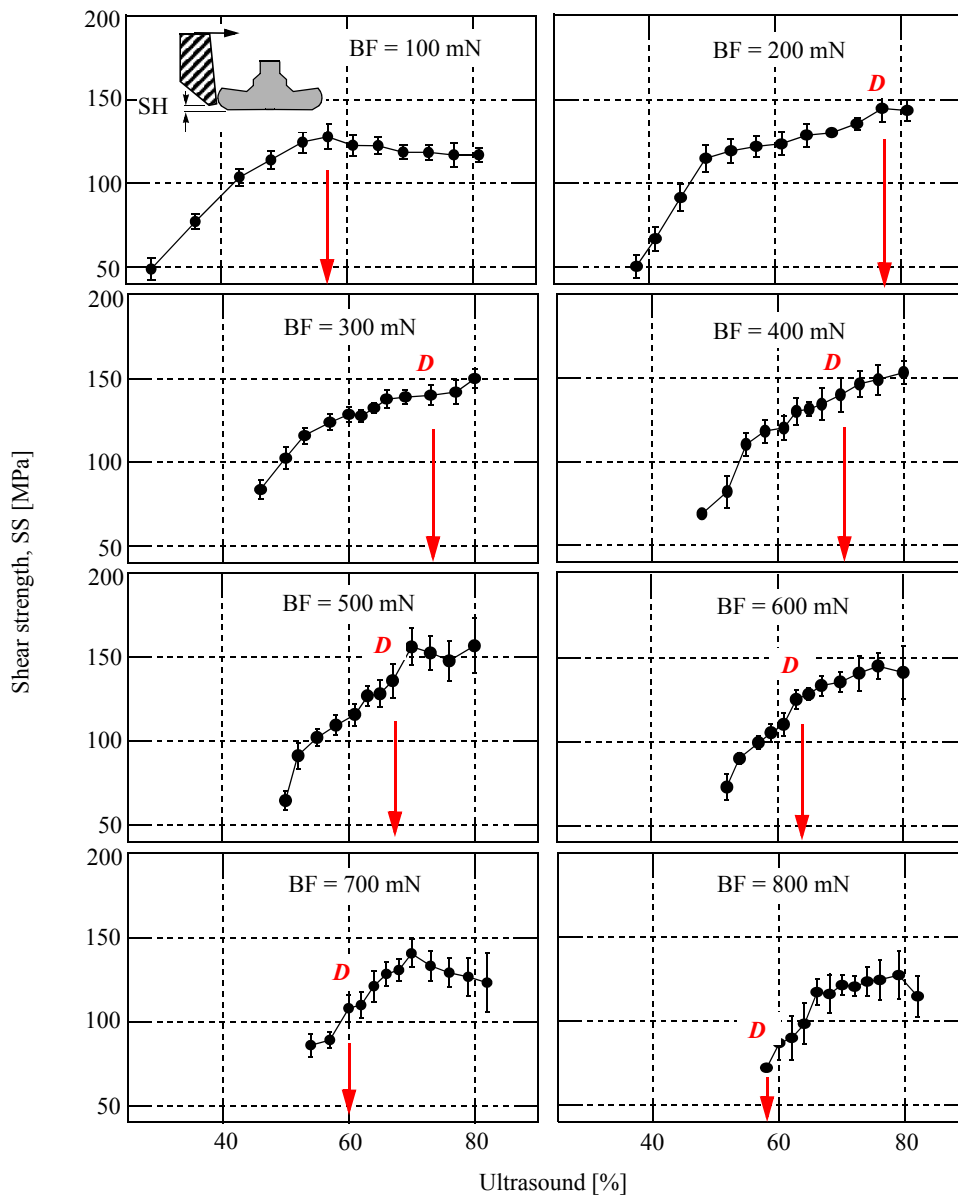
Fig. 3-5. Shear strength for different levels of US and BF. Arrows indicate optimum US level.

3.2.1 Noodle Effect

The ball diameter at interface (BDI) and splash diameter at interface (SDI) are measured in US direction using an optical microscope as shown in Fig. 3-6 (a). The results are shown in Fig. 3-8. It is observed that the BDI decreases with increasing US levels. Higher US levels cause excessive ball deformation at the capillary contact, resulting in higher BDC and lower BDI. An example micrograph showing one of the smallest BDI samples is shown in Fig. 3-9 (a).

(a)   (b)
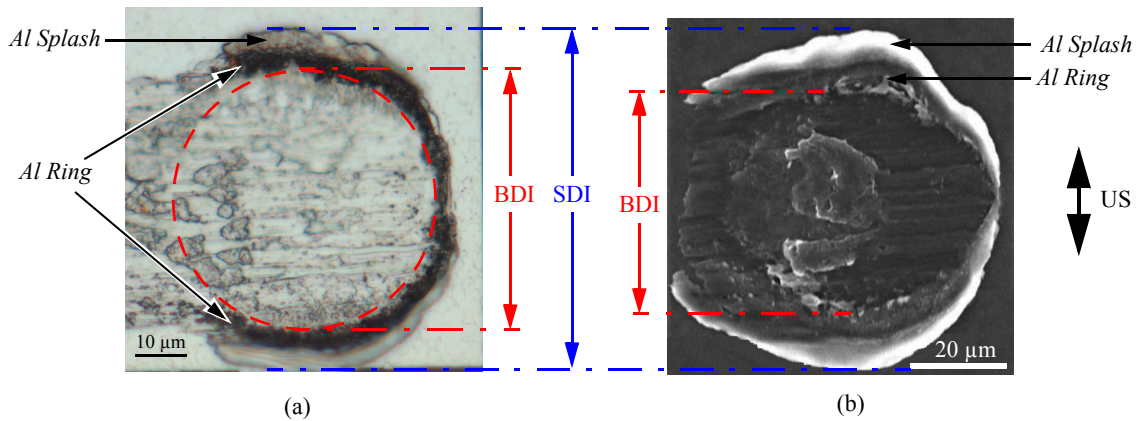
Fig. 3-6. (a) Optical and (b) SEM micrographs of typical sheared Cu ball bonds. Definitions of ball diameter at interface (BDI) and splash diameter at interface (SDI) are shown.
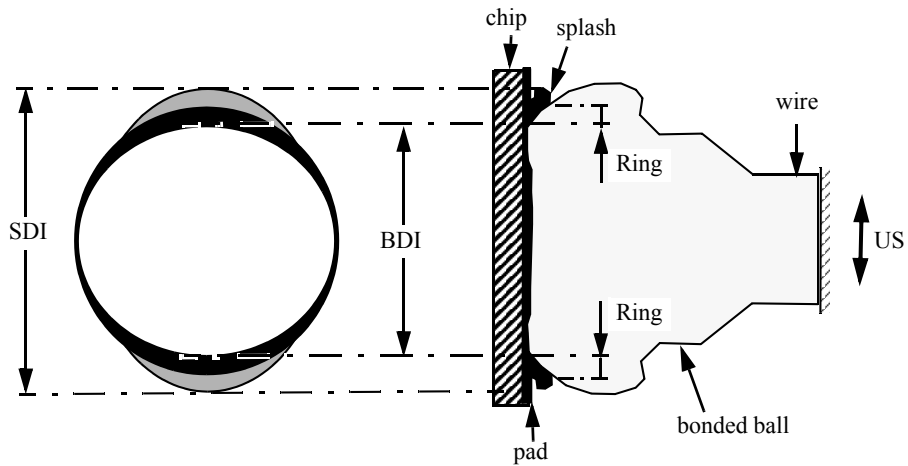
Fig. 3-7. Illustration of concave shaped ball/pad interface [63] due to "noodle effect" in Cu ball bonding. Optically bright and dark areas of splash are shown.

The bonded ball deforms plastically in a similar way as a dough ball between two pressing plates under parallel movements oscillating in opposed directions as illustrated in Fig. 3-10. This analogous process forms the dough into a cylinder (noodle) ready for further processing into e.g. a brezel or a baguette. The cylinder extends perpendicular to the oscillation direction. The higher the oscillation amplitude, the more pronounced the "noodle effect". In a similar way, the BDI decreases with increasing US. The reduction in the BDI is accompanied by a reduction in the circularity of the bonded ball circumference by e.g. more than
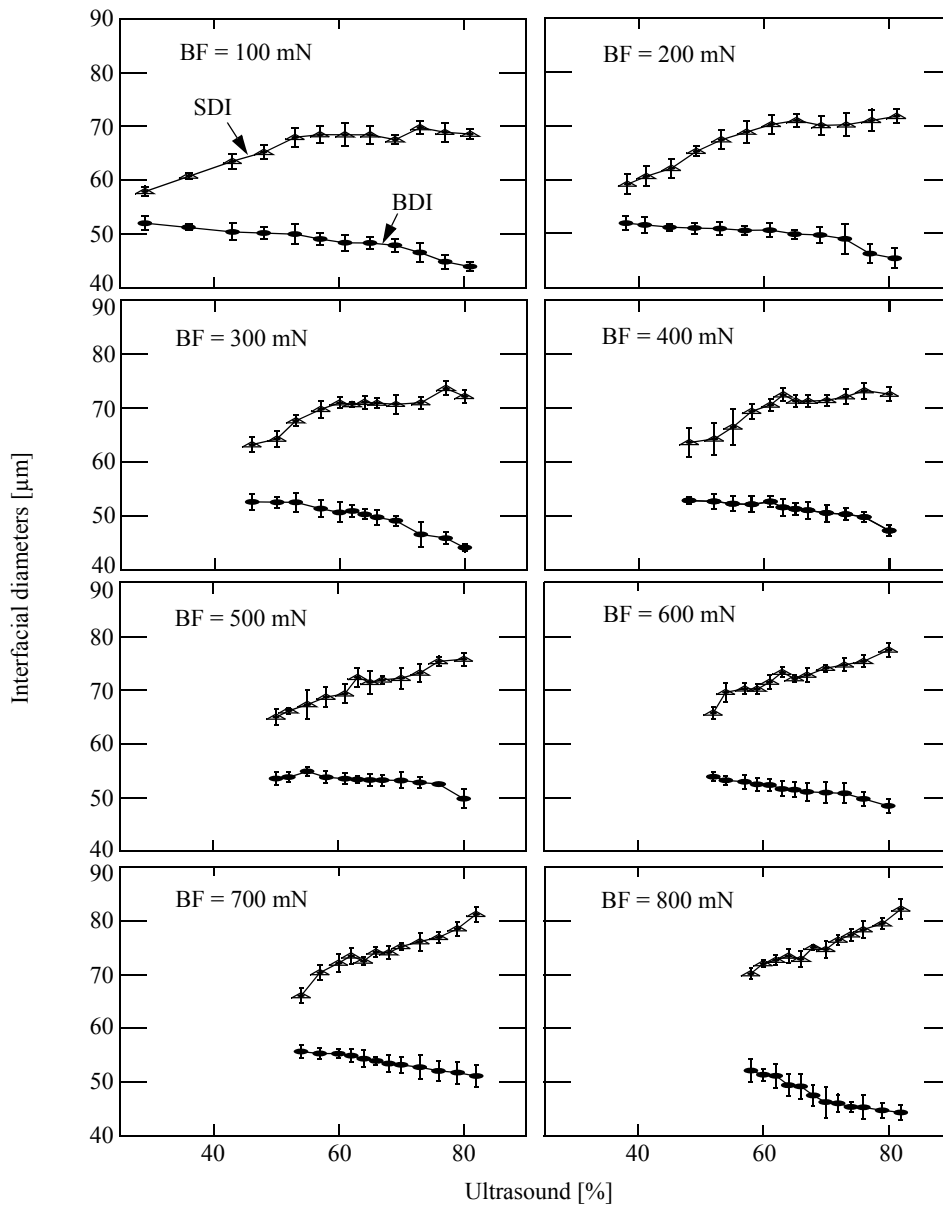
Fig. 3-8. Interfacial diameters: BDI (•)and SDI (ᵔ) for different levels of US and BF.

10% as shown by its elliptical shape in Fig. 3-9 (b). The minor axis of the ellipse is in the US direction and the major axis is perpendicular to the US direction.
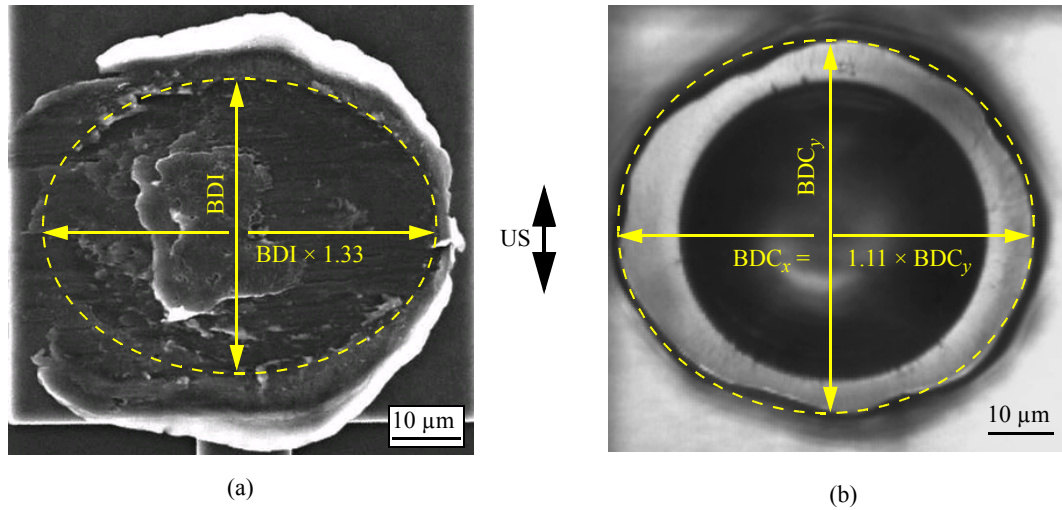
Fig. 3-9. Typical Cu ball bond (US = 77% and BF = 600 mN) with one of the smallest BDI: (a) SEM fractograph after shear; (b) Optical micrograph of the bond before shear showing non-circular BDC. BDC = (BDC$_x$ + BDC$_y$) / 2.
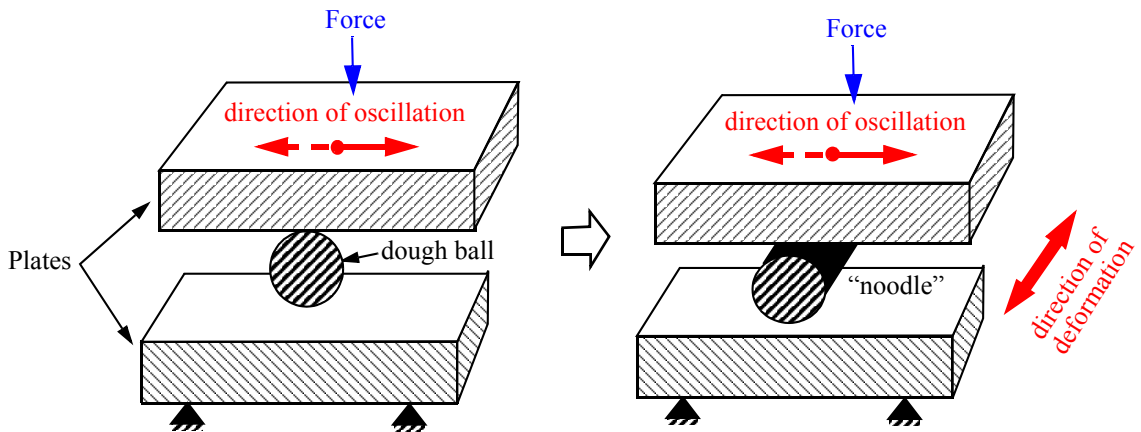
Fig. 3-10. Illustration of "noodle" formation process, which is analogous to the deformation behavior of the Cu bonded balls due to the on-going ultrasound.

3.2.2 Splash Results

The amount of splash can be quantified using SDI. The value of SDI increases with increasing US and can be compared to the volume of pad wear W defined by the sliding wear model [115]

$$W = \frac{k \cdot F_N \cdot A_T}{3H} \qquad (3\text{-}1)$$

where k is the dimensionless wear coefficient, F_N is the normal load (BF in N), A_T is the total sliding distance (in m), and H is the hardness of the softer material (in Pa), in this case the Al bond pad [116–118]. According to Eqn. 3-1, the higher the BF, the larger the value of SDI. On the other hand, high US levels lead to larger sliding amplitudes, longer sliding distances for the same time, and to larger values of SDI. These predictions are consistent with the experimental results observed in Fig. 3-8.

3.3 Pad stress

Ball bonding is performed on the microsensor test pad (Fig. 2-13) at optimum US level and US level needed to obtain shear strengths of ≈ 120 MPa (reduced US level) for different levels of BF. A baseline level of 120 MPa is selected since it is a typical shear strength achieved for a comparable Au ball bonding process in Section 2.1. The values of optimum US and reduced US parameters corresponding to each level of BF are shown in Table 3-2. The setup used for microsensor measurement is shown in Fig. 2-16. The measurements are

Table 3-2. Optimum and reduced US processes

BF [mN]	Optimum		Reduced	
	SS [MPa]	US [%]	SS [MPa]	US [%]
200	144	77		53
300	140	73		55
400	140	70	≈ 120	58
500	136	67		60
600	130	65		62

performed on ten chips for each parameter setting shown in Table 3-2, and the *in situ* US force acting at the pad is measured.

The maximum US force F_{max} is evaluated for optimum and reduced US levels for different levels of BF and plotted in Fig. 3-11. It is observed that for optimum US, a high BF level (BF = 600 mN, US = 65%) leads to ≈ 18% reduction in the value of F_{max} than for low BF (BF = 200 mN, US = 77%). However, the value of SS drops from 145 MPa to 135 MPa for BF increasing from 200 mN to 600 mN. By using a lower value of BF (200 mN) combined with a reduced US level (US = 53%), the value of F_{max} can be reduced by ≈ 30% (relative) while maintaining a SS of 120 MPa.

3.4   Discussion

Figure 3-12 shows process results summarized in the US/BF space. The lines of friction and UED determined for Cu ball bonding process are shaped similar to those found for an Au process [97]. For any combination of US and BF which lies in the region below the line of friction, ball NSOPs are expected. Similarly, any combination of US and BF which lies above the line of deformation results in BDC values greater than 58 μm. Contour curves visualize the results for SS and F_{max}.

There is a trade-off between maximizing SS and controlling ball deformation. While staying below the deformation curve, SS reaches 140 MPa in region *C* shown in Fig. 3-12, and
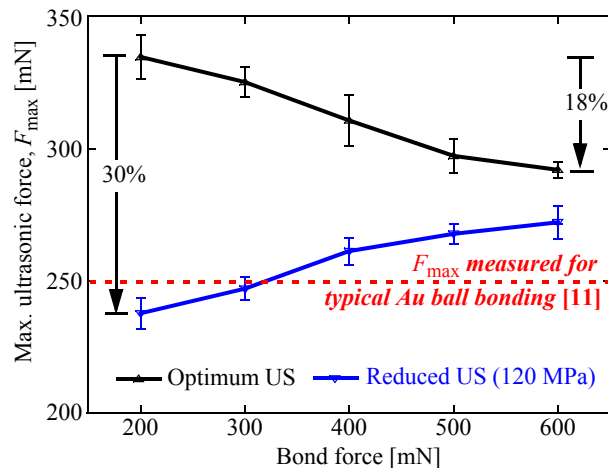
Fig. 3-11. Maximum force acting on the pad (F_{max}) vs. bond force. The error bars indicate average ± standard deviation.

a conventional process window could be chosen within this region. However, this region also results in high values of F_{max}, increasing the chances of pad damage. To minimize the chances of pad damage, Cu ball bonds can be made using parameter combinations lying in the lower stress bonding region R shown in Fig. 3-12. Within the region R, SS $\geq$ 120 MPa and $F_{max} \leq$ 250 mN. These values of SS and F_{max} correspond to those obtained for a typical Au ball bonding process. Thus, by a thorough optimization of BF and US, it is possible to completely eliminate the stress gap between Cu and Au ball bonding.

Figure 3-13 shows the contour plot of SDI in the US/BF space. While the low-stress bonding region (R in Fig. 3-12) results in lower values of SDI, no universal correlation between SDI and F_{max} is observed. A possible reason for this might be that F_{max} quantifies the maximum average stress acting at the bond pad, but not the peak values. The localized peak stresses might be more influential in determining splash and pad failure. A detailed understanding of the effective underpad stress distribution would be helpful in gaining insights into pad failure mechanisms.
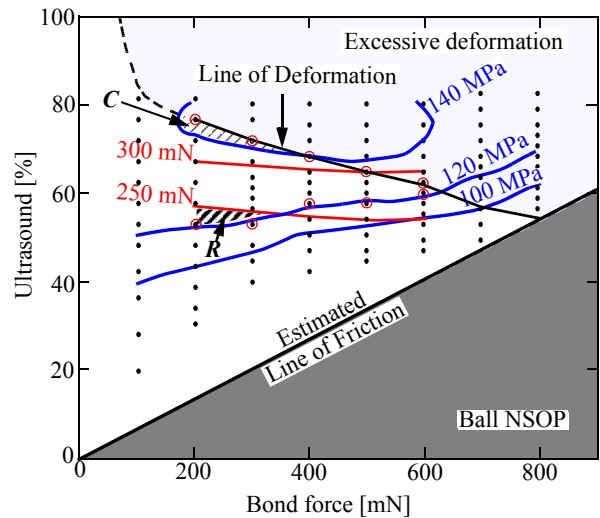
Fig. 3-12. US/BF process space with window for low-stress Cu ball bonding (R). The symbols '·' and '⊙'denote the points for each measured parameter combination and microsensor measurement points, respectively. Blue and red contours are SS and F_{max} contour lines, respectively.

3.5 Summary

Ball bonding processes are optimized on Al pads with a 25.4 µm diameter Cu wire to obtain average shear strengths of more than 100 MPa. Bonding is performed at eight levels of BF: 100, 200, 300, 400, 500, 600, 700, and 800 mN. For each level of BF, the US parameter is optimized. For ball bonds made with conventionally optimized BF and US settings, SS ≈ 140 MPa. The amount of splash extruding out of bond interface is between 10–12 µm. It can be reduced to 3–7 µm if accepting a SS reduction to 50–70 MPa. For excessive US settings, elliptical shaped Cu bonded balls are observed, with the minor axis of the ellipse in the US direction and the major axis perpendicular to the US direction. To quantify the direct effect of BF and US on pad stress, in situ US force is measured. By using a lower value of BF combined with a reduced US level, the pad stress can be reduced by 30% while achieving an average shear strength of at least 120 MPa. These process settings also aid in reducing the amount of splash by 4.3 µm (2.15 µm on each side).

The conventional optimization aims at maximum bond SS for the targeted bond geometry. However, it also causes the highest US stress on the pad. Therefore, a better optimization criterion could be adequately high SS, opposed to maximum shear strength. To this end, contour curves of the maximum ultrasonic force measured by the microsensor are shown in the US/BF process space. The results demonstrate that the underpad damage risks typical to a Cu ball bonding process can be reduced by a thorough optimization of the bonding pro-
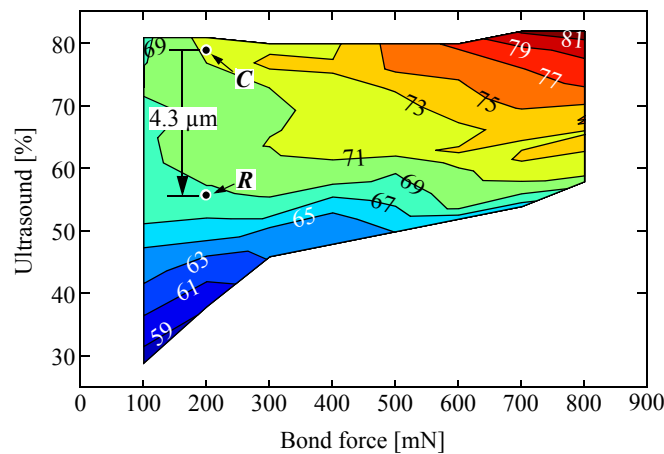
Fig. 3-13. Contour curves of SDI [µm] in US/BF space.

cess settings for US and BF. The amount of Al pad splash can also be reduced to a certain extent, however, it cannot be eliminated completely by controlling the US and BF settings alone.

4   Ultrasonic Al Wedge-Wedge Bonding

This Chapter reports on the in situ US tangential force measured during Al wedge bonding process on Al pads (Al-Al process). Al wedge bonds are investigated for the same or similar mechanisms observed previously during Au-Al and Cu-Al ball bonding processes. In combination with measurements of the current supplied to the US transducer and free-air vibration amplitude of the tool tip, the measured US force is used to derive the US friction power delivered to the interface during Al-Al wedge bonding process.

Section 4.1 describes the experimental details and procedure used in this study, including the microsensor details and calibration. The US force signals measured during a typical Al-Al process is reported in Section. 4.2. Section 4.3 reports on the friction power theory and experimental results pertaining to it. Finally, the results and conclusions of the study are summarized in Section 4.4.

The research reported in this Chapter has been published in the *Journal of Applied Physics* [119].

4.1   Experimental

US wire bonding is performed using a 25 μm diameter AlSi1 wire (1% Si) on Delvotek 6319 wedge-wedge bonder (Delvotek, Ottobrunn, Germany), having a nominal US frequency f = 95 kHz. The tool used for bonding is a tungsten carbide wedge tool ET-25-50-45, manufactured by Erosionstechnik Neudegger (Puchheim, Germany). A microsensor test chip [5] shown in Fig. 4-1 is used in this study. Note that this test chip (explained in Section 4.1.1) is different than the one used for ball bonding in Chapters 2 and 3. The test chip is die bonded to a 20-pin SOIC package using a commercial silver filled epoxy, which then is cured at 150°C for 90 min. The connection pads to the microsensor are connected to the package terminals by Au wire ball bonds. The package terminals are then soldered to a printed circuit board (PCB) as shown in Fig. 4-2. The PCB is mounted on a glass slid using a double sided tape and then fixed on the vacuum chuck of the bonding table.

4.1.1 Microsensor

The microsensor test chip [5] used in this study is manufactured using a standard 0.8 µm double polysilicon CMOS process and is provided by Besi Esec (Cham, Switzerland). The test chip [5] consists of 48 bonding pads with integrated microsensors shown in Fig. 4-2, which are addressed using a multiplexer circuitry co-integrated on the chip. The design and operation of the microsensor and the various electrical components integrated in the test chip are explained in detail in [5] and briefly described below.

Microsensor test pad

Multiplexer bus

Au wire bonds

1 mm
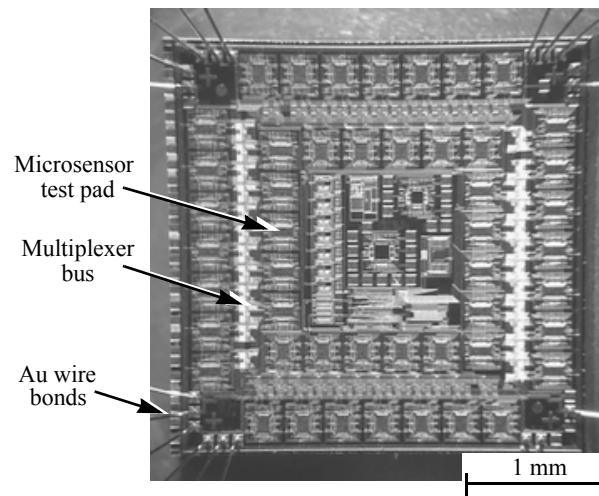
Fig. 4-1. Optical micrograph of test chip with integrated microsensors [5].

20-pin SOIC ceramic package

PCB

Test chip

Au wire bonds

10 mm

connectors to measurement system
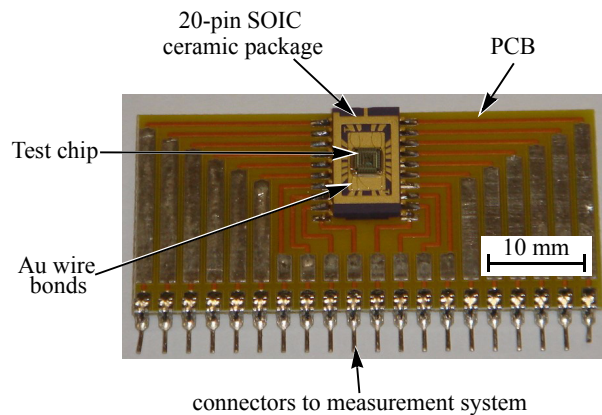
Fig. 4-2. Microsensor test chip in package. Au wire bonds connecting to package terminals.

66

An example test pad with integrated microsensor is shown in Fig. 4-3 (a). In contrast to the octagonal shaped test used for ball bonding, a rectangular test pad, 75×134 µm, is used for the wedge bonding application. The wire and US directions are along the length of the rectangular pad. The microsensor consists of four slanting line n^+ diffused Si piezoresistors integrated next to the bonding test pad as shown by the illustration in Fig. 4-3 (b). This design is selectively sensitive to the force component in the direction of US vibrations [5]. The piezoresistors are connected in a Wheatstone bridge configuration. The Wheatstone bridge is powered by a constant supply voltage, $V_S = 3.75$V. The voltage across the bridge is calculated using $V_B = V_H - V_L$, where V_H is the voltage taken between R_1 and R_3, and V_L is the voltage taken between R_2 and R_4.

The microsensor is calibrated for US tangential force using the procedure described in Section 2.2.3. All conditions and process parameter settings (Table 2-6) for the calibration test are exactly the same as those reported in Section 2.2.3. An example microsensor signal E from a calibration test is shown in Fig. 4-4 (a). Average values of E for each level of US are evaluated in Fig. 4-4 (a). Figure 4-4 (b) shows a linear relationship between the evaluated values from the microsensor and from the standard sensor. The calibration factor of the microsensor is evaluated as the slope of the linear fit in Fig. 4-4 (b) and is determined

(a)

(b)
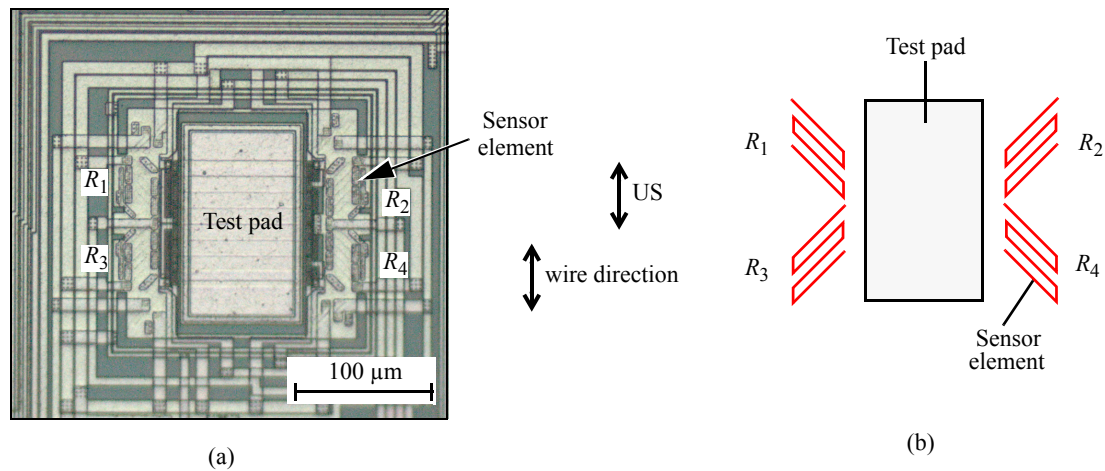
Fig. 4-3. (a) Optical micrograph of microsensor test pad with four slanting line n^+ Si piezo-resistors integrated next to it [5]. (b) Illustration of microsensor element shape and location (not to scale).

to be $f_{calib} = 5.9 \pm 0.33$ mV/V/N. The error value includes the fit error and the sensitivity error of the standard sensor. Thus, the US force measured using the microsensor is

$$F_T(t) = \frac{M(t)}{f_{calib}}$$
(4-1)

4.1.2 Experimental Plan

Al wire wedge bonding is performed on the Al test pad of the microsensor and the *in situ* US force variations during the bonding process is measured simultaneously. The first bond is performed on the microsensor test pad and the second bond is made on the package rim as shown in Fig. 4-5 (a). An example wedge bond on the microsensor test pad is shown in Fig. 4-5 (b). The parameters used for bonding are shown in Table 4-1. Note the different

(a) (b)
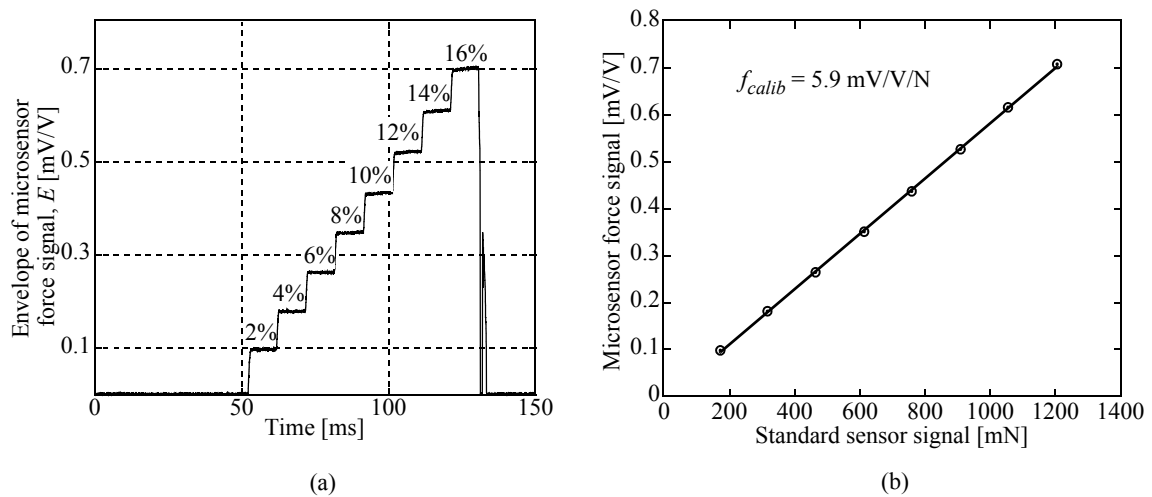
Fig. 4-4. (a) Example microsensor response for calibration test. Numbers in % indicate ultrasound level; (b) Calibration curve with step values from tests.

Table 4-1. Optimized wedge bond parameters

Parameter	Value
Ultrasonic parameter, *USP*	100 units
Bond force, F_N	250 mN
Touchdown force	50 mN
Time	35 ms

ultrasound parameter used compared to that previously described for the ball bonder. The technical ultrasound parameter (USP) of the wedge bonder is dimensionless and ranges from 0 to 200 units. To relate it to a physical quantity, the transient free-air vibration amplitude of the tool tip, $A_o(t)$, is measured using a Laser Interferometer OFV 501 and a Vibrometer Controller OFV 3000 of Polytec GmbH, Waldbronn, Germany. A laser spot 6 μm in diameter is focussed at the center of the tool tip while vibrating freely in air ($F_N = 0$, no wire) for the $USP = 100$ units. A typical plot of $A_o(t)$ is shown in Fig. 4-6, resulting in a maximum vibration amplitude, $A_o^{max} = 0.75$ μm. The result shows that there is ≈ 6.5 ms time lag to reach 95% of A_o^{max}.

4.2 Ultrasonic Tangential Force

An example US force signal is shown in Fig. 4-7 (a). The signal consists of approximately 3,500 cycles of US vibrations. As soon as the US period starts, F_T rises sharply for approximately 2.5 ms when a break-off in the signal is observed. About 1.5 ms after the break-off,
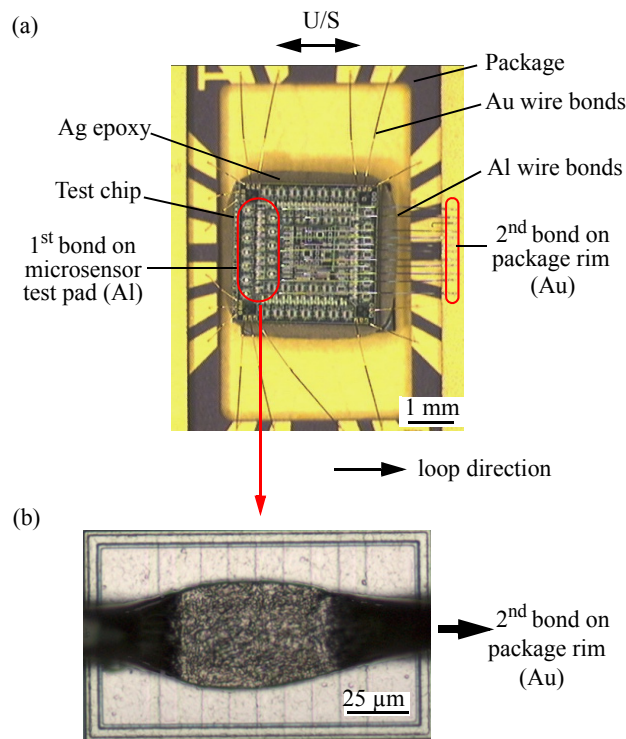
Fig. 4-5. (a) Overview photograph showing Al wire wedge bonds on microsensor chip; (b) close-up of example wedge (1st) bond on microsensor test pad.

69

the signal starts to rise gradually until the end of the US period. The waveforms of the signal at various times are shown in Fig. 4-7 (b). It is found that immediately after the break-off, the signal waveform [3 ms and 6 ms in Fig. 4-7 (b)] deviates from the sinusoidal shape it had initially (at 1 ms). This deviation is observed in only one direction of the US cycle, i.e., when the F_T rises from the negative half cycle to the positive half cycle. The waveform returns to sinusoidal shape about 10 ms after the break-off. In contrast, the break-off
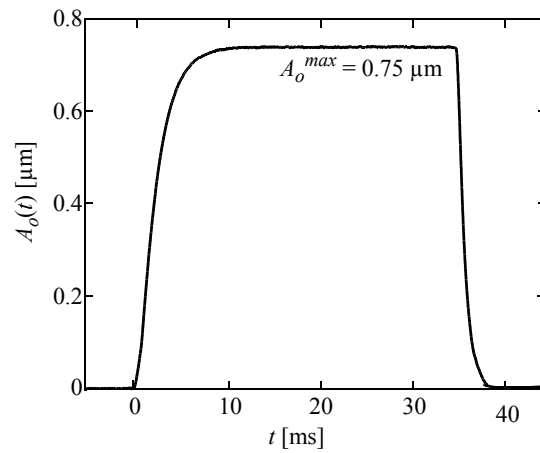
Fig. 4-6. Free vibration amplitude of tool tip $A_o(t)$ for USP = 100 units.
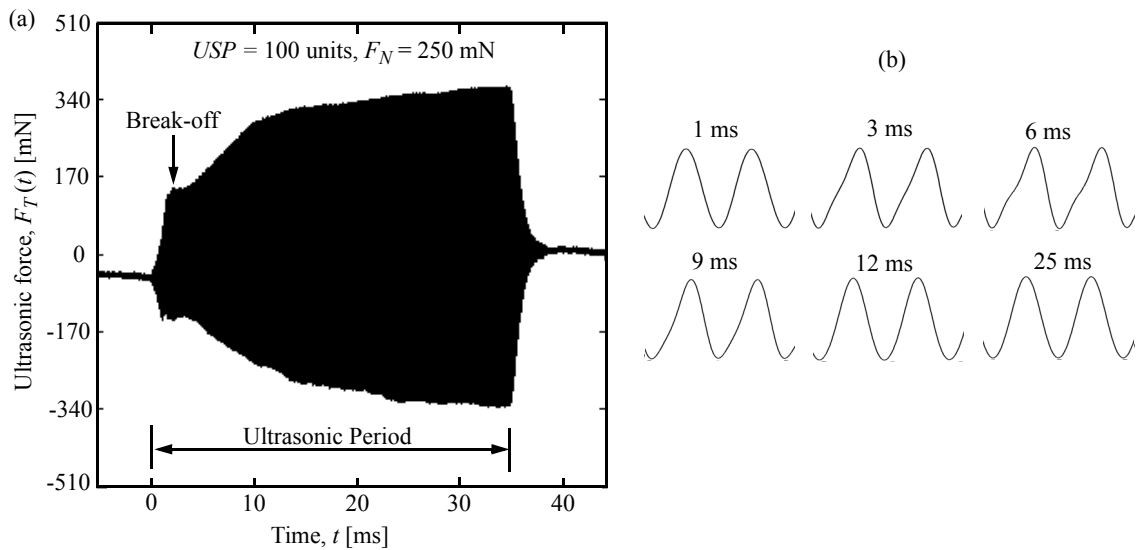
Fig. 4-7. (a) In situ ultrasonic force signal of Al-Al wedge bonding process; (b) Signal waveforms at different times after ultrasound on.

70

reported previously in Au wire ball bonding on Al pads [21] is characterized by a cropped sinusoidal waveform.

The US force signal is filtered at its fundamental, 2nd, and 3rd harmonic frequencies and the resulting amplitudes are plotted in Fig. 4-8. Amplitudes of harmonics higher than the 3rd are negligible and hence not shown. Four phases (1, 2, 3 and 4) can be distinguished for the Al-Al process. During phase 1, the wire sticks to the pad. This is because $A_o(t)$ is not high enough to overcome the static frictional force (F_b) required to cause any sliding at the interface. Phase 2 starts at time t_b when the fundamental (first harmonic) of F_T shows the characteristic break-off. At the same time, the second and third harmonics start to increase sharply from zero. This is caused by the onset of friction at the wire-pad interface. The friction facilitates the relative sliding of the wire on the pad causing bond area cleaning by wear of the native oxide layers at the interface. Moreover, the first harmonic does not rise any further until the end of this phase at t_{b2}, indicating the need of "minimum cleaning" or minimum amount of friction work (wear) to accumulate before the native oxide layers are sufficiently removed from the interface to allow the formation of bonded areas.
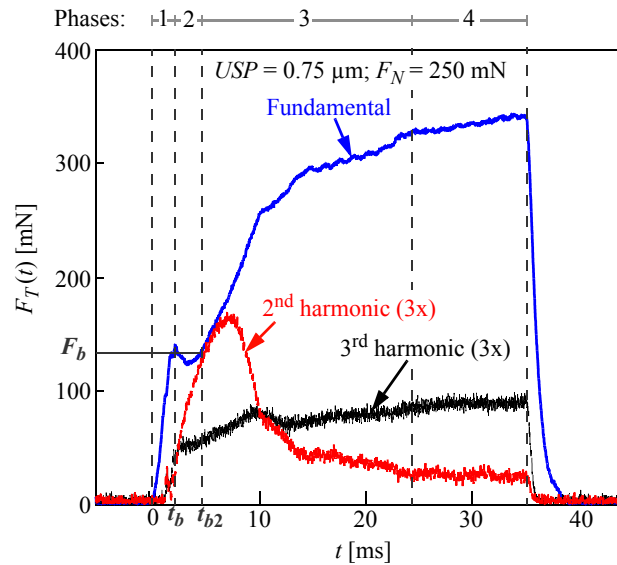
Fig. 4-8. Amplitudes of harmonics of ultrasonic force signal of Al-Al wedge bonding process shown in Fig. 4-7 (a).

The cleaning continues and is accompanied by bonding during phase 3 when the first harmonic of the US force signal starts to rise again. Bonding is expressed by the formation of welded areas at the interface that grow larger where the metals at opposite sides have been sufficiently cleaned. The sum of all bonded areas is the effective bonded area [97, 22], which is growing due to the friction power that continues to clean the interface. During phase 4, the fundamental and harmonics of the US force signal remain relatively constant. It is believed that bonding action has ended at the onset of this phase and US friction power might not aid in any further bonding.

4.2.1 Second Harmonic

In contrast to any ball bonding process, the second harmonic amplitude of the US force signal is found to be predominant during the Al-Al wedge bonding process. This is consistent to the previously reported studies involving measurement of US amplitude during Al-Al wedge bonding process using piezoelectric sensors attached to the horn [84] and to the heater block [85]. This may be attributed to the reduced geometrical symmetry of the wire and the wedge tool [Fig. 4-9 (b)], possibly causing the different vibration shape for positive compared to negative half cycles as observed in the 3, 6, and 9 ms signal waveforms in Fig. 4-7 (b). In particular, the geometry of the tool tip shown in Fig. 4-10 is not symmetrical since the tip radii at the left and right sides are 25 µm and 15 µm, respectively. In contrast, the rotational symmetry of the ball and the capillary geometry illustrated in Fig. 4-9 (a)
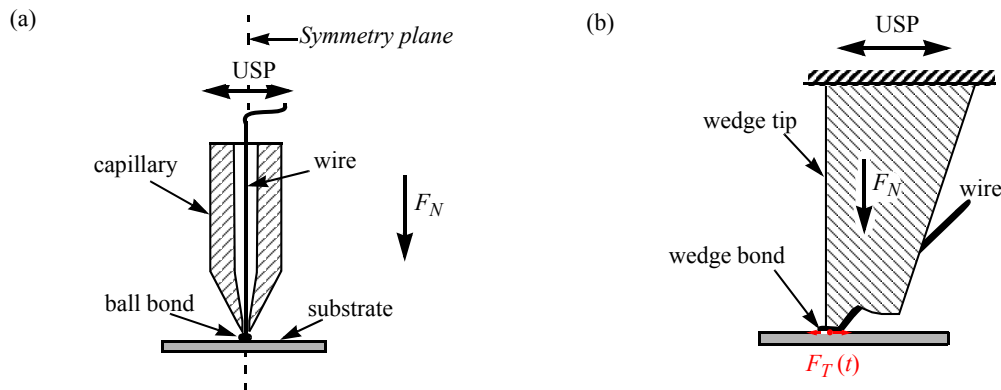
Fig. 4-9. Illustrations of ultrasonic vibrational symmetry of (a) ball bond process (symmetry) and (b) wedge bond process (reduced symmetry).

result in identical US vibrations for both positive and negative half cycles during ball bonding. The asymmetric sinusoidal waveform [3 ms and 6 ms waveforms in Fig. 4-7 (b)] can be mathematically explained as the sum of first, second, and third harmonic amplitudes as shown by an example in Fig. 4-11.

In the next section, a method to derive US friction power is described and typical power values are calculated.

4.3   Ultrasonic Friction Power

The US friction power delivered at the interface during the bonding process can be derived from the measured $F_T(t)$ using [96]
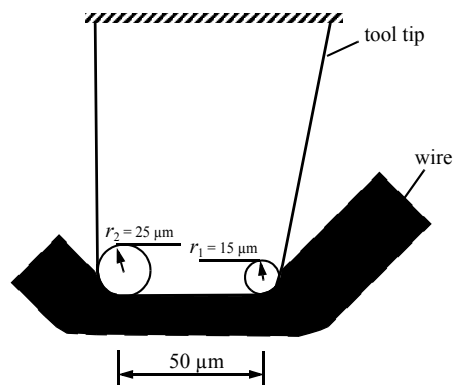
Fig. 4-10. Illustration of wedge tool tip.

1st harmonic

+

2nd harmonic

+

3rd harmonic

=

asymmetric sinusoidal
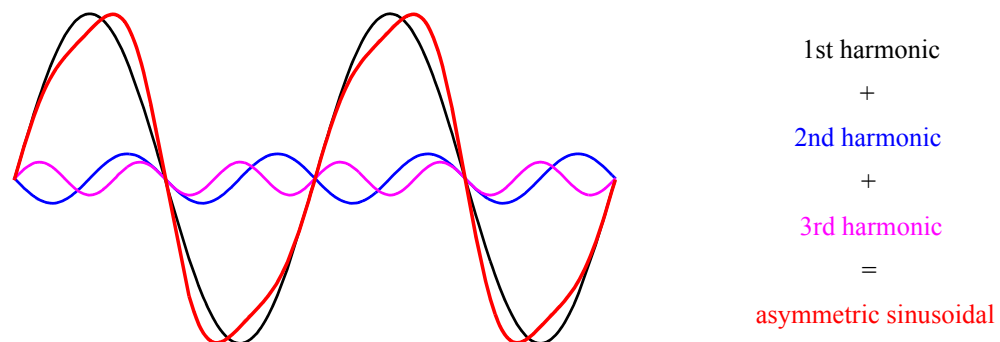
Fig. 4-11. Mathematical construction of the asymmetric waveform from the first, second, and third harmonic amplitudes of an example sine wave.

73

$$P(t) = 4 \cdot f \cdot A_{rel}(t) \cdot F_T(t) \tag{4-2}$$

where f = 95 kHz is the ultrasonic frequency and $A_{rel}(t)$ is the amplitude (zero-to-peak) of relative motion between the wire and the pad. Note that $A_{rel}(t)$ and $P(t)$ do not directly depend on the coefficient of friction in dry sliding. The sliding friction causes cleaning of the interfacial regions, which is followed by the formation of metallurgical connection (bonding) between the two mating surfaces (micro-welds). The micro-welds do not witness any sliding but shear yielding due to the on-going US. The measured $F_T(t)$ includes the combined effect of coefficient of friction (static and dynamic) as well as the shear yielding due to metallurgical bonding, and $F_T(t)$ is the only signal used to determine $A_{rel}(t)$ and $P(t)$.

To derive experimental values for $P(t)$, a number of evaluation steps are necessary, which are outlined in Fig. 4-12. The amplitude of relative motion, $A_{rel}(t)$ is derived using a simplified model describing the interfacial friction during the wire bonding process. The current supplied to the US transducer during the bonding process [measured simultaneously with $F_T(t)$] is used to derive a free-air equivalent of US vibration amplitude during the bonding process, $A_B(t)$. The value of $A_B(t)$ is then used to derive $A_{rel}(t)$. All the formulae associated with this derivation are described in the subsections that follow.
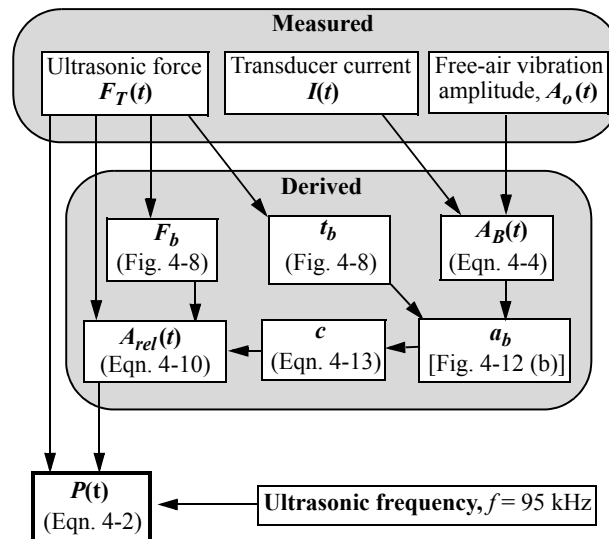
Fig. 4-12. Flow diagram outlining the procedure to derive $P(t)$.

74

4.3.1 Free-air Equivalent of Ultrasonic Vibration Amplitude

The US vibrations are generated by a piezo-electric transducer. During the free-air vibration, the transducer current $I(t)$ is proportional to $A_o(t)$,

$$k_1 \; = \; \frac{I(t)}{A_o(t)} \; = \; \frac{I^{max}}{A_o^{max}} \approx 0.19 \pm 0.01 \;\; \text{A/μm} \tag{4-3}$$

where k_1 is the constant of proportionality and I^{max} is the maximum value of current supplied to the generator in the free-air vibration case (FVC).

However, during the actual bonding process, the normal force F_N presses the wire to the pad. Friction (dynamic or static) dampens the vibration amplitude as seen by less current going to the transducer during the bonding process case (BPC) as compared to the FVC shown in Fig. 4-13 (a). The transducer current measured during BPC is $I_B(t)$ and is used to define the free-air equivalent of the US vibration amplitude during the bonding process,

$$A_B(t) \; = \; \frac{I_B(t)}{k_1} \tag{4-4}$$

An example plot of $A_B(t)$ is shown in Fig. 4-13 (b).
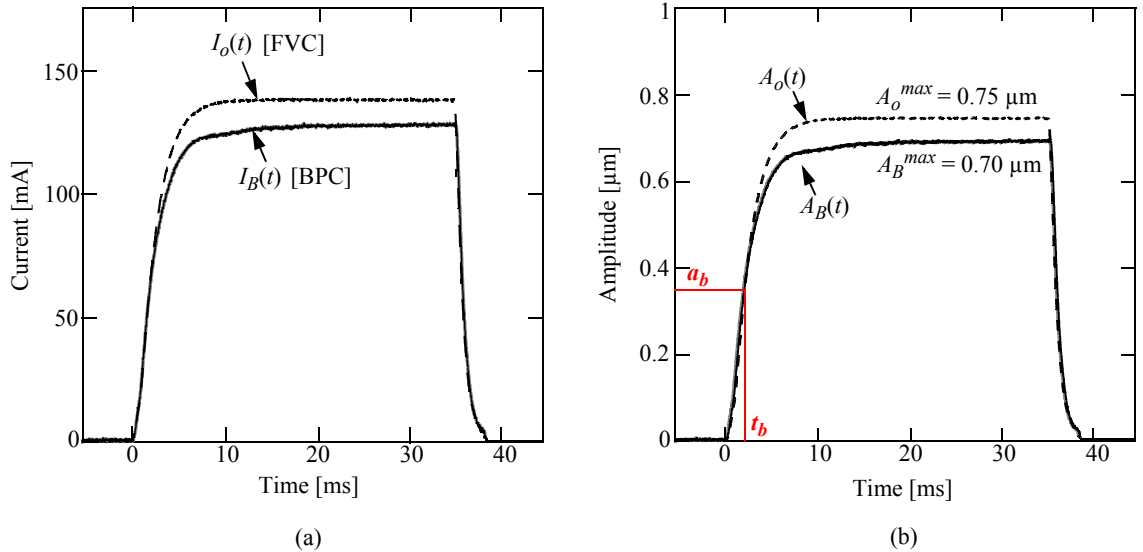
Fig. 4-13. (a) Transducer current and (b) Amplitude during FVC and BPC. $I_o(t)$, $I_B(t)$, $A_o(t)$ are measured characteristics. $A_B(t)$ derived using Eqn. 4-4.

4.3.2 Amplitude of Relative Motion

Interfacial welding in BPC is generated by the US friction. During US friction, $F_T(t)$ is acting at the wire-pad interface. The US causes both the wire and the pad to vibrate at the interface. The vibration amplitudes of the wire bottom and pad top are denoted as $a_w(t)$ and $a_p(t)$, respectively, as illustrated in Fig. 4-14. The relative motion between the wire and the pad is

$$A_{rel}(t) = a_w(t) - a_p(t) \qquad (4\text{-}5)$$

In the case where there is no relative motion between the wire and pad,

$$A_{rel}(t) = 0 \qquad (4\text{-}6)$$

In the case where the wire is vibrating with the tool in free-air (i.e. $F_N = 0$),

$$a_w(t) = A_B(t), \, a_p(t) = 0, \text{ and } F_T(t) = 0 \qquad (4\text{-}7)$$

The amplitudes $a_w(t)$ and $a_p(t)$ can be described as functions of $F_T(t)$ using Eqns. 4-6 and 4-7, and the linear model shown in Fig. 4-15. In this model, it is assumed that the ampli-
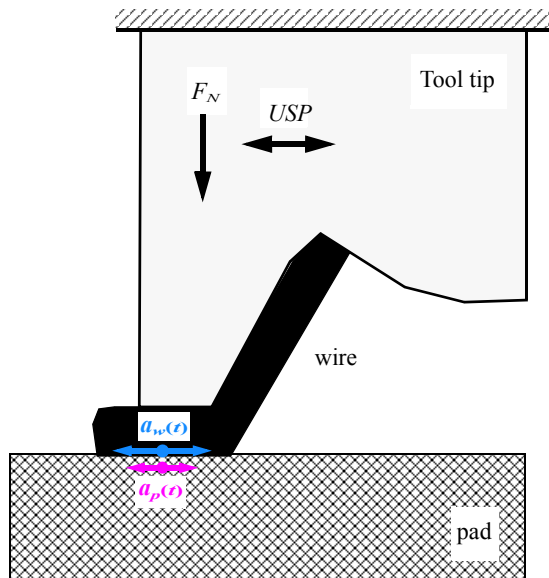
Fig. 4-14. Illustration of the vibration amplitudes at the wire-pad interface during BPC.

tudes $a_w(t)$ and $a_p(t)$ vary linearly with $F_T(t)$. The linearity assumption has been verified by laser measurements of the tool and pad amplitudes and reported in [83]. Thus,

$$a_w(t) = A_B(t) - c_w \cdot F_T(t) \tag{4-8}$$

and

$$a_p(t) = c_p \cdot F_T(t) \tag{4-9}$$

where c_w and c_p are the US compliances (inverse stiffnesses) of the wire/tool and pad/chip, respectively. The value of c_w represents the attenuation of A_B by F_T.

Using Eqns. 4-5, 4-6, 4-8 and 4-9, the amplitude of relative motion is

$$A_{rel}(t) = \begin{cases} 0 & \text{for } 0 < t \le t_b \\ A_B(t) - c \cdot F_T(t) & \text{for } t > t_b \end{cases} \tag{4-10}$$

where $c = c_w + c_p$ is the total US compliance of the bonding system.

The relative motion between the wire and pad starts at the transition point T (Fig. 4-15), marking the transition from 'no sliding' to 'sliding'. Point T corresponds to the break-off point observed in the US force signal [Fig. 4-7 (a)].
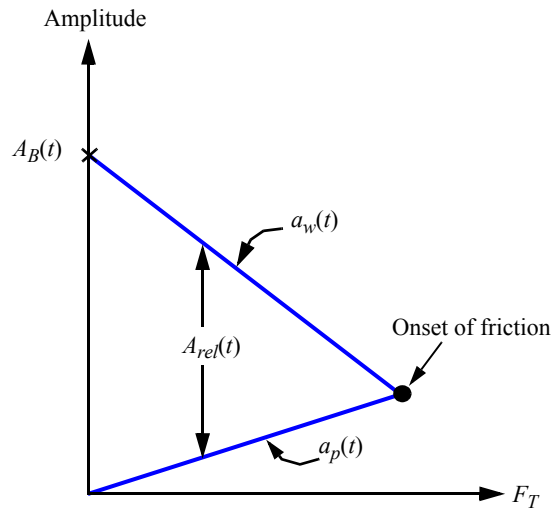
Fig. 4-15. A simplified model of the friction process during the ultrasonic wire bonding process.

It may seem counterintuitive that A_{rel} decreases while F_T increases (Fig. 4-15). However, F_T is not one of the process parameters that can be controlled, e.g. via *USP*. It is affected by F_N, and by the bond growth at the interface. A higher value of F_N will lead a higher value of F_T for friction at the interface, thereby "damping" A_{rel}. Similarly, bond growth at the interface reduces A_{rel}, while F_T may still rise.

The average maximum value for $A_{rel}(t)$ is at least 222 ± 16.4 nm. The total sliding distance, A_T, is

$$A_T = \int_0^t U_{rel}(t) \; dt \tag{4-11}$$

where U_{rel} is the relative sliding velocity averaged over one vibration cycle, given by

$$U_{rel}(t) = 4 \cdot f \cdot A_{rel}(t) \tag{4-12}$$

The average $\pm$ standard deviation of A_T is at least 401.8 ± 65.3 μm.

4.3.3 Ultrasonic Compliance

The US compliance c is a measure of the US free vibration amplitude reduction at the wire/ pad interface per unit tangential force acting at the interface. In the case of no sliding, i.e. at point T, $A_{rel}(t_b) = 0$ and with Eqn. 4-10,

$$c = \frac{A_B(t_b)}{F_T(t_b)} = \frac{a_b}{F_b} \tag{4-13}$$

where a_b is the US amplitude marking the transition between sliding and no sliding. The values $a_b = 0.37 \pm 0.04$ μm and $F_b = 137 \pm 7.30$ N are visually estimated from Fig. 4-13 (b) and Fig. 4-8, respectively. Using Eqn. 4-13, the value of the compliance is $c = 2.66 \pm 0.18$ μm/N.

4.3.4 Results and Discussion

An example plot of $P(t)$ evaluated using Eqn. 4-2, averaged over ten bonds is shown in Fig. 4-16. The friction power $P(t)$ emerges from zero at t_b and increases rapidly until it

reaches a maximum value (P_{max}), about 6 ms after US on. Then it starts to decrease. This decrease is due to bond growth, which reduces the relative motion between the wire and pad. However, the derivation of $P(t)$ using Eqn. 4-2 is not valid after the end of phase 2, since the linearity assumption of $a_w(t)$ and $a_p(t)$ is no longer valid. The $P(t)$ curve derived after the end of phase 2 (indicated using dashed lines) is based on the assumption that value of c remains same as calculated at t_{b1}.

However, beyond time t_{b2}, the bonding action starts, resulting in two physical mechanisms contributing to the non-linearity of the model. First, the cleaning process removes the native oxide layers from the wire and pad, bringing two clean metal layers in contact with each other. This can be interpreted as a transient change in the coefficient of friction at the interface from μ_s to μ_m with $\mu_m > \mu_s$, where μ_s is the coefficient of friction between the two oxide surfaces, and μ_m is the coefficient of friction between the cleaned metal surfaces. The second mechanism is the plastic deformation of the wire during the US period. This leads to a flattening of the wire and therefore to a reduction in the value of c during bonding. Other reasons might be changes in wire material properties such as hardness during bonding [17]. While the changes in the coefficient of friction is already included in the model as the measured $F_T(t)$, the effect due to the reduction in the value of c is not quantified. A reduction in the value of c causes an increase in $A_{rel}(t)$ [Eqn. 4-10], and thus leads to an
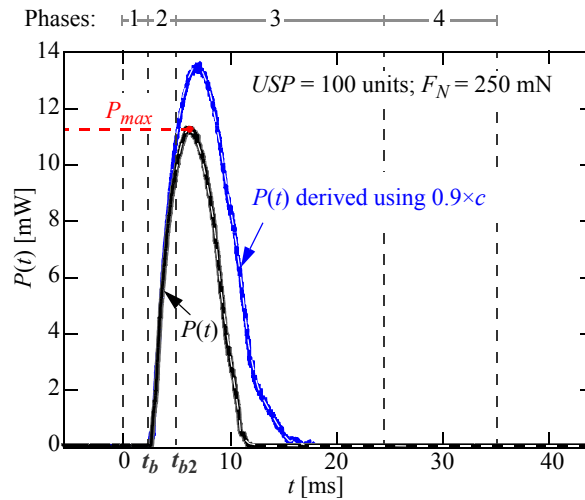
Fig. 4-16. Ultrasonic friction power, $P(t)$. Phases as in Fig. 4-8.

79

increase in $P(t)$ [Eqn. 4-2]. For example, the $P(t)$ curve derived for c reduced by 10% is shown in Fig. 4-16.

It is observed that $P(t)$ becomes zero between $\approx 12 - 16$ ms after the start of US period, which indicates that friction at the wire/pad interface ends at this time. This view is supported by the findings of a previous study of Al wedge bonding processes [120], which used similar process settings as here. In that study, the authors used a high speed video camera to record the wire vibrations during bonding. Combined with the laser measurements of the vibration amplitudes of tool tip and pad edge during bonding, the authors confirmed that relative motion between the wire and pad ends at about 11 ms after the start of US period, a value which is in fair agreement with the present work.

The total power supplied to the US transducer, P_T is calculated using

$$P_T = V_B{}^{max} \cdot I_B{}^{max} = 238 \pm 6 \text{ mW} \tag{4-14}$$

where $V_B{}^{max}$ and $I_B{}^{max}$ are the maximum peak-to-peak values of voltage and current supplied to the ultrasonic generator during BPC, respectively. The maximum friction power is $P_{max} = 11.5 \pm 0.7$ mW, i.e., only about 4.8% of the total electrical power delivered to the US transducer ends up at the bond interface. The remaining power supplied to the transducer is lost due to either internal friction (damping) in the material or heat dissipation caused by friction between the interfaces in the piezo-electric transducer.

The total sliding friction energy delivered to the bond, E, is

$$E = \int_0^t P(t) \; dt \tag{4-15}$$

The value of E during Al wedge-wedge bonding is at least 60.4 ± 9.6 mJ. With an interfacial bond area estimated at 2950 μm^2, the maximum friction power density is at least 3.9 W/mm^2 and the total friction energy density is at least 20.4 J/mm^2. This value is of the same order of magnitude as those reported for typical macroscopic Al-Al US welding processes [121]. The value is about 1.9 times as high as those reported for a Au-SiO$_2$ friction process [92], respectively.

4.4 Summary

A friction power model based on Amontons Laws of friction is used to derive the US friction power during Al wedge bonding. Auxiliary measurements include the current delivered to the US transducer, the vibration amplitude of the bonding tool tip in free-air, and the US tangential force acting on the bonding pad during the bond process.

The US force measurement is like a signature of the bond as it allows for a detailed insight into mechanisms during various phases of the bonding process. A clear break-off in the force signal is observed, which is followed by a relatively constant force for a short duration. A large second harmonic content is observed, describing a non-symmetric deviation of the signal waveform from the sinusoidal shape. This deviation might be due to the reduced geometrical symmetry of the wedge tool.

For bonds made with typical process parameters, several characteristic values used in the friction power model are determined. The US compliance of the bonding system is between 2.66 µm/N. A typical maximum value of the relative interfacial amplitude of US friction is at least 222 nm. The maximum interfacial friction power is at least 11.5 mW, which is only about 4.8% of the total electrical power delivered to the US generator. The total sliding friction energy delivered to the bond is at least 60.4 ± 9.6 mJ.

5 Friction Power and Wear in Thermosonic Ball Bonding

This Chapter reports on a new, improved method to derive the transient interfacial sliding amplitude and US friction power, and on results obtained during thermosonic Au and Cu ball bonding processes. The method employs a bond process modification to accurately derive the mechanical compliance of the US system. Using the derived interfacial sliding amplitude and the sliding wear model [115], the amount of Al pad wear during the Au and Cu ball bonding is estimated.

Section 5.1 summarizes the theory of US friction power highlighting specific differences pertaining to this study. The experimental details including the method of bond process modification are described in Section 5.2. Section 5.3 discusses the measured and derived physical quantities including ultrasonic compliance, relative interfacial amplitude and US friction power. Estimation of the amount of Al pad wear is reported in Section 5.4. Finally, Section 5.6 summarizes the results.

Parts of this Chapter have been submitted as a manuscript for publication [122].

5.1 Theory of Friction Power

While the basic concept of the friction power theory reported in Section 4.3 is unchanged, there are two major improvements in the way A_{rel} and c are derived in this study. These improvements result from using: (i) a constant current control on the US transducer; and (ii) the method of bond process modification, which is explained in detail in Section 5.2.1.

In contrast to a constant voltage transducer used in the wedge bonding study in Chapter 4, this study uses a constant current control for the US transducer, which automatically compensates for damping losses during the BPC, i.e. $I_B = I$. Thus, the hypothetical variable A_B is no longer required; the equivalent free-air vibration amplitude is same as A_o, and is obtained directly by measuring the transducer current I during BPC using

$$A_o(t) = f_d \cdot I(t) \tag{5-1}$$

where $f_d = 18.08$ nm/mA is the calibration constant for derived tool tip displacement depending on transducer current. The value of f_d is derived using laser measurements of A_o for different values of I [123].

Thus, the formula for A_{rel} derived using the friction model reported in Section 4.3.2 is

$$A_{rel}(t) = \begin{cases} A_o(t) - c \cdot F_T(t) & \text{if } c \cdot F_T < A_o \\ 0 & \text{if } c \cdot F_T \geq A_o \end{cases} \tag{5-2}$$

The US compliance c denotes the loss in US amplitude due to the friction force at the interface. It is given by

$$c = \frac{A_o^{nf}}{F_T^{nf}} \tag{5-3}$$

where A_o^{nf} and F_T^{nf} are the US amplitude and tangential force when there is a completely firm connection at the ball/pad interface. Figure 5-1 summarizes the improved procedure to derive the US friction power P. The experimental details and measurements required are described in the following sections.
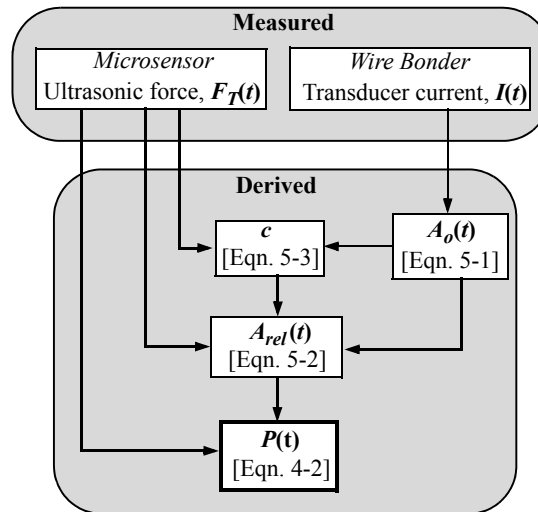
Fig. 5-1. Schematic illustration outlining an improved procedure to derive P.

5.2   Experimental

Thermosonic ball bonding is performed using 25 μm diameter Au and Cu wires on an automatic K&S IConn ball bonder (Kulicke and Soffa Industries Inc., Fort Washington, U.S.A.). This wire bonder uses a dual frequency transducer capable of producing US vibrations at 50 kHz and 122.5 kHz. In this study, $f = 122.5$ kHz is used. The nominal heater plate temperature is 150°C, resulting in an actual temperature of ≈ 138°C at the bond pad. A standard ceramics bottleneck capillary having a hole diameter of 30 μm and chamfer diameter of 35 μm is used. During the formation of free air balls (FABs) with Cu wire, a homogeneous mixture of 95% nitrogen and 5% hydrogen is used as a shielding gas to prevent the oxidation of the hot FAB metal. The flow rate of the shielding gas is set to 0.62 l/min.

The test chip with integrated piezoresistive microsensors described in Section 2.2.1 (Fig. 2-11) is used to measure the US tangential force F_T acting at the bond interface. The test chip is die bonded to a 16-pin SOIC package using a commercial silver filled epoxy, which then is cured at 150°C for 90 min. The connection pads to the microsensor are connected to the package terminals by Au wire bonds. The package terminals are then soldered to a printed circuit board (PCB) as shown in Fig. 5-2. The PCB is placed on a custom made heater plate and clamped by the vacuum system on the bonding machine.
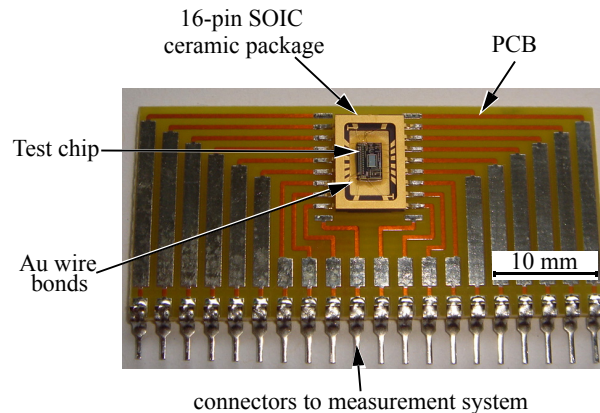
Fig. 5-2. Microsensor test chip in package. Au wire bonds connecting to package terminals.

5.2.1 Bonding Process with Modification

Ball bonding parameters are optimized on a chip with Al metallized bond pads using Au and Cu wires. A 35 μm diameter FAB is used for bonding, which is performed using an ID process for both wire types. The optimized process parameters together with the obtained process responses for both wire types are shown in Table 5-1. The interfacial area is derived using $S = (\pi \cdot BDI^2)/4$, where BDI is the bonded ball diameter at interface (Table 5-1). The estimated values of S for Au and Cu ball bonding are

$$S_{Au} = 960 \pm 13 \, \mu m^2 \tag{5-4}$$

$$S_{Cu} = 906 \pm 39 \, \mu m^2 \tag{5-5}$$

Thus, the average normal stress acting at the interface due to bond force (Table 5-1) is 143.1 ± 1.9 MPa and 176.3 ± 7.8 MPa for the Au and Cu processes, respectively.

To find the compliance values c using Eqn. 5-3, the vibration amplitude and tangential force are evaluated for the case when there is no sliding at the interface. To this end, the bonding process is modified as shown by the illustration in Fig. 5-3 and the US current profiles in Table 5-2. The US period is split into three segments. The duration and US current for each segment is adjusted separately to obtain two low level US steps before actual bonding, i.e., in segments 1 and 2, the value of US current is set to relatively low values of 10% and 20% of the optimum US parameter, I_{opt}, in order to prevent sliding at the ball/pad inter-

Table 5-1. Optimized ball bonding parameters and responses

		Au	Cu
Parameter	Impact force [a.u.]	10	16
	Bond force, *BF* [gf]	14	16.25
	Time [ms]	10	10
	Ultrasonic current, I_{opt} [mA]	90	105
Response	Ball diameter, *BDI* [μm]	35.0 ± 0.2	33.9 ± 0.7
	Ball height, *BH* [μm]	8.6 ± 0.7	11.2 ± 0.7
	Shear strength, *SS* [MPa]	99.8 ± 6.2	102.3 ± 8.1

face. Thus, bond formation takes place only during segment 3 when the US current is ramped up to I_{opt}. All other bonding parameters are maintained at the optimized values shown in Table 5-1.

The previous method to derive c, described in Section 4.3.3, involved an estimation of the values of A_o^{nf} and F_T^{nf}. While the value of F_T^{nf} was taken at the break-off (onset of friction) in F_T, the value of A_o^{nf} was estimated from $A_o(t)$ at the same time stamp as F_T^{nf}. Given the large rising slopes of both $F_T(t)$ and $A_o(t)$, and the fact that there is a small time delay between the two signals, the accuracy of the previous method is substantially limited. Another limitation of the previous study is the fact that an UED process was used. In an UED process, the US causes additional plastic deformation of the wire during the later stages of the bonding process. This leads to a flattening of the wire, resulting in a transient
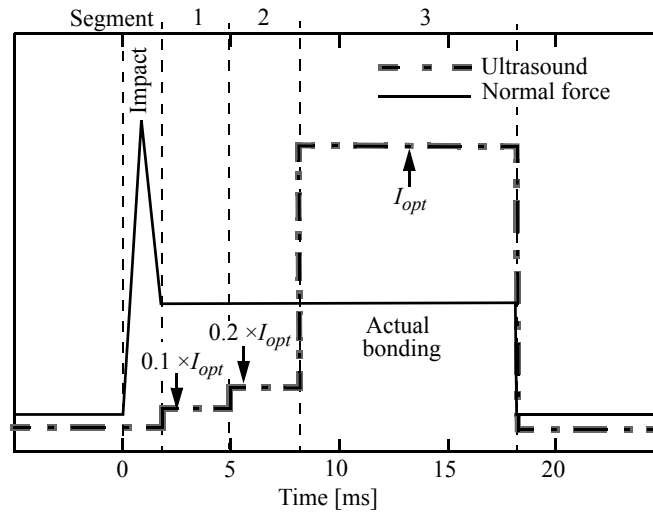
Fig. 5-3. Schematic illustration of force and ultrasound profiles for the ball bonding tests.

Table 5-2. Ultrasonic current profile for ball bonding tests on the microsensor

Wire type	Parameter	Segment number			
		Impact	Bonding		
			1	2	3
	Time [ms]	2	3	3	10
Au	Ultrasonic current [mA]	0	9	18	90
Cu		0	10.5	21	105

reduction in the value of c during the bonding process. As the amount of reduction in c is not known, the US friction power cannot be derived accurately in the later stages of a UED bonding process. The new method described here avoids these limitations by (i) more accurately deriving the values of A_o^{nf} and F_T^{nf} by the bond process modification using the two dedicated US steps; and (ii) using the ID process as described in Section 1.2.2, which ensures that the changes in the value of c due to UED are minimized.

5.3 Results and Discussion

Ball bonding tests are performed with Au and Cu wires on the microsensor test pad and the real time signals of F_T and I are measured simultaneously. The measurements are repeated six times for each wire type using the modified bonding process. Example SEM micrographs of typical Au and Cu ball bonds on the test pad of the microsensor are shown in Figs 5-4 (a) and (b), respectively.

5.3.1 Ultrasonic Signals

The fundamental (first harmonic) and third harmonic amplitudes of F_T measured during typical Au and Cu ball bonding are shown in Figs. 5-5 (a) and (b), respectively. The signal features are similar to those described previously for Au [11, 21] and Cu [62] ball bonding processes (see Section 2.2). The characteristic signal break-off in the first harmonic of F_T

(a)   (b)
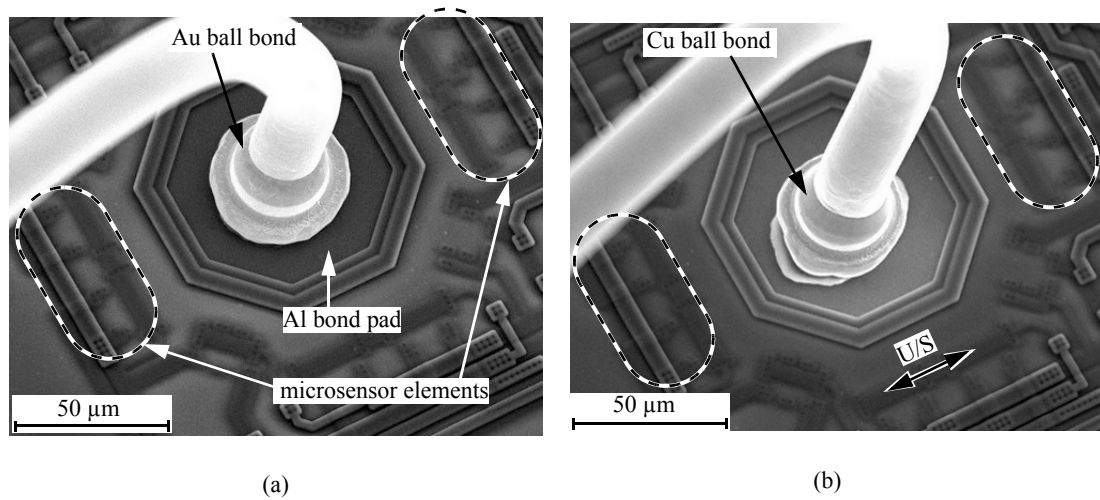
Fig. 5-4. SEM micrographs of (a) Au and (b) Cu ball bonds on the microsensor test pad.

87

is observed in the Au signal, marking the onset of friction at the interface [11, 21]. The onset of friction can also be determined from the time at which the third harmonic starts to rise.

The zero-to-peak amplitudes of I are shown in Figs. 5-5 (a) and (b) for Au and Cu ball bonding, respectively. A small time delay is observed between the I and the F_T signals, with
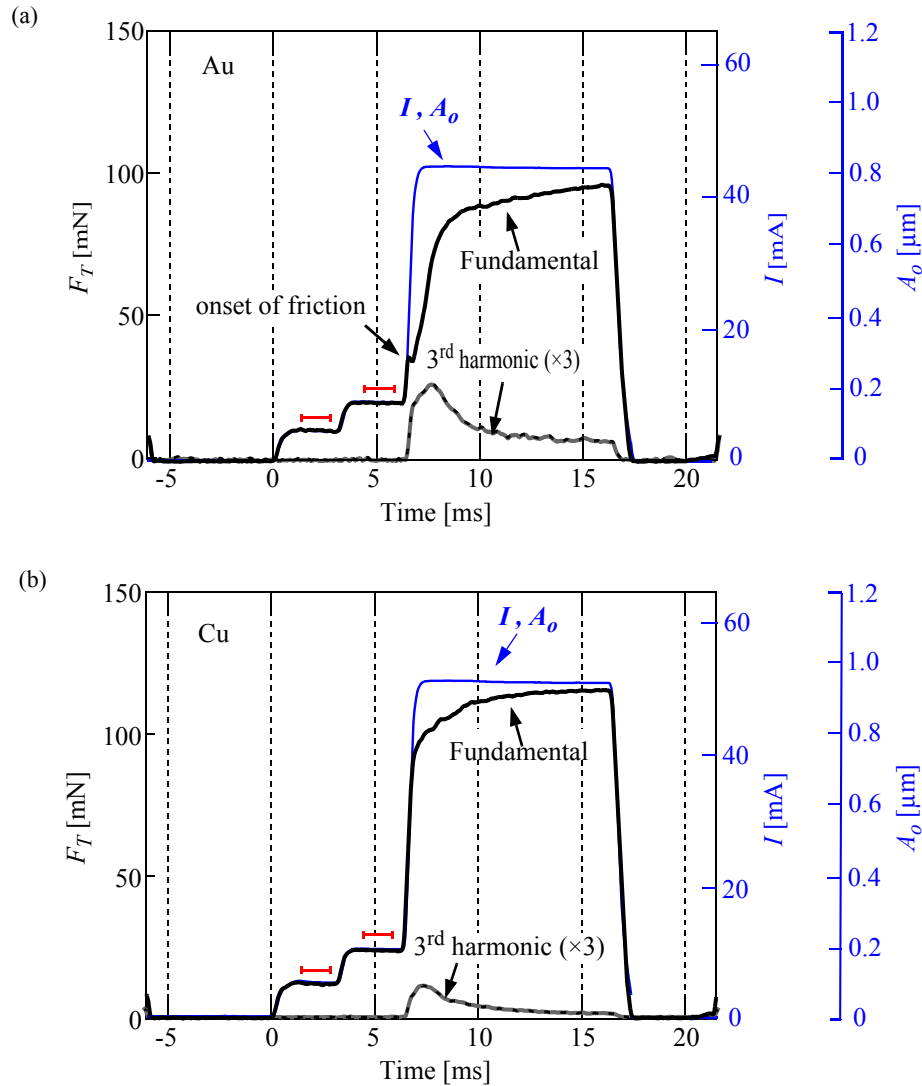
Fig. 5-5. Typical fundamental and third harmonic amplitudes of F_T, and transducer current $I(t)$ for parameter profiles used in (a) Au and (b) Cu ball bonding processes. The scale of the $I(t)$ curve is adjusted so that the height of the two steps in F_T and I overlap with each other. The derived equivalent free capillary tool tip amplitude $A_o(t)$ is also shown on the right scale. The horizontal (red coloured) bars indicate the location at which average values of F_{ti}^{nf} and A_{oi}^{nf} are evaluated.

I lagging behind F_T by $\approx$50 µs. Using Eqn. 5-1, the corresponding values of A_o are derived and shown on a separate scale on the right hand axis in Figs. 5-5 (a) and (b). Typical maximum values of A_o, A_o^{max} = 815 nm and A_o^{max} = 950 nm for the Au and Cu ball processes, respectively.

5.3.2 Ultrasonic Compliance

The values of F_T^{nf} and A_o^{nf} are evaluated from the steps in the plots of F_T and A_o at the periods indicated by horizontal bars in Figs. 5-5 (a) and (b). By substituting these values in Eqn. 5-3, the US compliance c for each segment is derived. The average values of c for Au and Cu processes do not significantly depend on the step number. The overall averages $\pm$ standard deviations are 8.20 $\pm$ 0.18 and 7.66 $\pm$ 0.15 µm/N for the Au and Cu ball bonding processes, respectively. These values are at least three times as large as those reported for Al wedge bonding (described in Section 4.3.3) and Au ball bonding [97] processes. Differences in the designs of US transducer, capillary tool, clamping, and mechatronics control system on this wire bonder might be reasons for the relatively large values of c.

It is observed that the compliance is 6 to 7% higher for the Au than for the Cu ball bonding process. This is due to the fact that Cu has an elastic modulus of 110 – 128 GPa which is 30 – 40% higher than that of Au [111]. Cu therefore offers an increased resistance to US vibrations, resulting in lower compliance.

5.3.3 Relative Sliding Amplitude

The transient curves of A_{rel} derived using Eqn. 5-2 for typical examples of Au and Cu processes are shown in Figs. 5-6 (a) and (b), respectively. The value of A_{rel} rapidly rises to a maximum value A_{rel}^{max} as soon as the US dissipation starts. Then it starts to decrease. This decrease is indicative of bond growth, which reduces the relative motion at the interface. While the decrease is gradual during the Au process, it is more rapid during the Cu process. Moreover, a local maximum in A_{rel} is observed only for the Au process. The local maximum occurs approximately at the same time as the characteristic break-off observed in F_T (onset of sliding) [Fig. 5-5 (a)]. One reason for this might be the mechanical interlock-

ing between the Au ball and Al pad caused by the impact deformation pressing the FAB onto the pad, preceding the US period. The interlocking inhibits relative sliding at the interface for ≈ 0.5 ms as indicated by the local minimum (preceding the local maximum) in A_{rel}. However, it is not clear why this effect would be absent in the Cu ball bond process. An another reason might be attributed to a not yet understood tribological mechanism during Au ball bonding on Al, which results in a situation where a higher value of A_{rel} is temporarily induced at the interface for a lower value of F_T. This contradicts the mechanical interlocking mechanism described earlier. It is not clear what might be the cause for the local maximum in A_{rel}.

The average ± standard deviation of A_{rel}^{max} are 654.4 ± 4.3 nm and 766.5 ± 1.4 nm for the Au and Cu processes, respectively. The standard deviation of A_{rel} in the case of Au process is higher than in the Cu process, which can be attributed to the higher variation in the F_T measured during the Au process compared to the Cu process. The A_{rel} values are 80.6% of the A_o^{max}, indicating that at least 19.4% of applied US amplitude is lost due to friction at the beginning of the bonding process. Due to bond growth, which inhibits relative motion
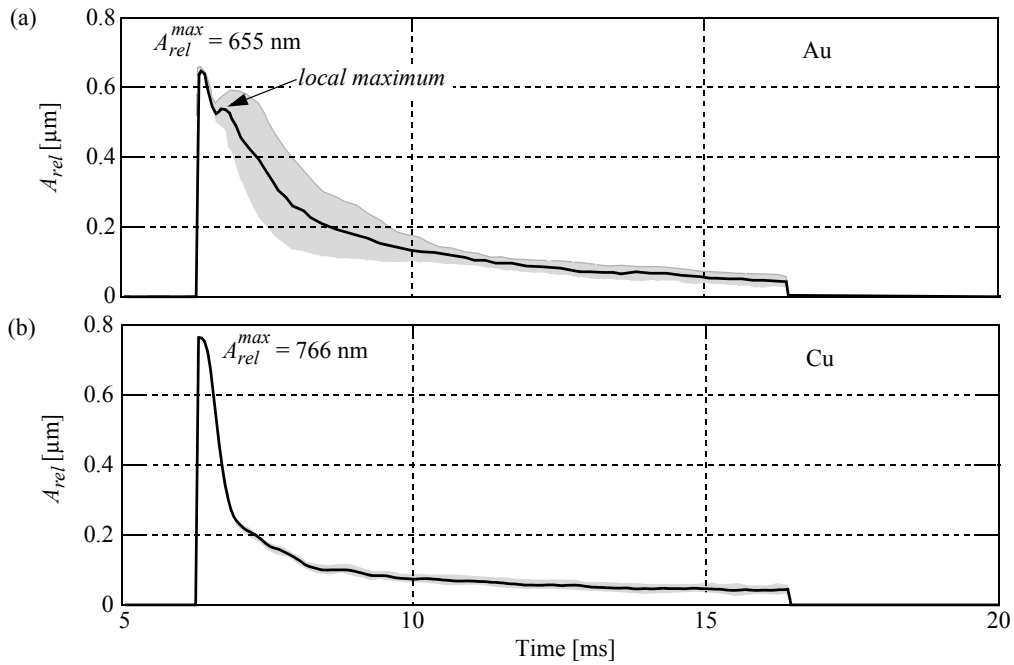
Fig. 5-6. Relative sliding amplitude $A_{rel}(t)$ for (a) Au and (b) Cu ball bonding processes. Dark solid curve is the average, grey shaded area is ± standard deviation. Sample size = 6.

at the interface, the value of A_{rel} decreases to 35 nm at the end of the bonding process, indicating a loss of up to 96.4% in A_o.

The average ± standard deviation of total sliding distance A_T derived using Eqn. 4-11 is 758.6 ± 183.5 µm and 519.4 ± 36.1 µm for Au and Cu ball bonding processes, respectively. Therefore, even though the values of A_o^{max} and A_{rel}^{max} for the Cu process are both $\approx 17\%$ higher than the Au process, the total sliding A_T in the Cu process is found to be $\approx 31\%$ lower than in the Au process. This finding supports the earlier conclusion of reduced sliding (friction) in Cu compared to Au obtained from the analysis of third harmonic of F_T of Au and Cu ball bonding (Section 2.2, Fig. 2-21).

5.3.4 Ultrasonic Friction Power

The US friction power $P(t)$ evaluated using Eqn. 4-2 for Au and Cu ball bonding are shown in Figs. 5-7 (a) and (b), respectively. These curves are not exactly similar to those obtained during the Al wedge bonding process (Section 4.3.4). While the $P(t)$ curve for Al wedge bonding process becomes zero within a few ms after reaching the maximum value (Fig. 4-16), the $P(t)$ curves for Au and Cu ball bonding processes reach a non-zero steady state value. The reason for $P(t)$ going to zero in Al wedge bonding process was related to the end of friction (EOF) [120] at the wire/pad interface as described in Section 4.3.4. It is not completely clear why EOF might be absent in a ball bonding process, i.e. why $P(t)$ does not drop to zero before US ends.

The maximum friction power P_{max} is a characteristic of the friction process at the ball/pad interface. The time stamp of P_{max} might indicate the high-time of cleaning process (removal of native oxides) at the ball/pad interface, which is a pre-requisite to high quality bond formation. The average maximum friction power P_{max} measured during the Cu process is 16.9 ± 0.3 mW, which is $\approx 64\%$ higher than that during the Au process $(10.3 \pm 0.1$ mW). The time required to reach P_{max} is measured from the start of actual bonding (third segment in Fig. 5-3), and is 0.3 ms for the Cu process. This is ≈ 1.2 ms less than in the Au process, consistent with reports on faster bond growth in a Cu process compared to a Au process reported in Section 2.2.6 (Fig. 2-22).

With the measured interfacial areas (Eqns. 5-4 and 5-5), the average maximum friction power densities for Au and Cu ball bonding processes are 10.8 ± 0.2 W/mm^2 and 18.7 ± 0.6 W/mm^2, respectively. These values are in the same order of magnitude as those reported for typical US Al welding processes in the macroscopic range [121].

The averages ±standard deviations of total sliding friction energy delivered to the bond E derived using Eqn. 4-15 for Au and Cu ball bonding are 48.5 ± 8.0 mJ and 49.4 ± 4.0 mJ. These values result in average friction energy densities of 50.3 ± 7.8 J/mm^2 and 54.8 ± 4.8 J/mm^2 for Au and Cu ball bonding, respectively.

5.4 Estimation of Wear

In wire bonding, the US induces a high frequency, low amplitude relative motion at the ball/pad interface. This causes bond area cleaning by interfacial fretting [68]. In this sec-
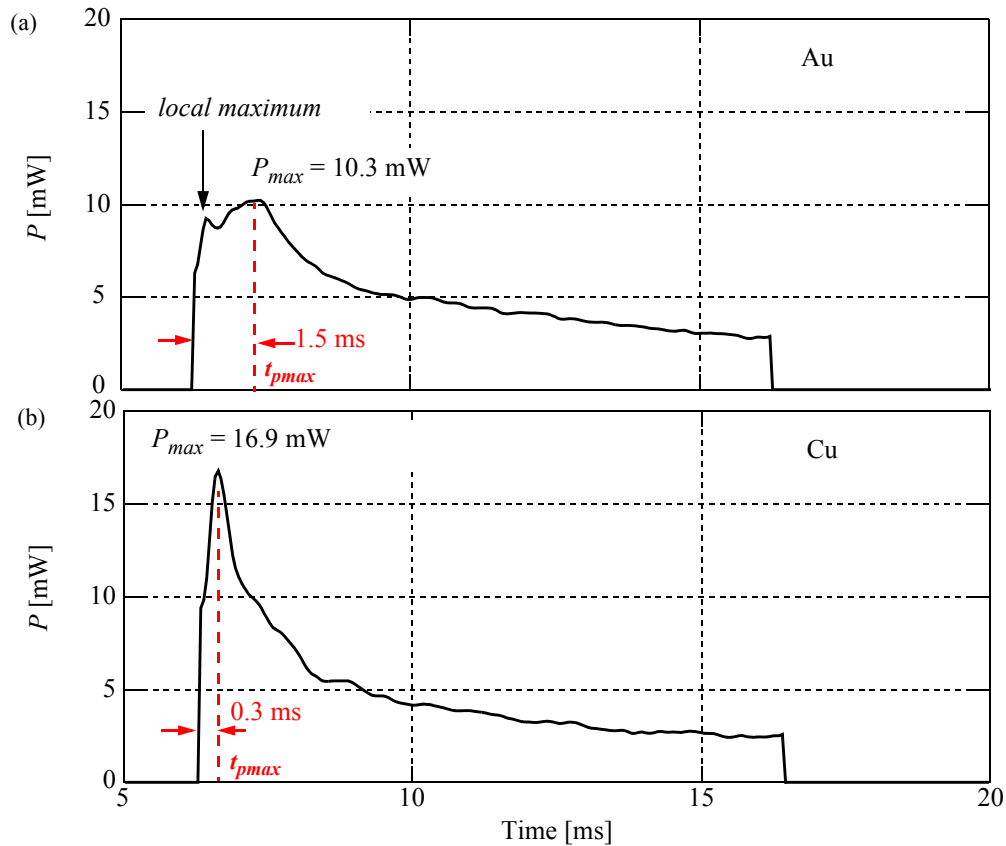
Fig. 5-7. Ultrasonic friction power $P(t)$ for (a) Au and (b) Cu ball bonding processes.

tion, a sliding wear theory [115] is used to estimate the amount of wear during Au and Cu ball bonding.

5.4.1 Sliding Wear Theory

The volume of wear of the softer material (in m^3) defined by the sliding wear theory [115] is

$$W = \frac{k \cdot F_N \cdot A_T}{3 \cdot H} \tag{5-6}$$

where k is the dimensionless wear coefficient, F_N is the normal load, i.e. BF (in N), A_T is the total sliding distance (in m), and H is the hardness of the softer material (in N/mm^2).

A comparison of hardness of FAB and bonded ball (BB) made with Au and Cu wires, and that of the Al bond pad from the literature is shown in Table 5-3. Since the hardness of Au BB and Al bond pad are quite similar, the value of W derived using Eqn. 5-6 for Au ball bonding on Al pads might denote the combined wear of both Au and Al. In contrast, the hardness of Cu is at least 25% higher than that of Al bond pads. Thus, according to Eqn. 5-6, in the case of Cu ball bonding on Al pads, the value of W indicates the amount of Al pad wear.

It has been shown that the volume of wear W produced during fretting satisfies the sliding wear Eqn. 5-6 [124, 125]. The volume of wear caused by US friction per vibration cycle is

$$W_{cycle} = \frac{k \cdot F_N \cdot 4A_{rel}}{3 \cdot H} \tag{5-7}$$

A number of assumptions and simplifications are made when using Eqn. 5-7:

Table 5-3. Comparison of indentation hardness values of FABs, BBs and bond pad.

Material	Wire	FAB hardness	BB hardness	Reference
Au	60 MPa	60 MPa	60–85 MPa	[60]
Cu	88–110 MPa	85 MPa	100–128 MPa	[43, 60]
Al bond pad	55-83 MPa			[116]

1. The mechanical properties of the two contacting metals are uniform throughout the interface.

2. The effect of temperature rise (due to frictional heating) on the material properties, in particular the hardness is assumed to be negligible.

3. The effect of surface fatigue (fretting fatigue) [126, 127] is not included in Eqn. 5-7.

5.4.2 Wear Coefficient, k

The wear coefficient k represents the probability that a surface asperity is worn away when two materials slide against each other. The value of k can be considered as an indication of the severity of the interaction between the two sliding surfaces. Experimental results for a number of different metal [124, 128] combinations, including those of interest in this study i.e. Au, Cu and Al have shown that the value of k is proportional to the fifth power of the coefficient of friction μ according to

$$\log\left(\frac{k}{3}\right) = 5\log\mu - 2.27 \quad \Rightarrow \quad k = 16.1 \times 10^{-3} \times \mu^5 \tag{5-8}$$

The value of μ is not constant during the bonding process. At the start of the bonding process, thin layers of native oxides are present on the surfaces of the bonding metals (Al and Cu, but no oxide in case of Au), which is subsequently removed due to US friction. Where the bonding metals are free from their surface precipitations or oxides, the value of μ is higher than that at uncleaned areas, i.e. $\mu_m > \mu_o$, where μ_o and μ_m are the coefficient of oxide friction and coefficient of metal friction, respectively. The cleaning action is accompanied with bonding (welding) producing interfacial regions with metallurgical connection that do not experience sliding friction but shear yielding due to the on-going US. Using Amontons law of friction, an overall coefficient of friction is suggested that includes sliding on oxide and clean metal as well as the shear yielding of metallurgically welded regions:

$$\mu_{OA}(t) = \frac{F_T(t)}{F_N} \tag{5-9}$$

Using Eqn. 5-8 and μ_{OA} from Eqn. 5-9 as μ, the wear coefficient, k, is

$$k(t) = 16.1 \times 10^{-3} \times \left[\frac{F_T(t)}{F_N}\right]^5 \tag{5-10}$$

Typical curves of $k(t)$ derived using Eqn. 5-10 for Au and Cu ball bonding are shown in Figs. 5-8 (a) and (b), respectively. In the derivation of k, only the sliding portion of F_T is considered. For simplicity, the sliding portion of F_T is determined for the period when the third harmonic of F_T is greater than 20% of its maximum value. The value of k increases gradually with time due to cleaning at the interface and reaches a maximum value k_{max} at the end of the US period. At the start of the US period, there are native oxide and surface precipitate layers at the bond interface. These contaminants act as lubricants between the metal layers, resulting in a lower value of k at the start of bonding [129]. With increasing time, the cleaning at the interface causes clean metal layers exposed to each other leading to an increase in the value of k. The average $\pm$ standard deviation of k_{max} for Au-Al and Cu-Al bonding processes are 2.2 ± 0.3 and $3.7 \pm 0.4 \times 10^{-3}$, respectively. These values are within the range of k values reported for these material combinations under fretting wear conditions [129].
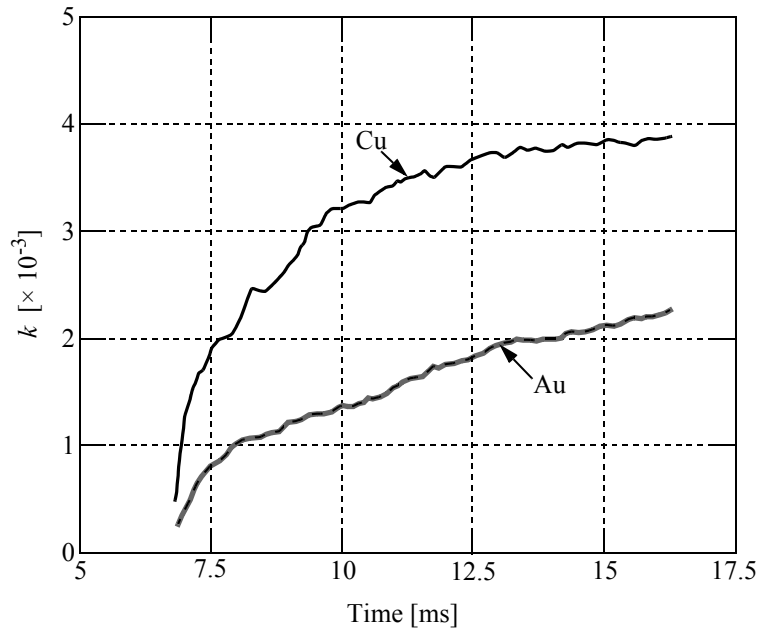
Fig. 5-8. Wear coefficient $k(t)$ derived using Eqn. 5-10 for Au and Cu ball bonding.

5.5 Amount of Wear

Substituting Eqn. 5-10 in Eqn. 5-7, the volume of wear per US cycle is

$$W_{cycle} = \frac{21.5 \times 10^{-3} \cdot [F_T(t)]^5 \cdot A_{rel}(t)}{H \cdot [F_N]^4} \qquad (5\text{-}11)$$

The Al bond pad hardness H is taken from [116] where 70 MPa is the median value of the range of H values measured for typical IC bond pads [116]. Figures 5-9 shows typical plots of W_{cycle} for Au and Cu ball bonding, respectively. In the case of Au ball bonding, W_{cycle} rises gradually until it reaches a maximum value of 0.44 μm^3 at $\approx$ 3 ms after the start of US. In contrast, in Cu ball bonding, W_{cycle} rises rapidly to reach a maximum value 0.93 μm^3 at $\approx$ 1.2 ms after the start of US.

The average total volume of wear due to US friction during bonding is
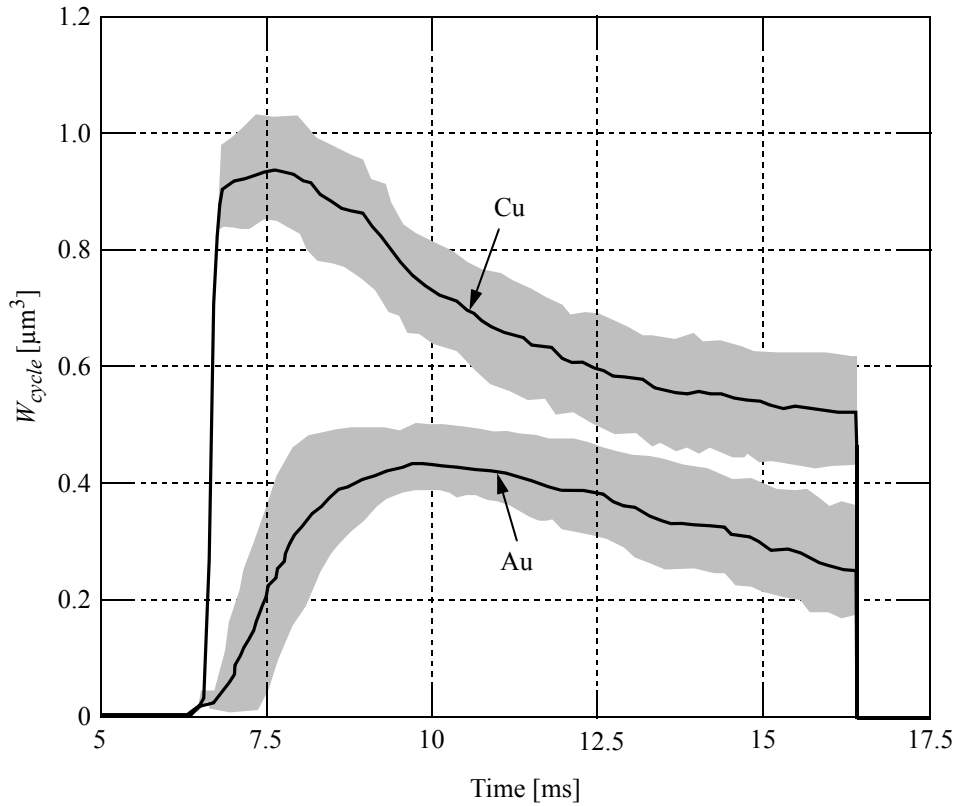
Fig. 5-9. Wear volume per ultrasound cycle W_{cycle} during Au and Cu ball bonding for H = 70 MPa. Dark solid curve is the average, grey shaded area is $\pm$ standard deviation. Sample size = 6.

96

$$W = \sum_{cycles} W_{cycle} \tag{5-12}$$

The average $\pm$ standard deviation of W is 400.5 ± 67.2 μm^3 and 808.4 ± 103.3 μm^3 for Au and Cu ball bonding, respectively. The time evolution of W, $W(t)$, is shown in Fig. 5-10 for Au and Cu bonds, respectively.

The average total depth of wear, δ, is

$$\delta = \frac{W}{S} \tag{5-13}$$

where S is the interfacial area. With the measured interfacial areas (Eqns. 5-4 and 5-5), the average $\pm$ standard deviation of the total depth of wear δ is 416.3 ± 69.9 nm and 895.7 ± 114.4 nm for the Au and Cu processes, respectively. The standard deviation of δ indicates measurement variability (due to F_T, A_{rel}, and S). It does not include the error due to the variation in k and H. The combined error of δ that includes each of these factors is
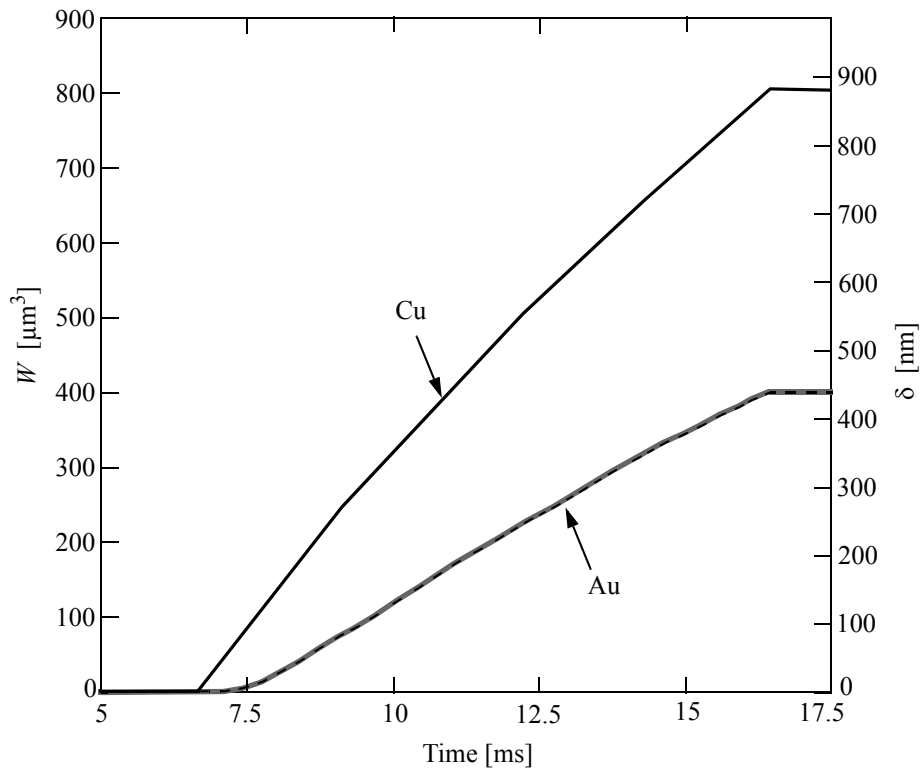
Fig. 5-10. Time evolution of W and δ during Au and Cu ball bonding.

estimated in the next section. The thickness of native Al oxide on typical IC bond pads ranges between ≈ 2.5–15 nm [130–133]. Using the derived $W(t)$, it is estimated that these native oxides are dispersed at ≈ 1.4 ms and ≈ 0.5 ms for the Au and Cu ball bonding, respectively.

The worn material might be either trapped within the bond interface or transferred outside of the bond zone. While the former might be the main mechanism in the case of Au-Al bonding process, the latter as Al pad splash (Section 3.2) is observed to be more dominant in the Cu-Al process. Since the hardness of Au and Al is similar, the derived amount of wear in the Au-Al process might indicate the combined wear of both Au and Al. Moreover, Au is a nobel metal that shows exceptional adhesive and cohesive properties [131, 132]. Thus, if a Au or Al wear particle is formed, it might adhere back to the bulk material, resulting in reduced transfer of the wear debris to the outside of the bond interface. Further investigations are required to gain a better understanding of the mechanism of wear and particle transfer in Au-Al process.

To verify the theoretical values of δ with experimental data, the profile of surface after shearing away the Cu ball bonds is measured using an optical profiler. This experimental method could not be applied in the case of Au ball bonds since in the case of Au, shear failure occurred in the Au ball, leaving Au residue on the pad as shown in Fig. 5-11. An optical fractograph of a typical sheared Cu ball bond together with its surface profile are shown in
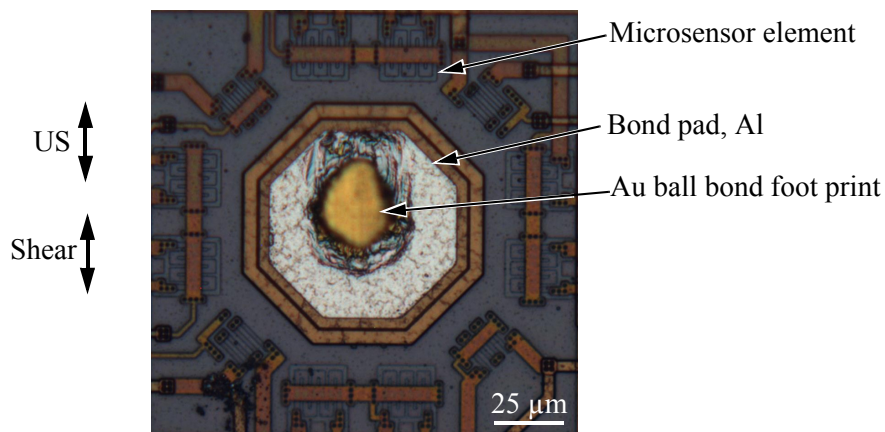
Fig. 5-11. Optical fractograph of a typical sheared Au ball bond footprint on the microsensor test pad.

Fig. 5-12 (a) and (b), respectively. Figures 5-13 (a) and (b) show the surface profile along the lines X and Y shown in Fig. 5-12 (b), respectively. From the surface profile, the experimental wear depth is estimated as the difference between levels of pad surface and the average maximum depth at the sheared bond footprint as shown in Figs. 5-13 (a) and (b). It is observed that the experimental estimates of δ for Cu ball bonds range between 500–750 nm. Note that these values might possibly include a small amount of material removed during shearing the bonded ball. These experimental values agree reasonably well with the theoretical estimates of δ when the combined error of δ due to the variation in k and H (described in the next section) is considered.
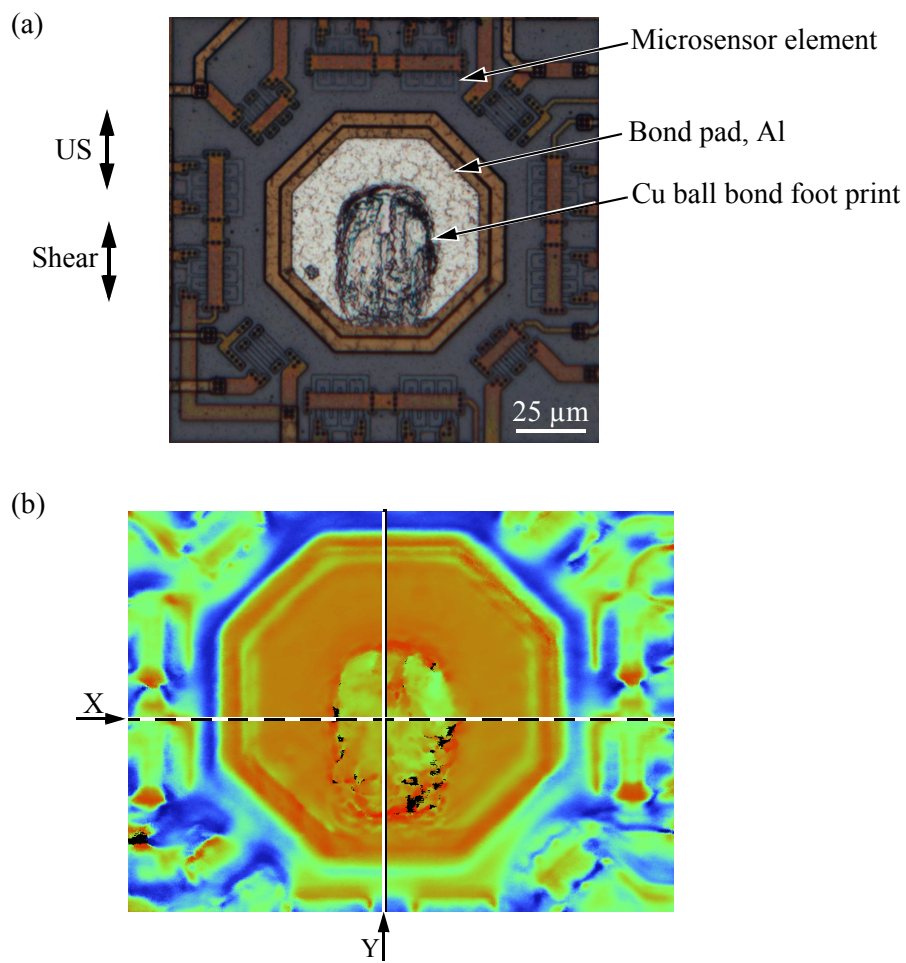
Fig. 5-12. (a) Optical fractograph of a typical sheared Cu ball bond footprint on the microsensor test pad. (b) Surface profile of the sheared Cu ball bond fractograph shown in (a).

5.5.1 Sensitivity Analysis

The error due to the values of k and H can be estimated. The sensitivity of δ to these errors is evaluated and given in Table 5-4. The combined error $\Delta\delta_T$ is derived using the theory of combination of component errors in overall system accuracy calculations [134] and is
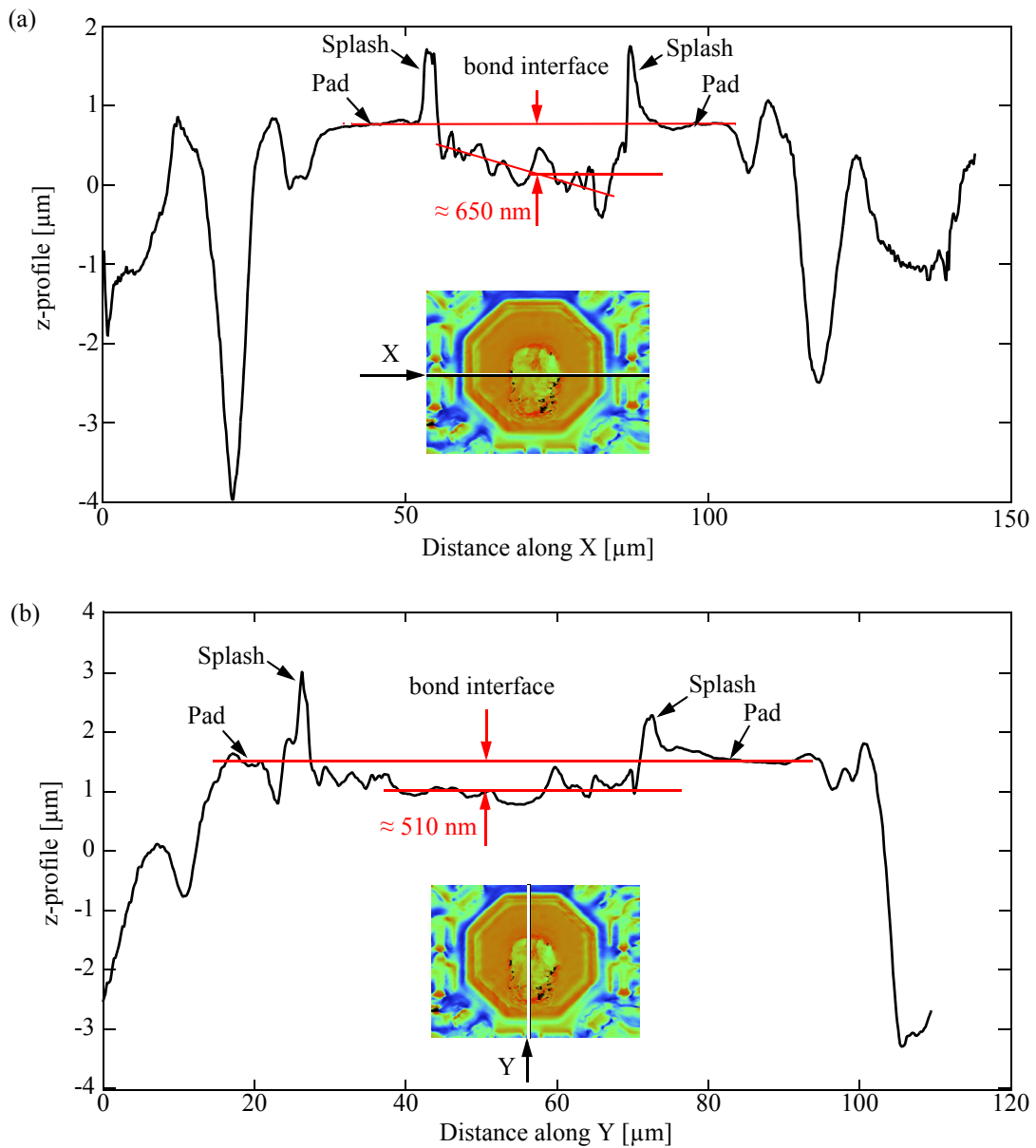
Fig. 5-13. Surface profile of the sheared Cu ball bond fractograph [Fig. 5-12 (a)] along the lines (a) X and (b) Y in Fig. 5-12 (b).

$$\Delta\delta_T = \sqrt{\Delta k^2 + \Delta H^2 + \Delta\delta_M^2} \tag{5-14}$$

where Δk and ΔH are the error in δ due to the estimated variation in k and H (Table 5-4), and the value of $\Delta\delta_M$ is the error in δ due to variation in A_{rel}, F_T, and S (measurement variability). The value of $\Delta\delta_M$ is calculated as the error of average using

$$\Delta\delta_M = \frac{s}{\sqrt{n-1}} = \frac{s}{\sqrt{5}} \tag{5-15}$$

where $\Delta\delta_M$, s, and n are the error, standard deviation of the derived δ reported in previous section, and sample size, respectively. The results show that the amount of wear depends significantly on the errors of these variables. Improved methods to derive k and experimental measurements of H will help improve the accuracy of determining the amount of wear during wire bonding.

The sliding wear theory used in this study is an overly simplified model to describe wear during fretting. An advanced fretting wear theory [135] will possibly result in improved accuracy in determining the amount of wear in wire bonding.

5.6   Summary

The US friction power during thermosonic ball bonding with Au and Cu wires, both 25 μm in diameter, is derived with an improved method from experimental measurements during the bonding process. The improvement results from a new, more accurate method to derive the mechanical compliance of the US system. The method employs bond process modifi-

Table 5-4. Sensitivity analysis of average total depth of wear, δ

Source	Name	Error estimate		Au ball bonding		Cu ball bonding	
				$\Delta\delta$		$\Delta\delta$	
		Type	Value	[nm]	[%]	[nm]	[%]
A_{rel}, F_T, S	$\Delta\delta_M$	Error of average	Eqn. 5-15	31.26	7.5	114.4	5.8
k	Δk	Error (assumed)	± 20%	166.5	20.0	358.3	20.0
H	ΔH	Variation [116]	± 15 MPa	121.4	29.2	261.2	29.2
Combined Error, $\Delta\delta_T$ (Eqn. 5-14)				208.4	50.0	457.9	51.1

cation in which the US current is set to levels that are too low to cause sliding. The bonding takes place during the third step, when the current is ramped up to the optimum value required for making good quality bonds. The US compliance values are derived from the first two steps and are 8.2 ± 0.2 μm/N and 7.7 ± 0.2 μm/N for the Au and Cu process, respectively. These values are determined within an average error estimate of $\pm 2\%$, substantially lower than the $\pm 7\%$ estimated with the previous method reported in Section 4.3.3. The US compliance in the case of Au is 6% higher due to the lower elastic modulus of Au compared to that of Cu.

Typical maximum values of relative amplitude of US friction at the interface are 655 nm and 766 nm for Au and Cu processes, respectively. These results show at least 19% of applied US amplitude is lost in the beginning of the bonding process due to friction at the ball/pad interface, and up to 96% is lost at the end of the bonding process. While the maximum value of interfacial amplitude is 17% higher in the Cu process compared to Au process, the total sliding distance in Cu process is 31% lower than the Au process.

The average maximum interfacial friction power is 10.3 ± 0.2 mW and 16.9 ± 0.3 mW during Au and Cu ball bonding, respectively. The total sliding friction energy delivered to the bond is 48.5 ± 8.0 mJ and 49.4 ± 4.0 mJ for the Au and Cu processes, respectively. These values result in average friction energy densities of 50.3 ± 7.8 J/mm^2 and 54.8 ± 4.8 J/mm^2 for the Au and Cu ball bonding, respectively.

A method to derive the volume of Al pad wear during wire bonding is reported. The method is based on the sliding wear model [115], and uses the derived relative sliding amplitude and measured US tangential force as inputs. The total average depth of Al wear during is estimated to be 416.3 ± 69.9 nm and 895.7 ± 114.4 nm for the Au and Cu processes, respectively. These values are significantly larger than the typical thickness of native oxide on IC bond pads [130-133].

6   Conclusions and Outlook

In this thesis, the mechanical and tribological mechanisms of thermosonic Au and Cu ball bonding and US Al wedge-wedge bonding processes have been investigated using piezo-resistive microsensors. Section 6.1 contains the conclusions of this research and Section 6.2 the recommendations for future research.

6.1   Conclusions

The conclusions are grouped according to the research objectives (Section 1.3.1).

6.1.1 Low-stress Cu Ball Bonding

The microsensor method applied to measure the *in situ* US force is fast and robust, yielding precise data during thermosonic ball and US wedge-wedge bonding processes. The measured US force is directly related to the mechanical stress acting on the pad and in combination with the bond force is a measure for the underpad damage risk. The underpad defect risks typical to Cu ball bonding can be reduced as has been demonstrated by modifying the wire material or the bonding process settings. Lower than optimized US levels can be used to obtain Cu ball bonds with shear strength c_{pk} values that are higher than that of a comparable Au wire bonding process while reducing the risk for underpad damage. Similarly, Cu wires developed with softer deformed balls are shown to produce less US force during bonding.

The conventional optimization of a Au ball bonding process aims at maximum bond shear strength for the targeted bond geometry. However, it also causes the highest US stress acting on the pad. In Cu ball bonding, this conventional optimization can increase the pad stresses and subsequently the risk of underpad damage to unacceptable levels. Hence, it is suggested to trade-off maximizing the bond shear strength and minimizing the US pad stress. The contour curves of the maximum US force and the bond shear strength shown in the US/BF process space are used to define a low-stress bonding region that can qualify for

the suggested trade-off. Thus, instead of a conventional shear strength maximization, an adequate trade-off between shear strength and pad stress is recommended for Cu ball bonding.

6.1.2 Improved Understanding of Process Tribology

The US tangential force signals allows for detailed insights into the mechanical and tribological mechanisms occurring during the bonding process. Some characteristic signal features of the Au ball bonding process are not evident in the Cu ball bonding process. The relative amount of the third harmonic in the Cu process signal is five times smaller than that in a comparable Au process, indicating less interfacial sliding.

In contrast to the thermosonic Au and Cu ball bonding processes, the US force in the Al wire wedge-wedge bonding process contains a strong asymmetric component. This is expressed by the large amount of second harmonic content. The other signal features are similar to those of a typical Au ball bonding process, in particular the typical time required to have successful bonding. Although slightly different from each other, it is concluded that stick-slip friction is an important mechanism in all these variants of wire bonding.

6.1.3 Theories of Interfacial Friction and Wear

A method to derive the transient interfacial US friction power during typical US Al wedge-wedge bonding process, and thermosonic Au and Cu ball bonding processes is demonstrated. The method uses a friction power theory based on Amontons' law of friction. For the first time, the maximum relative amplitude of the US friction at the interface in each of the three processes is reported.

The multi-step bond process modification during typical thermosonic Au and Cu ball bonding processes is shown to help improve the accuracy of the US compliance determination. Friction power differences of processes with different materials can now be quantified with greater significance. It is now possible to detect the changes in interfacial tribological processes, e.g. the start and end of interfacial sliding during the bonding process.

A method to estimate the amount of interfacial wear during thermosonic Au and Cu ball bonding processes is demonstrated. The method is based on Archard's sliding wear theory.

The results indicate that only a few cycles of US sliding are required to disperse the native oxide and contaminants away from the interface in both Au and Cu ball bonding. A relatively large error, estimated to be about 50% of the average, makes the method of deriving wear less accurate than the method of friction power.

It is found that the friction cleaning process in Cu ball bonding is faster than in Au, resulting in faster bond formation in the Cu process compared to the Au process. The total interfacial sliding amplitude in the Cu ball bonding process is significantly lower than that in the Au process. This is consistent to the findings on the reduced magnitude of the third harmonic of US force in the Cu process compared to the Au process. While the interfacial friction energy density values during typical Au and Cu ball bonding are similar in magnitude to each other, these values are significantly higher than those in a typical Al wedge-wedge bonding process.

6.2   Outlook

The following topics of future research are suggested:

1. The low-stress Cu bonding study reported here used standard shear testing of as-bonded samples to qualify the bonds. For these findings to be implemented in the industry, it is necessary to evaluate the long-term reliability performance of the low-stress ball bonds.

2. The microsensors used in this study quantify the average stress acting at the bond pad. However, it is the localized (peak) stresses that cause pad/chip failure. Future sensor designs can look at the possibility of measuring localized stresses at a number of pre-defined locations around the bonding zone.

3. An improved microsensor which can measure real underpad damage in conjunction with the stress measurement during the bonding process can be developed. Such a design would have to include both an underpad crack sensor [136] and the US force sensor. Combined with FE simulations, these sensors can help in a detailed understanding of the effective underpad stress distribution. Such an understanding promises to be helpful in gaining insights into pad failure mechanisms.

4. The friction power theory can be extended to predict bonding process parameters and bond strength [22], possibly leading to new bond process control methodologies [137] and higher process quality. The theory can be applied to estimate the rise in interfacial temperature due to frictional heating [138–141] during the bonding process.

5. The sliding wear theory used in this research is an overly simplified model to describe wear in US wire bonding. For example, it does not include the effects of interfacial temperature rise due to friction heating and surface or sub-surface fatigue (fretting fatigue). Future work can look at the possibility of using an advanced fretting wear theory [135] that includes these effects to study interfacial wear during US wire bonding. In addition, studies on how wear relates to bond quality might help to understand possible interactions between surface physics and joining mechanisms of ultrasonic wire bonding process.

Bibliography

[1]   Vardaman, E. J., "Advanced Packaging Interconnect Trends and Technology Development", *Proceedings of K&S Interconnect Technology Symposium*, 2007. Available online at: http://www.kns.com/_temp/downloads/agendaJuly2007/1.pdf.

[2]   Harman G., *Wire Bonding in Microelectronics: Materials, Processes, Reliability, and Yield,* 2nd ed., McGraw Hill, New York, 1997.

[3]   Greig, W. J., *Integrated Circuit Packaging, Assembly and Interconnections,* Springer Science+ Business Media, 2007.

[4]   Zhou, Y., Ed. *Microjoining and Nanojoining*, Woodhead Publishing Ltd., Cambridge, England, 2008.

[5]   Schwizer, J., Mayer, M., and Brand, O., *Force Sensors for Microelectronic Packaging Applications,* Springer, Berlin, Germany, 2005.

[6]   Small Precision Tools Inc., "Basics of Ball Bonding", In: *Technical Guide for Bonding Capillaries*. Available online at: http://www.smallprecisiontools.com/index.cfm ?parents_id=563.

[7]   Beleran, J., Turiano, Calpito, D. R. M., Stephan, D., Saraswati, Wulff, F., and Breach, C., "Tail Pull Strength of Cu Wire on Gold and Silver Plated Bonding Leads", *Proceedings of Semi Technology Symposium, SEMICON Singapore*, 2005.

[8]   Chen, J. L. and Lin, Y. C., "A New Approach in Free Air Ball Formation Process Parameters Analysis", *IEEE Transactions on Electronic Packaging Manufacturing*, Vol. 3, No. 2, 2002, pp. 116-122.

[9]   Tan, J., Toh, B. H., Ho, H. M., "Modelling of Free Air Ball for Copper Wire Bonding", *Proceedings of IEEE Electronic Packaging and Technology Conference*, 2004.

[10]   Murali, S., Srikanth, N., Vath, and C. J., "Grains, Deformation Substructures, and Slip Bands Observed in Thermosonic Copper Ball Bonding", *Materials Characterization*, Vol. 50, 2003, pp. 39-50.

[11]   Mayer, M., *Microelectronic Bonding Process Monitoring by Integrated Sensors*, Ph.D. Disseration ETH No. 13685, Physical Electronics Laboratory, ETH Zurich, Switzerland, 2000.

[12]   Osterwald, F., Lang, K. D., and Reichl, H., "Increasing Bond Quality by Ultrasonic Vibration Monitoring", *Proceedings of the International Symposium on Microelectronics*, SPIE, Vol. 2920, 1996, pp. 426-431.

[13] Joshi, K. C., "The Formation of Ultrasonic Wire Bonds between Metals", *Welding Journal,* Vol. 50, 1971, pp. 840-858.

[14] Jeng, Y. R. and Chen, J. Y., "On the Microcontact Mechanism of Thermosonic Wire Bonding in Microelectronics: Saturation of Interfacial Phenomena", *Tribology Transactions*, Vol. 48, No. 1, 2005, pp. 127-132.

[15] Langenecker, B., "Effects of Ultrasound on Deformation Characteristics of Metals", *IEEE Transactions on Sonics and Ultrasonics*, Vol. SU-13, 1996, pp. 1-8.

[16] Zhou, N., Li, X., and Noolu, N. J., "A Footprint Study of Bond Initiation in Gold Wire Crescent Bonding", *IEEE Transactions on Components and Packaging Technologies*, Vol. 28, No. 4, 2005, pp. 810-816.

[17] Geissler, U., Schneider-Ramelow, M., Lang, K., and Reichl, H., "Investigation of Microstructural Processes during Ultrasonic Wedge/Wedge Bonding of AlSi1 Wires", *Journal of Electronic Materials*, Vol. 35, No. 1, 2006, pp. 173-179.

[18] Lum, I., Huang, H., Chang, B. H. Mayer, M., Du. D., and Zhou, Y., "Effects of Superimposed Ultrasound on Deformation of Gold", *Journal of Applied Physics*, Vol. 105, 024905, 2009, pp. 1-5.

[19] Lum, I., Hang, C. J., Mayer, M., and Zhou, Y., "In-Situ Studies of the Effect of Ultrasound During Deformation on Residual Hardness of a Metal", *Journal of Electronic Materials*, Vol. 38, No. 5, 2009, pp. 647-654.

[20] Huang, H., Pequegnat, A., Chang, B. H., Mayer, M., Du, D., and Zhou, Y., " Influence of Superimposed Ultrasound on Deformability of Cu", *Journal of Applied Physics*, Vol. 106, 2009, 113514.

[21] Mayer, M., Schwizer, J., Paul, O., Bolliger, D., and Baltes, H., "In situ Ultrasonic Stress Measurements during Ball Bonding using Integrated Piezoresistive Microsensors", *Advances in Electronic Packaging*, Vol. 1, 1999, pp. 973-978.

[22] Gaul, H., Schneider-Ramelow, M., Lang, K.-D., and Reichl, H., "Predicting the Shear Strength of a Wire Bond Using Laser Vibration Measurements", *Proceedings of the 1st Electronics System Integration Technology Conference*, Vol. 2, 2006, pp. 719-725.

[23] McKenna, R. G. and Mahle, R. L., "High Impact Bonding to Improve Reliability of VLSI Die in Plastic Packages", *Proceedings of the IEEE Electronic Components Conference*, 1989, pp. 424-427.

[24] Toyozawa, K., Fujita, K., Minamide, T., and Maeda, T., "Development of Copper Wire Bonding Application Technology", *Proceedings of the IEEE Electronic Components and Technology Conference*, 1990, pp. 762-767.

[25] Toyozawa, K., Fujita, K., Minamide, S., and Maeda, T., "Development of Copper Wire Bonding Application Technology", *IEEE Transactions on Components, Hybrids, and Manufacturing Technology,* Vol. 13, No. 4, 1990, pp. 667-672.

[26] *Wire Bond Shear Test Method*, Electronics Industries Alliance/JEDEC Standard EIA/JESD22-B116, 1998, pp. 7-8.

[27] Blish, R. C., Parobek, L., "Wire Bonding Integrity Test Chip", *Proceedings of Reliability Physics Symposium*, 1983, pp. 142-147.

[28] Maiocco, L., Smyers, D., Munroe, P. R., and Baker, I., "Correlation between Electrical Resistance and Microstructure in Gold Wirebonds on Aluminium Films", *IEEE Transactions on Components, Hybrid, Manufacturing Technology*, Vol. 13, No. 3, 1990, pp. 592-595.

[29] Murcko, R. M., Susko, R. A., and Lauffer, J. M., "Resistance Drift in Aluminium to Gold Ultrasonic Wire Bonds", *IEEE Transactions on Components, Hybrid, Manufacturing Technology*, Vol. 14, No. 4, 1991, pp. 843-847.

[30] Ueno, H., "Influence of Al Film Thickness on Bondability of Au wire to Al pad", *Materials Transactions*, Japan Institute of Metals, Vol. 33, No. 11, 1992, pp. 1046-1050.

[31] Nicewarner, E., "Interconnect Resistance Characteristics of Several Flip-chip Bumping and Assembly Techniques", *Microelectronics Reliability*, Vol. 39, No. 1, 1999, pp. 113-121.

[32] Krabbenborg, B., "High Current Bond Design Rules-based on Bond Pad Degradation and Fusing of Wire, *Microelectronics Reliability*, Vol. 39, 1999, No. 77-88.

[33] Teverovsky, A. and Sharma, A., "High-temperature Degradation of Wire Bonds in Plastic Encapsulated Microcircuits", *Proceedings of IMAPS European Microelectronics Packaging Conference*, 2005.

[34] Hund, T. D., "Thermosonic Gold ball bond Accelerated Life Test", *Proceedings of IEEE Electronics Components and Technology Conference*, 1990, pp. 436-441.

[35] Mayer, M., "Non-destructive Monitoring of Au Ball Bond Stress during High-temperature Aging", *Proceedings of IEEE Electronics Components and Technology Conference*, 2008, pp. 1762-1768.

[36] Mayer, M., Moon, J. T., and Persic, J., "Measuring Stress Next to Au Ball Bond During High Temperature Aging", Vol. 49, 2009, pp. 771-781.

[37] Tan, C. M., Er, E., Hua, Y., and Chai, V., "Failure analysis of Bond Pad Metal Peeling using FIB and AFM", *IEEE Transactions on Components Packaging Manufacturing Technology Part A*, Vol. 21, No. 4, 1998, pp. 585–591.

[38] Tan, C. M., Linggajaya, K., Er, E., Chai, V., "Effect of BOE Etching Time on Wire Bonding Quality", *IEEE Transactions on Components Packaging Technology,* Vol. 22, No. 4, 1999, pp. 551-557.

[39] Jeon I. and Chung, Q., "The Study on Failure Mechanisms of Bond Pad Metal Peeling: Part A–Experimental Investigation", *Microelectron Reliability*, Vol. 43, 2003, pp. 2047-2052.

[40] Jeon I., "The Study on Failure Mechanisms of Bond Pad Metal Peeling: Part B – Numerical Analysis", *Microelectron Reliability*, Vol. 43, 2003, pp. 2055-2064.

[41] Tan, C. W. and Daud, A. R., "Bond Pad Cratering Study by Reliability Tests", *Journal of Materials Science: Materials in Electronics*, Vol. 13, No. 5, 2002, pp. 309-314.

[42] Tan, C. W. and Daud, A. R., "Cratering on Thermosonic Copper Wire Ball Bonding", *ASME Journal of Materials Engineering and Performance*, Vol. 11, No. 13, 2002, pp. 283-286.

[43] Saraswati, Thient, E. P. P., Stephan, D., Goh, H. M., Pasamanero, E., Calpito, D. R. M., Wulff, F. W., and Breach, C. D., "High Temperature Storage (HTS) Performance of Copper Ball Bonding Wires", *Proceedings of the 7th Electronics Packaging and Technology Conference*, 2005.

[44] Ho, H. M., Tan, Y. C., Tan, W. C., and Goh, H. M., "Investigation of Factors Affecting Bonded Ball Hardness on Copper Wire Bonding", *Proceedings of IMAPS Conference on Microelectronic Packaging,* Taiwan, 2006.

[45] Caers, J., Bischoff, A., Falk, J., Roggen, J., "Conditions for Reliable Ball/Wedge Copper Wire Bonding", *Proceedings of IEEE/CHMT European International Electronic Manufacturing Technology Symposium*, 1993, pp. 312 -315.

[46] Harman, G., "Reliability and Yield Problems of Wire Bonding in Microelectronics: The Application of Materials and Interface Science", *Proceedings of International Society for Hybrid Microelectronics*, McGraw-Hill, New York, 1989.

[47] Koyama, H., Shiozaki, H., Okumura, I., Mizugahsira, S., Higuchi, H., and Ajiki, T., "A New Bond Failure: Wire Cratering in Surface Mount Device," *Proceedings of the IEEE International Reliability Physics Symposium*, 1988.

[48] Khoury, S. L., Burkhard, D. J., Galloway, D. P., and Scharr, T. A., "A Comparison of Copper and Gold Wire Bonding on Integrated Circuit Devices," *IEEE Transactions on Components, Hybrids, Manufacturing Technology*, Vol. 13, No. 4, 1990, pp. 673-81.

[49] Huang, Y., Shah, A., Mayer, M., Zhou, Y., and Persic, J., "Effect of Ultrasonic Capillary Dynamics on the Mechanics of Thermosonic Ball Bonding", *IEEE Transactions on Ultrasonics, Ferroelectrics, and Frequency Control*, Vol. 57, No. 1, 2010, pp. 241-252.

[50] Mori, S. and Yoshida, H., "The Development of New Copper Ball Bonding Wire," *Proceedings of IEEE Electronics Components Conference*, 1988.

[51] Nguyen, N. T., McDonald, D., Danker, D., and Ng, P., "Optimization of Copper Wire Bonding on Al-Cu Metallization," *IEEE Transactions on Components Hybrids Manufacturing Technology*, Vol. 18, No. 2, 1995, pp. 423-429.

[52] Clatterbaugh, G. V. and Charles, H. K., "The Effect of High Temperature Intermetallic Growth on Ball Shear-Induced Cratering," *IEEE Transactions on Components Hybrids Manufacturing Technology*, Vol. 13, No. 1, 1990, pp. 167-75.

[53] Winchell, V. H. and Berg, H. M., "Enhanced Ultrasonic Bonding Development", *IEEE Transactions on Components, Hybrids and Manufacturing Technology*, Vol. CHMT-1, 1978, pp. 211-219.

[54] Harman, G. and Leedy, K. O., "An Experimental Model of the Microelectronic Ultrasonic Bonding Mechanism", *Proceedings of the 10th Annual Reliability Physics Symposium*, 1972, pp. 49-56.

[55] Chylak, B., Ling, J., Clauberg, H., and Thieme, T., "Next Generation Nickel-Based Bond Pads Enable Copper Wire Bonding", *ECS Transactions*, Vol. 18, No. 1, 2009, pp. 777-785.

[56] Tan, J., Zhong, Z. W., Ho, H. M., "Wire Bonding Process Development for Low-k Materials", *Microelectronic Engineering*, Vol. 81, 2005, pp. 75-82.

[57] Brunner, J. and Chylak, B., "Optimization of the Wire Bonding Process on Low-k Pad Structures", *Proceedings of the IMAPS Device Packaging Conference*, 2006.

[58] Deley, M. and Levine, L., "The Emergence of High Volume Copper Ball Bonding", *Proceedings of SEMICON West Conference*, 2004.

[59] Wulff, F. W., Breach, C. D., Stephan, D., Saraswati, and Dittmer, K. J., "Characterisation of Intermetallic Growth in Copper and Gold Ball Bonds on Aluminum Metallisation", *Proccedings of the 6th IEEE Electronics Packaging and Technology Conference*, 2004.

[60] Wulff, F. W., Breach, C. D., Stephan, D., Saraswati, Dittmer, K. J., and Garnier, M., "Further Characterisation of Intermetallic Growth in Copper and Gold Ball Bonds on Aluminum Metallisation", *Proceedings of the SEMI Technology Symposium*, Singapore, 2005.

[61] Hang, C. J., Wang, C. Q., Mayer, M., Tian, Y. H., Zhou, Y., and Wang, H. H., "Growth Behaviour of Cu/Al Intermetallic Compounds and Cracks in Copper Ball Bonds during Isothermal Aging", *Microelectronics Reliability*, Vol. 48, 2008, pp. 416-424.

[62] Shah, A., Mayer, M., Zhou, Y., Hong, S. J., Moon, J. T., "In situ Ultrasonic Force Signals during Low-temperature Thermosonic Copper Wire Bonding", *Microelectronic Engineering*, Vol. 85, No. 9, 2008, pp. 1851-1857.

[63] Qin, I., Shah, A., Huynh, C., Meyer, M., Mayer, M., and Zhou, Y., "Effect of Process Parameters on Pad Damage during Au and Cu Ball Bonding Processes", *Proceedings of IEEE Electronics Packaging and Technology Conference*, 2009.

[64] Kreye, H., "Melting Phenomena in Solid-state Welding Processes", *Welding Journal,* Vol. 56, No. 5, 1977, pp. 154-158.

[65] Krzanowski, J. E., "A Transmission Electron Microscopy Study of Ultrasonic Wire Bonding", *IEEE Transactions on Components, Hybrids and Manufacturing Technology*, Vol. 13, No. 1, 1990, pp. 176-181.

[66] Lee, J., Mayer, M., and Zhou, Y., "The Feasibility of Au Ball Bonding on Sn-Plated Cu", *Journal of Electronic Materials*, Vol. 36, No. 6, 2007, pp. 682-689.

[67] Hochman, R. F. and Gray, R. M., "A Note on the Effect of Ultrasonic Activation on Diffusion and Sintering", *International Journal of Powder Metallurgy*, Vol. 2, No. 3, 1966.

[68] Harthoorn, J. L., "Joint Formation in Ultrasonic Welding Compared with Fretting Phenomena for Aluminum", *Proceedings of the International Conference on Ultrasonics*, 1973, pp. 43-51.

[69] Chen, G., "The Role of Micro-slip in Ultrasonic Bonding of Microelectronic Dimensions", *Proceedings of the International Hybrid Microelectronics Symposium,* 1972.

[70] Mindlin, R. D., Mason, W. P., Osmer, J. F., and Deresiewicz, H., "Effects of an Oscillating Tangential Force on the Contact Surfaces of Elastic Spheres", *Proceedings of 1st National Congress on Applied Mechanics*, 1952, pp. 203-208.

[71] Ding, Y., Kim, J., Tong, P., "Numerical Analysis of Ultrasonic Wire Bonding: Effects of Bonding Parameters on Contact Pressure and Frictional Energy", *Mechanics of Materials,* Vol. 38, 2006, pp. 11-24.

[72] Lum, I., Jung, J. P., and Zhou, Y., " Bonding Mechanism in Ultrasonic Gold Ball Bonds on Copper Substrate", *Metallurgical and Materials Transactions A*, Vol. 36A, 2005, pp. 1279-1286.

[73] Lum, I., Mayer, M., and Zhou, Y., "Footprint Study of Ultrasonic Wedge Bonding with Aluminum Wire on Copper Substrate", *Journal of Electronic Materials*, Vol. 35, No. 3, 2006, pp. 433-442.

[74] Zhang, L., Gumaste, V., Poddar, A., Nguyen, L., and Schulze, G., "Analytical and Experimental Characterization of Bonding Over Active Circuitry", *ASME Journal of Electronic Packaging*, Vol. 129, 2007, pp. 391-399.

[75] Yeh, C.-L., Lai, Y.-S., "Transient Analysis of the Impact Stage of Wirebonding on Cu/low-K Wafers", *Microelectronics Reliability*, Vol. 45, 2005, pp. 371-378.

[76] Viswanath, A. G. K., Zhang, X., Ganesh, V. P., and Chun, L., "Numerical Study of Gold Wire Bonding Process on Cu/Low-k Structures", *IEEE Transactions on Advanced Packaging*, Vol. 30 (2007), pp. 448-456.

[77] Liu, Y., Irving, S., and Luk, T., "Thermosonic Wire Bonding Process Simulation and Bond Pad Over Active Stress Analysis", *IEEE Transactions on Electronic Packaging Manufacturing*, Vol. 31, No. 1, 2008, pp. 61-71.

[78] Takahashi, Y., and Inoue M., "Numerical Study of Wire Bonding - Analysis of Interfacial Defor-mation Between Wire and Pad", *ASME Journal of Electronic Packaging*, Vol. 124 (2002), pp. 27-36.

[79] Yeh, C. -L, Lai, Y. -S., "Comprehensive Dynamic Analysis of Wirebonding on Cu/ Low-K Wafers", *IEEE Transactions on Advanced Packaging*, Vol. 29, No. 2, 2006, pp. 264-270.

[80] Gao, Y., Doumanidis, C., "Mechanical Analysis of Ultrasonic Bonding for Rapid Prototyping", *ASME Journal of Manufacturing Science Engineering*, Vol. 124, 2002, pp. 426-434.

[81] Siddiq, A., Ghassemieh, E., "Thermomechanical Analyses of Ultrasonic Welding Process using Thermal and Acoustic Softening Effects", *Mechanics of Materials*, Vol. 40, 2008, pp. 982-1000.

[82] Zhong, Z. W., Goh, K. S., "Investigation of Ultrasonic Vibrations of Wire Bonding Capillaries", *Microelectronics Journal*, Vol. 37, 2006, pp.107-113.

[83] Gaul, H., Shah, A., Mayer, M., Zhou, Y., Schneider-Ramelow, M., and Reichl, H., "The Ultrasonic Wedge/wedge Bonding Process Investigated using In situ Real-time Amplitudes from Laser Vibrometer and Integrated Force Sensor", *Microelectronic Engineering*, In press. doi:10.1016/j.mee.2009.08.031.

[84] Or, S.W., Chan, H.L.W., Lo, V.C., and Yuen, C.W., "Ultrasonic Wire-bond Quality Monitoring using Piezoelectric Sensor", *Sensors and Actuators A*, Vol. 65, 1998, pp. 69-75.

[85] Pufall, R., "Automatic Process Control of Wire Bonding", *Proceedings of the IEEE Electronic Components and Technology Conference*, 1993, pp. 159-162.

[86] Mayer, M., Paul, O., and Baltes, H., "In situ Measurement of Stress and Temperature under Bonding Pads during Wire Bonding using Integrated Microsensors', *Proceedings of the 2nd International Conference on Emerging Microelectronics and Interconnection Technology*, 1998, pp. 129-133.

[87] Kanda, Y., "Piezoresistance Effect of Silicon", *Sensors and Actuators A*, Vol. 28, 1991, pp. 83-91.

[88] Bittle, D. A., Suhling, J. C., Beaty, R. E., Jaeger, R. C., and Johnson, R. W., "Piezo-resistive Stress Sensors for Structural Analysis of Electronic Packages, *Journal of Electronic Packaging*, Vol. 113, 1991, pp. 203-215.

[89] Sweet, J. N., "Die Stress Measurement using Piezoresistive Stress Sensors", *Thermal Stress and Strain in Microelectronics Packaging,* Von Nostrand Reinhold, New York, 1993, pp. 221-271.

[90] Mayer, M., Paul, O., Baltes, H., "Complete Set of Piezoresistive coefficients of CMOS n+ Diffusion", *Journal of Micromechanics and Microengineering,* Vol. 8, 1998, pp. 158-160.

[91] Mayer, M., Paul, O., Bolliger, D., Baltes, H., "Integrated Temperature Microsensors for Characterization and Optimization of Thermosonic Ball Bonding Process", *IEEE Transactions on Components and Packaging Technologies,* Vol. 23, No. 2, 2000, pp. 393-398.

[92] Mayer, M and Zwart, A., "Ultrasonic Friction Power in Microelectronic Wire Bonding", *Materials Science Forum*, Vol. 539-543, Part 4, 2007, pp. 3920-3925.

[93] Suman, S., Gaitan, M., Joshi, Y., and Harman, G., "Wire Bond Temperature Sensor", *Proceedings of the International Symposium of Microelectronics,* Vol. 4587, 2001, pp. 344-349.

[94] Suman, S., Gaitan, M., Joshi, Y., and Harman, G., "Wire Bonding Process Monitoring using Thermopile Temperature Sensor", *IEEE Transactions on Advanced Packaging*, Vol. 28, No. 4, 2005, pp. 685-693.

[95] Schwizer, J., Mayer, M., Bolliger, D., Paul, O., and Baltes, H., "Thermosonic Ball Bonding: Friction Model based on Integrated Microsensor Measurements", *Proceedings of the IEEE International Electronics Manufacturing Technology Symposium*, 1999, pp. 108-114.

[96] Mayer, M. and Schwizer, J., "Ultrasonic Bonding: Understanding How Process Parameters Determine the Strength of Au-Al Bonds", *Proceedings of IMAPS International Symposium on Microelectronics*, 2002.

[97] Mayer, M. and Schwizer, J., "Thermosonic Ball Bonding Model based on Ultrasonic Friction Power", *Proceedings of the IEEE Electronic Packaging Technology Conference*, 2003, pp. 738-743.

[98] Assembly and Packaging, In: *International Technology Roadmap for Semiconductors*, 2006, pp. 1-19.

[99] Sheaffer, M., Levine, L. R., Schlain, B., "Optimizing the Wire Bonding Process for Copper Ball Bonding using Classic Experimental Designs", *IEEE Transactions on Components, Hybrids and Manufacturing Technology*, Vol. 10, No. 3, 1986, pp. 32 1-326.

[100] Chen, J., Degryse, D., Ratchev, P., DeWolf, I., "Mechanical Issues of Cu-to-Cu Wire Bonding", *IEEE Transactions on Components and Packaging Technologies*, Vol. 27, No. 3, 2004, pp. 539-545.

[101] Degryse, D., Vandevelde, B., Beyne, E., "FEM Study of Deformation and Stresses in Copper Wire Bonds on Cu LowK Structures During Processing", *Proceedings of the 54th Electronic Components and Technology Conference*, Vol. 1, 2004, pp. 906-912.

[102] Kaimori, S., Nonaka, T., Mizoguchi, A., "The Development of Cu Bonding Wire with Oxidation-Resistant Metal Coating", *IEEE Transactions on Advanced Packaging*, Vol. 29, No. 2, 2006, pp. 227-231.

[103] Srikanth, N., Murali, S., Wong, Y. M., and Vath, C. J., "Critical Study of Thermosonic Copper Ball Bonding", *Thin Solid Films*, Vol. 462-463, 2004, pp. 339-345.

[104] Onuki, Koizumi, M., Araki, I., "Investigation on the Reliability of Copper Ball Bonds to Aluminum Electrodes", *Proceedings of the 37th Electronic Components and Technology Conference*, 1987, pp. 566-572.

[105] Callister, W. D., *Materials Science and Engineering: An Introduction*, John Wiley and Sons (5th Ed.), New York, 1999, pp. 169-171.

[106] Bhattacharyya, A., Rittel, D., Ravichandran, G., "Effect of Strain Rate on Deformation texture in OHFC Copper", *Scripta Materialia*, Vol. 52, 2005, pp. 657-661.

[107] Shah, A., Mayer, M., Zhou, Y., Hong, S. J., and Moon, C. T., "Reduction of Underpad Stress in Thermosonic Copper Ball Bonding", *Proceedings of IEEE 58th Electronic Components and Technology Conference*, Lake Buena Vista, Florida, U.S.A., 2008. pp. 2123-2130.

[108] Shah, A., Mayer, M., Zhou, Y., Hong, S. J., and Moon, J. T., "Low-stress Thermosonic Copper Ball Bonding", *IEEE Transactions on Electronics Packaging Manufacturing*. Vol. 32, No. 3, 2009, pp. 1-9.

[109] Hang, C. J., Lum, I., Lee, J., Mayer, M., Zhou, Y., Wang, C. Q., Hong, S. J., and Lee, S. M., "On-line Hardness Characterization of Novel 2-mil Copper Bonding Wires", *Proceedings of ASME InterPACK'07 Conference*, 2007.

[110] Lee, J., Mayer, M., Zhou, Y., and Hong, S. J., "Iterative Optimization of Tail Breaking Force of 1 mil Wire Thermosonic Ball Bonding Processes and the Influence of Plasma Cleaning", *Microelectronics Journal*, Vol. 38, 2007, pp. 842-847.

[111] *Metals Handbook, Vol. 2 - Properties and Selection: Nonferrous Alloys and Special-Purpose Materials*, ASM International, 10th Ed., 1990.

[112] Montgomery, D., *Introduction to Statistical Quality Control*, John Wiley and Sons, New York, 2004.

[113] Shah, A., Mayer, M., Zhou, Y., Persic, J., and Moon, C. T., "Optimization of Ultrasound and Bond Force to Reduce Pad Stress during Thermosonic Copper Ball Bonding", *Proceedings of IEEE 11th Electronics Packaging and Technology Conference*, Singapore, 2009, pp. 10-15.

[114] Shah, A., Mayer, M., Zhou, Y., Persic, J., and Moon, C. T., "Reduction of Ultrasonic Pad Stress and Aluminum Splash in Copper Ball Bonding", *Microelectronic Reliability: Special Issue on Cu Wire Bonding* (Accepted for publication, Feb. 2010).

[115] Archard, J. F., "Contact and Rubbing of Flat Surfaces", *Journal of Applied Physics*, Vol. 24, 1953, pp. 981-988.

[116] Randall, N. X., Hollander, E., and Julia-Schmutz, C., "Characterization of Integrated Circuit Aluminium Bonding Pads by Nanoindentation and Scanning Force Microscopy", *Surface Coatings and Technology*, Vol. 99, 1998, pp. 111-117.

[117] Krzanowski, J. E., Razon, E., and Hmiel, A. F., "The Effect of Thin Film Structure and Properties on Gold Ball Bonding", *Journal of Electronic Materials*, Vol. 27, No. 11, 1998, pp. 1211-1215.

[118] Bykov, Y. A., Karpukhin, S. D., Panfilov, Y. V., Boichenko, M. K., Cheptsov, V. O., and Osipov, A. V., "Measurement of Hardness of Thin Films", *Metal Science and Heat Treatment*, Vol. 45, No. 9-10, 1003, pp. 396-399.

[119] Shah, A., Gaul, H., Schneider-Ramelow, M., Reichl, H., Mayer, M., and Zhou, Y., "Ultrasonic Friction Power during Al Wire Wedge-Wedge Bonding", *Journal of Applied Physics*, Vol. 106, 2009, pp. 013503 -1/8.

[120] Gaul, H., Schneider-Ramelow, M., and Reichl, H., "Analysis of the Friction Processes in Ultrasonic Wedge/Wedge Bonding", *Microsystem Technologies*, Vol. 15, 2009, pp. 771-775.

[121] Cheng, X. and Li, A., "Investigation of Heat Generation in Ultrasonic Metal Welding using Microsensor Arrays", *Journal of Micromechanics and Microengineering,* Vol. 17, 2007, pp. 273-282.

[122] Shah, A., Mayer, M., Qin, I., Huynh, C., Zhou, Y., and Meyer, M., "Ultrasonic Friction Power during Thermosonic Au and Cu Ball Bonding", Submitted to: *Journal of Physics D: Applied Physics*. Under Review. MS. Ref. No. D/343589/PAP/244937.

[123] DeAngelis, D., "Laser Vibrometer Gain Data for Capillary Tip Displacement Versus Current (120kHz)", *Internal Communication with Kulicke and Soffa Inc.*, Fort Washington, PA, May 28, 2009.

[124] Stowers, I. F. and Rabinowicz, E., "The Mechanism of Fretting Wear", *Transactions of the ASME: Journal of Lubrication Technology*, Vol. 95, 1973, pp. 65-70.

[125] Hurricks, P. L., "The Mechanism of Fretting and the Influence of Temperature", *Industrial Lubrication and Tribology*, 1976.

[126] Rabinowicz E., *Friction and Wear of Materials*, 2nd Ed., John Wiley and Sons Inc., New York, 1995.

[127] Lipson, C., *Wear Considerations in Design*, Prentice-Hall Inc., Englewood Cliffs, 1967.

[128] Rabinowicz, E., "The Dependence of the Adhesive Wear Coefficient on the Surface Energy of Adhesion", *Wear of Materials*, American Society of Mechanical Engineers, 1977, pp. 36-40.

[129] Rabinowicz, E., "Wear Coefficients – Metals", In: *Wear Control Handbook*, Eds: M. B. Peterson, W. O. Winer, American Society of Mechanical Engineers, 1980, pp. 475-506.

[130] Petzold, M., Berthold, L., Katzer, D., Knoll, H., Memhard, D., Meier, P., and Lang, K.-D., "Surface Oxide films on Aluminum Bond Pads: Influence on Thermosonic Wire bonding Behavior and Hardness", *Microelectronics Reliability*, Vol. 40, 2000, pp. 1515-1520.

[131] Ohmae, N., and Rabinowicz, E., "The Wear of Nobel Metals", *ASLE Transactions*, Vol. 23, 1980, pp. 86-92.

[132] Editorial, "The Wear of Nobel Metals in Air: Effect of Crystal Structure and Compatibility" *Platinum Metals Review*, Vol. 24, No. 4, 1980, pp. 134.

[133] Eagle Analytical Group LLC, "Evaluating Bond Pad Performance", *Application Note AN 332*, 2007. Available online at: http://www.eaglabs.com/files/appnotes/AN332.pdf.

[134] Doebelin, E. O., *Measurement Systems Application and Design*, 4th Ed., Mc Graw Hill, New York, 1990, pp. 58-67.

[135] Attia, H., "A Generalized Fretting Wear Theory", *Tribology International*, Vol. 42, No. 9, 2009, pp. 1380-1388.

[136] Blish, R. C., Patel, P. D., Lewis, D. E., and Hatchard, C. D., "Method and Apparatus to Achieve Bond Pad Crater Sensing and Stepping Identification in Integrated Circuit Products", *United States Patent*, No. US 6,548,881 B1, 2003.

[137] Geissler, U., Reichl, H., Gaul, H., Lang, K.-D., and Schneider-Ramelow, "Method and Device for Controlling the Generation of Ultrasonic Wire Bonds", *European Patent Application*, WO2008028906 (A1), 13-03-2008.

[138] Archard, J. F., "The Temperature of Rubbing Surfaces", *Wear*, Vol. 2, 1958, pp. 438-455.

[139] Ashby, M. F., Abulawi, J., and Kong, H. S., "Temperature Maps for Frictional Heating in Dry Sliding", *Tribology Transactions*, Vol. 34, No. 4, 1991, pp. 577-587.

[140] Tian X. , Kennedy F. E., "Maximum and Average Flash Temperatures in Sliding Contacts", *ASME Journal of Tribology*, Vol. 116, 1994, pp. 167–174.

[141] Greenwood J.A., Alliston-Greiner A.F., "Surface Temperatures in a Fretting Contact", *Wear*, Vol. 155, 1992, pp. 269–75.